Spring 2005

High Power 121.6 NM Radiation Source for Advanced Lithography

Jianxun Yan
Old Dominion University

Recommended Citation

Yan, Jianxun. "High Power 121.6 NM Radiation Source for Advanced Lithography" (2005). Doctor of Philosophy (PhD), Dissertation, Electrical & Computer Engineering, Old Dominion University, DOI: 10.25777/z99w-ny77
https://digitalcommons.odu.edu/ece_etds/145

HIGH POWER 121.6 NM RADIATION SOURCE FOR ADVANCED LITHOGRAPHY

by

Jianxun Yan
B.S. July 1991, Hunan University, P.R. China
M.S. July 1997, Chinese Academy of Science, P.R. China

A Dissertation Submitted to the Faculty of
Old Dominion University in Partial Fulfillment of the
Requirements for the Degree of

DOCTOR OF PHILOSOPHY

ELECTRICAL ENGINEERING

OLD DOMINION UNIVERSITY
May 2005

Approved by:

Mool C. Gupta (Director)

Linda Vahala (Member)

Mounir Laroussi (Member)

Gene J.-W. Hou (Member)

ABSTRACT

HIGH POWER 121.6 NM RADIATION SOURCE FOR ADVANCED LITHOGRAPHY

Jianxun Yan
Old Dominion University, 2005
Director: Dr. Mool C. Gupta

A novel high power 121.6 nm radiation source based on dielectric barrier discharge (DBD) has been developed for advanced lithography applications. The discharge unit consists basically of a hollow tube made of a dielectric material with two loop-electrodes wrapped on the outside of the tube. The discharge is generated inside the tube by means of a 13.56 MHz RF power system. The discharge unit is located in a vacuum chamber that provides a dynamic gas flow and windows for radiation transmission.

A very intense and spectrally clean Lyman-α line at 121.6 nm was observed by operating the DBD discharge in a mixture of high-pressure Ne (200 – 800 Torr) with a small admixture of hydrogen (less than 0.1%). The hydrogen Lyman-α line at 121.6 nm was emitted via near-resonant energy transfer between Ne excimer and H_2, which leads to the dissociation of H_2 and the excitation of atomic hydrogen. The Lyman-α emission intensity depends on the operating parameters of the discharge, such as gas pressure, gas mixture, gas flow rate and discharge geometry. By optimizing these parameters, the radiation power at 121.6 nm was maximized. A radiation source with 8 watts of optical power at 121.6 nm wavelength with a narrow line width ($\Delta\lambda < 0.03$ nm) and stable operation was achieved. Since the lamp operation is based on RF driven plasma, one

method to increase the power was to couple more RF power in discharge. By applying a proper RF network and optimizing the electrode area and gap, the RF reflection losses were reduced to less than 2%. With the water-cooling circuit, the temperature of discharge unit was maintained at room temperature and the lamp operation was able to maintain over 100 hours of continuous use.

The discharge was optimized by simulation using XOOPIC software, which models the plasma as discrete macroparticles interacting with EM field. Some plasma parameters, such as the spatial distribution of electrons and ions, electron energy and density, were calculated from simulation. The results from simulation were in agreement with our experimental measurements. By modeling the operating parameters of the discharge, such as pressure, discharge tube diameter, electrode area and gap, high radiation power at 121.6 nm was achieved.

The lamp source was sent to MIT-Lincoln Lab for 121.6 nm lithography applications. From the initial results of the experiments, patterns with 63 nm feature size lines were obtained. One other application of lamp was explored where direct metal pattern writing by VUV photodissociation of a palladium acetate ($Pd(OCOCH_3)_2$, Pdac) was achieved. Palladium metal pattern was directly written on glass substrate by using a MgF_2 mask, which has feature linewidth of 1 μm.

A stable, high power, and narrow spectral width radiation source has been developed. It is suitable for photolithography and nanofabrication applications.

ACKNOWLEDGMENTS

I would like to express my sincerest appreciation and gratitude to my advisor, Dr. Mool C. Gupta, for his guidance and continuous support on my study and research. He contributed his experience, knowledge, and time to help me to bring this work to a conclusion. I would like to thank Dr. Linda Vahala, Dr. Mounir Laroussi, and Dr. Gene J.-W. Hou for their willingness to serve on my dissertation committee. Their invaluable comments and suggestions are greatly appreciated.

I am grateful for the valuable advices from Dr. Mounir Laroussi, Dr. Karl Schoenbach, and Dr. Kurt Becker from Stevens Institute of Technology. I also would like to thank Dr. Jousef Mohajer, Dr. Nariman Akhmerov, and Shujun Yang for their help and cooperation during the course of this work.

I also appreciate the help received from colleagues and friends at the Applied Research Center of Old Dominion University. I would especially like to thank Mr. Brandt Robertson and Mr. Richard Podlesny for technical support.

Finally, I would like to express my gratitude to my mother, Meifeng Shi, and my whole family for their love and support.

TABLE OF CONTENTS

LIST OF TABLES

LIST OF FIGURES

CHARPTER I

INTRODUCTION

1.1 Background

Lithography at 157 nm with fluorine lasers is widely considered as the last generation of conventional photolithography methods for sub-100 nm device fabrication [1,2,3]. It is believed that 100 nm lithography and beyond will be performed with next-generation lithography (NGL) technologies such as extreme ultraviolet (~ 13 nm) [4,5], electron beams [6], x-ray [7], and ion beams [8]. But these alternatives represent a more radical deviation from the present optical-based technology, and thus they encounter more engineering challenges. It has become apparent that a more mainstream extension of optical lithography should be considered as well. One of the alternatives is 121.6 nm technology [9]. Therefore the development of high intensity 121.6 nm light source appears to be necessary for extension of optical lithography [10,11].

121.6 nm, Lyman-α line ($2p^2P_0 \rightarrow 1s^2S$), is emitted from an atomic transition in hydrogen, and is sufficiently of narrow spectral width for lithography. There are many plasma-based methods, which can achieve 121.6 nm line emission. Examples are arc discharge [12], microwave excited discharge [13], glow discharge [14], microhollow cathode discharge [15], and laser-induced plasma [16]. Here we explore a discharge lamp based on a novel variant of the Dielectric Barrier Discharge (DBD) [17]. The DBD configuration is characterized by the presence of at least one dielectric layer in the current path between the electrodes and discharge space [18,19]. The dielectric barrier serves two functions. It distributes the microdischarges evenly over the entire electrode area and it limits the amount of charge and energy that can be fed into an individual filament. The plasma conditions of these microdischarges are ideal for excimer formation, in which major fraction of the energy gained by the electrons in the electric field can be deposited in excited atomic and molecular states. One important feature of the DBD is that the plasma parameters can be influenced and thus optimized by external means. The reduced electric field E/n (E - electrical field and n - gas density), which mainly controls the mean electron energy, can be influenced by the pressure in the discharge, the electrode spacing and voltage slope at breakdown. On the other hand, the electron density in a microdischarge can be controlled again by pressure and the properties of the dielectric barrier. The simplicity, versatility and low cost of the DBD make it attractive for generating a Lyman-α line.

In this research a high power DBD-based 121.6 nm radiation source has been developed [10,11]. By optimizing the lamp parameters such as gas pressure, discharge tube diameter, electrode area and gap, the 121.6 nm radiation power can be maximized. The 121.6 nm source has been evaluated for photolithography and the results indicated that it is a reliable source for lithography below 100 nm feature size.

1.2 Optical Lithography

Optical lithography has been used over the past 30 years by the semiconductor industry to generate small features, which determine the size of the electronic circuits on semiconductor wafers [20]. The reduction in patterned feature size from 5 μm to the current 0.13 μm and submicron in the near future have been the result of a remarkable combination of improvements in all aspects of optical lithography. The optical imaging systems employed in lithography have been designed and manufactured to have near diffraction-limited performance, and therefore the resolution limits afforded by them can be estimated from diffraction theory. There are basically three imaging methods: contact printing, proximity printing, and projection printing.

In the contact and proximity printing, light is directed through the mask and onto the resist-coated substrate, which is held in direct contact or close proximity to the mask. The theoretical resolution for a pattern of equal lines and spaces in contact/proximity lithography is given by:

$$2b_{\min} = 3[\lambda(s + 0.5d)]^{1/2} \tag{1.3.1}$$

where, $2b_{min}$ = grating period,

s = width of gap between mask and resist surface,

d = resist thickness, and

λ = exposure wavelength.

Assuming perfect contact in contact printing, $s = 0$, we have:

$$2b_{\min} = 3[(\lambda d / 2)]^{1/2} \tag{1.3.2}$$

In proximity printing, the substrate is brought very close to the mask (about 10 μm), but does not touch it. The resist thickness is negligible compared to the substrate-mask separation, so the equation becomes:

$$2b_{\min} \sim 3[\lambda s]^{1/2} \tag{1.3.3}$$

From these equations, the obvious way to enhance resolution is to reduce the exposure wavelength.

In contrast to contact and proximity printing, projection printing involves the introduction of extremely complicated lens elements into the optical system. But it provides considerable benefits in optical lithography and it is the dominant form of lithography in industry today. The most important performance parameters of the projection printer are resolution and depth of focus (DOF). The resolution or minimum feature size is given by:

$$d_{\min} = k\lambda / NA \qquad (1.3.4)$$

where k is a process variable with a typical value between 0.7 and 1.0, λ is the exposure wavelength, and NA is the numerical aperture, which is given by:

$$NA = n \sin\theta \qquad (1.3.5)$$

where n is the index of refraction in the image medium, and θ is the half-angle of the cone of light converging to a point image at the substrate.

The depth of focus (DOF) is given by:

$$DOF = k\lambda / 2(NA)^2 \qquad (1.3.6)$$

The DOF must be larger than any variations in the flatness of the photoresist surface. From the resolution and DOF equations, one can sum up all the problems with the promise of projection lithography: the way to increase resolution is to decrease the wavelength, and to increase the numerical aperture of the lens. However, both of these options have the effect of decreasing the depth of focus. In the choice between reducing the wavelength and increasing the numerical aperture, reducing wavelength causes less of a decrease in DOF and therefore it should be preferable.

It is obvious that to reduce the feature size is to decrease the exposure wavelength. Indeed, optical lithography has gradually evolved from using the visible emission of mercury discharge lamp (g-line, 436 nm), to the near-UV emission of mercury lamp (I-line, 365 nm), to the deep-UV emission of KrF excimer lasers (248 nm), and recently to the even deeper-UV emission of the ArF excimer lasers (193 nm) [21,22]. The vacuum-UV (VUV) wavelength of F_2 excimer laser (157 nm) is rapidly emerging as the industry-preferred technology for the post-193 nm era [2,23]. At that point, the target application is the 100 to 70 nm feature size generations. In the trend of this progress, it is natural to explore further methods to reduce the lithography wavelength under 150 nm in VUV range. The promising way to obtain such short wavelength emission is incoherent excimer light from discharge sources. The 121.6 nm emission of atomic hydrogen, also called Lyman-α line, is the most promising candidate.

1.3 VUV Excimer Emission

Comparing with excimer lasers [24], which are generally discharge pumped and have efficiencies on the order of 1%, excimer lamps, which provide noncoherent radiation, have a much higher efficiency, up to 40% [19]. The photon emission from excimer lamps is based on the mechanisms of excimer formation. All rare gas atoms have a $^1S_0$ electronic ground state. The lowest lying electronically excited state manifold results from the excitation of one of the valance n_p-electrons (n = 2, 3, 4, 5 for Ne, Ar, Kr, Xe) to the next higher (n+1) s-level. This results in four “P-states”, which are most appropriately described in an intermediate angular momentum coupling scheme. Two of the four “P-states” are metastable. Excimer (excited dimmer) molecules are formed via three-body collisions involving a metastable rare gas atom and two ground state atoms. An excimer molecule has at least one stable bound excited state and a repulsive ground state. The conditions for efficient excimer formation require: 1) a sufficiently large number of electrons with energies above the threshold for the formation of metastable rare gas atoms; 2) high pressure in order to have a sufficiently high rate of three-body collisions; and 3) exceptional purity of the gas to prevent quenching of the long-lived metastable atoms. Excimer emissions occur from the bound excimer state to the repulsive ground state. Rare gas excimer emission spectra are dominated by the so-called second excimer continua which are the result of transitions from the lowest lying $^1\Sigma u$ and $^3\Sigma u$ excimer states of the pure gases to the repulsive ground state. The peak in the second continua of different rare gases are at wavelengths of 172 nm (Xe), 146 nm (Kr), 126 nm (Ar), and 84 nm (Ne) [18].

There are several versions of excimer lamps that can generate the excimer emission. The microhollow cathode discharge, is one of excimer lamps with simple in design, low cost, high efficiency and compact [25,26,27]. It is characterized by hollow structure scaled to be several hundreds of micrometer. However, the most common one is dielectric barrier discharge, which generates excimer radiation in pulsed filamentary or micro discharges between two electrodes, one or both of them covered with a dielectric layer. The pulse duration of microdischarges is in the nanosecond range. This discharge has a simple design, can be compact or large, and has high efficiency with high optical power. Because the discharge and the electrodes are insulated by the dielectric layers, so lamps based on the barrier discharge can have long lifetime and very good power stability. These lamps can meet the requirements for photolithography applications. In our experiment, we designed a DBD based lamp to obtain a high intensity 121.6 nm Lyman-α line.

1.4 Lyman-α Line Radiation

We note that because of the nature of the excimer emissions as continua, excimer emissions are inherently not as narrow as atomic line emissions, but have a typical width of several nanometers, e.g. the Ar_2* excimer emission at 126 nm is in fact a more than 25 nm wide band extending from 113 to 139 nm. The design of catadioptric optical system is required for this source to be suitable for photolithography.

Due to the high excitation energy of rare-gas ions or excited rare-gas atoms, the Lyman-α line can be obtained under various excitation conditions when trace amount of hydrogen is added to rare-gas. For example, intense Lyman-α was observed in He-H_2 mixture near atmospheric pressure [28]. Argon/hydrogen mixture in low-pressure glow-discharge has been investigated to generate VUV for the photochemical treatment of polymer surfaces [14]. Energy transfer form neon ion to hydrogen molecules has been studied by an e-beam induced light source to obtain strong intense Lyman-α line [29]. Neon-hydrogen mixture in a high-pressure discharge was shown to be a very efficient and selective method for generating Lyman-α [30]. The process of neon excimer formation, the resonant energy transfer from neon excimer molecules to molecular hydrogen and subsequent light emission are shown as follows:

$$\mathrm{Ne} + e^- \rightarrow \mathrm{Ne}^+ + 2e^-, \tag{1.5.1}$$

$$\mathrm{Ne}^+ + 2\,\mathrm{Ne} \rightarrow \mathrm{Ne}_2^+ + \mathrm{Ne}, \tag{1.5.2}$$

$$\mathrm{Ne}_2^+ + e^- \rightarrow \mathrm{Ne}^* + \mathrm{Ne}, \tag{1.5.3}$$

where Ne^* denotes a metastable neon atom. Alternatively, Ne* can be the product of direct electron impact,

$$\mathrm{Ne} + e^- \rightarrow \mathrm{Ne}^* + e^- \tag{1.5.4}$$

Neon excited molecular complexes without stable ground states, also called excimer, are formed by three-body reaction of a metastable neon atom and two atoms in the ground state,

$$\mathrm{Ne}^* + \mathrm{Ne} + \mathrm{Ne} \rightarrow \mathrm{Ne}_2^* + \mathrm{Ne}. \tag{1.5.5}$$

Resonant energy transfer from Ne_2^* (excited state gap = 14.8 ± 0.8 ev) to molecular hydrogen leads to H_2 dissociation (4.48 ev) and excitation of hydrogen atom H* (10.2 ev),

$$Ne_2^* + H_2 \rightarrow 2Ne + H + H^* \ \ (n = 2). \tag{1.5.6}$$

Excited hydrogen atoms spontaneously emit the Lyman-α line,

$$H^* \rightarrow H + h\upsilon \ (121.6 \text{ nm}). \tag{1.5.7}$$

The hydrogen Lyman-α emission at 121.6 nm has several attractive features for photolithography applications, 1) a favorable wavelength at 121.6 nm for the generation of small feature sizes below 0.1 μm, 2) the possibility of stable, cw operation, 3) a very narrow natural line width of about 0.0001 nm, so that there is no need to use a wavelength selective device such as a grating to produce a sufficiently narrow linewidth, which reduces the availability intensity considerably, and 4) the possibility of having a source "sealed off" from its environment with a LiF or MgF_2 window.

1.5 Overview of Dissertation

Chapter 1 presents the historical trend of optical lithography. The extension of optical lithography with a much shorter wavelength under 157 nm would be a candidate for next-generation lithography. 121.6 nm Lyman-α radiation from excimer discharge could be the potential reliable source for lithography.

Chapter 2 introduces several of VUV radiation sources including, excimer lasers, synchrotron radiation sources, and plasma radiation sources.

Chapter 3 describes the experimental setup of the lamp, a novel DBD-based VUV discharge source. It covers the structure of lamp chamber, the configuration of spectral and optical power measurements, and the gases inlet/outlet and pumping system.

Chapter 4 is the description of source characterizations. First we presented a discharge model and electrical circuit of RF-driven discharge. Then, experimental results were presented, including spectra, optical power, stability, beam profile, and associated discharge parameters. Finally, the simulation results were presented.

Chapter 5 presents two applications of the 121.6 nm lamp, 121 nm lithography and direct metal pattern writing by VUV photodissociation. The 121 nm lithography application was performed by MIT Lincoln Lab. Patterns with feature size under sub-micron were obtained by using the 121.6 nm source. The direct metal pattern writing was performed in our lab with the lithography facility. Palladium patterns with feature size of 1 μm were obtained by dissociating palladium acetate to palladium.

Chapter 6 summarizes this project and puts forward suggestions for future work.

CHAPTER II

VUV RADIATION SOURCES

Vacuum ultraviolet (VUV) spectra region extends from 100 nm to 200 nm, namely from the onset of atmospheric absorption at approximately 190 nm to the short wavelength cut-off of suitable window materials at around 105 nm [31]. This division of the electromagnetic spectrum is useful, since experiments involving VUV radiation require certain experimental conditions – for example chambers or beam pipes must be evacuated or purged of air, and may need window and differential pumping. The applications of VUV radiation is of increasing interest in basic technology, because this relative narrow range of wavelengths spans a broad and important range of photon energies: 6 –12 eV which corresponds to the energies of many atomic and molecular states. For this reason, VUV radiation has important applications in spectroscopy and photochemistry.

The excited states of many atomic and molecular species lie at energies of several eV and thus there are a lot of sources to generate the VUV radiation [32]. These sources cover lasers, synchrotron radiation, and plasmas. In this chapter, an overview of the VUV spectral region and a description of existing techniques for generating VUV radiation and its measurement will be presented.

2.1 Excimer Formation and Excimer Lasers

The development of excimer laser systems marked a significant turning point in the development of VUV coherent sources. The physical mechanisms underlying these laser systems is based on the mechanisms of excimer molecules [24].

The interaction of the ground states of two closed-shell systems (atoms or molecules) is usually repulsive except for a weak long-range van der Waals or electrostate interaction. But the interaction of an excited state with the ground state of the same fragments can form a strong chemical bond. This excited state bound has been called an excimer (excited dimmer) that is a slightly bound excited molecular state of complexes that do not possess a stable ground state [33]. The bonding of the excited state can be classified into three extreme regions. There are bound covalent, Rydberg, and charge transfer excimer states. Covalent bonding occurs when a pair of electrons share a bonding orbital that is distributed over the two atoms [34]. The group II homonuclear molecules such as Hg_2, Mg_2 provide examples of this type of bonding. The Rydberg orbitals are diffuse and have relatively little molecular bonding or anti-bonding characteristics [35,36]. The basic bonding behavior of the Rydberg molecular state is, therefore, determined by the bonding characteristics of the limiting positive ion curve. Rare gases excimer states provide the example of Rydberg excimers. Charge transfer excited states are well known in the case of the rare gas halides [37,38]. It is likely that such states are very widespread. They result when the ionization potential of the electron donor is relatively high such that the ion-pair asymptote is so high in energy relative to the neutral atom asymptote that the Coulombic attraction is insufficient to make the ion-pair state the ground state.

All rare gases can form a slightly bound excited dimer lying about 8 -20 eV above the repulsive ground state. The kinetics of excimer systems are rather complex, involving several ground state and molecular species, several ionic species, and a large number of atomic and molecular species [39,40,41,42,43]. The mechanism of excimer forming can be viewed as a sequence of collisional energy exchanges. Fig. 2.1 portrays a schematic diagram of this sequence. We use xenon as a specific case, but the conclusions also apply to other noble gases. The high energy electrons ionize or excite the xenon gas in reactions such as,

$$e^- + Xe \rightarrow Xe^+ + 2e^- \tag{2.1.1}$$

$$e^- + Xe \rightarrow Xe^* + e^- . \tag{2.1.2}$$

The secondary electrons created will have a mean energy of five to seven electron volts depending on the gas. At the high pressure (at atmosphere), three-body association to form the molecular ion is rapid through the process

$$Xe^+ + 2Xe \rightarrow Xe_2^+ + Xe . \tag{2.1.3}$$

Subsequently, a dissociative recombination reaction quickly forms an excited neutral in a dissociating state,

$$Xe_2^+ + e^- \rightarrow Xe_2 \rightarrow Xe^{**} + Xe . \tag{2.1.4}$$

Typical rate constants for this process are 10^{-6} cm^3s^{-1} and decrease with increasing electron temperature. In xenon, the repulsive curves that cross the lower vibrational levels of the molecular ion lead to xenon atoms in 6p states. Three-body association reactions, which are rapid at high pressures, then lead to formation of bound molecular levels, which has energy of roughly 8 eV (Fig. 2.2) [44].

$$Xe^{**} + 2\,Xe \rightarrow Xe_2^* + Xe \tag{2.1.5}$$

Under suitable discharge conditions excimers decay within nanoseconds and emits VUV radiation, peaking at 172 nm,

$$Xe_2^* \rightarrow 2Xe + h\nu \quad (\lambda = 172 \quad nm) . \tag{2.1.6}$$

At high pressure the formation process are fast compared with the radiant decay times, thereby enabling the kinetic chain to produce a high-density population inversion.

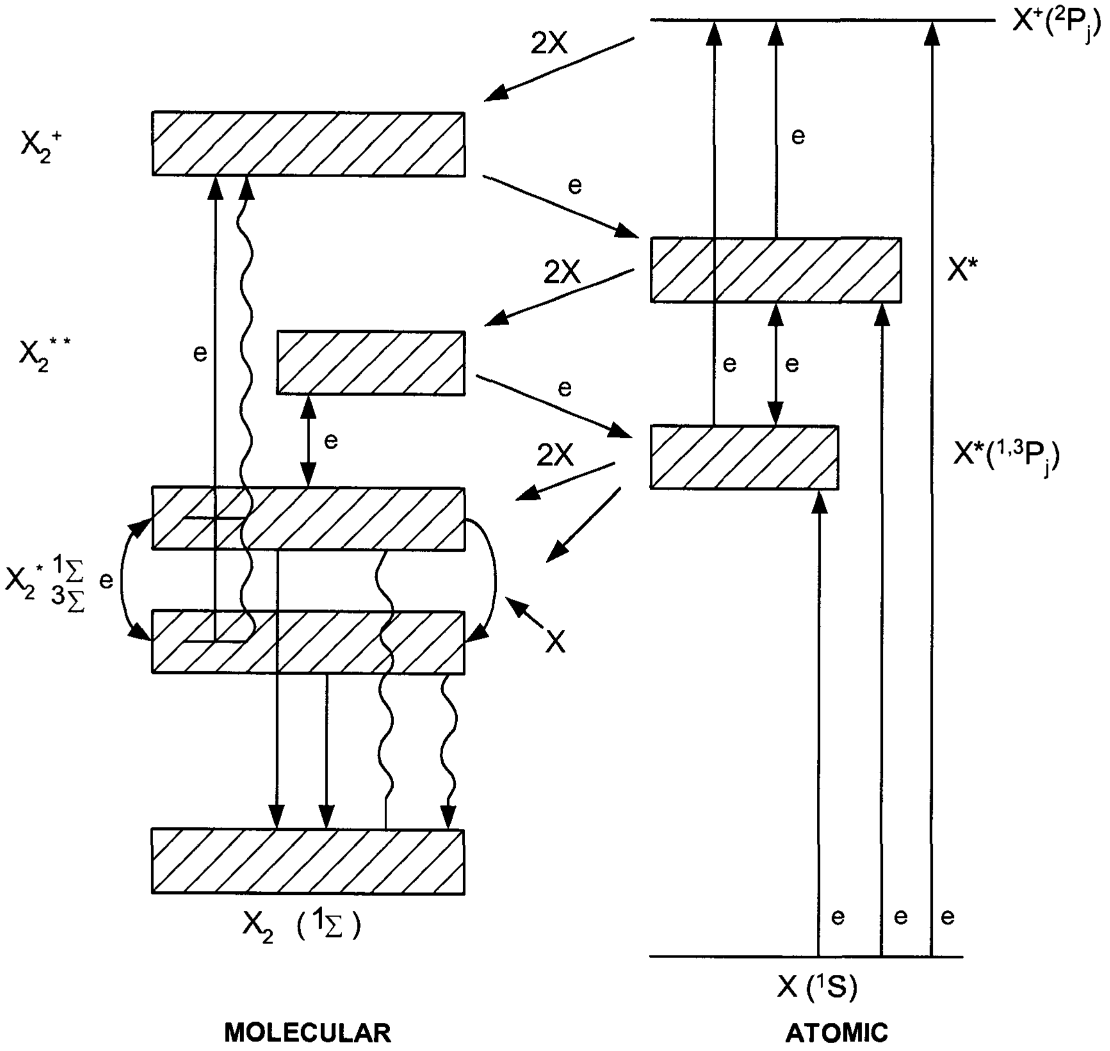

FIG. 2.1 Energy levels relevant to noble gas excimer production. X refers to any noble gas except helium (ref. 24).

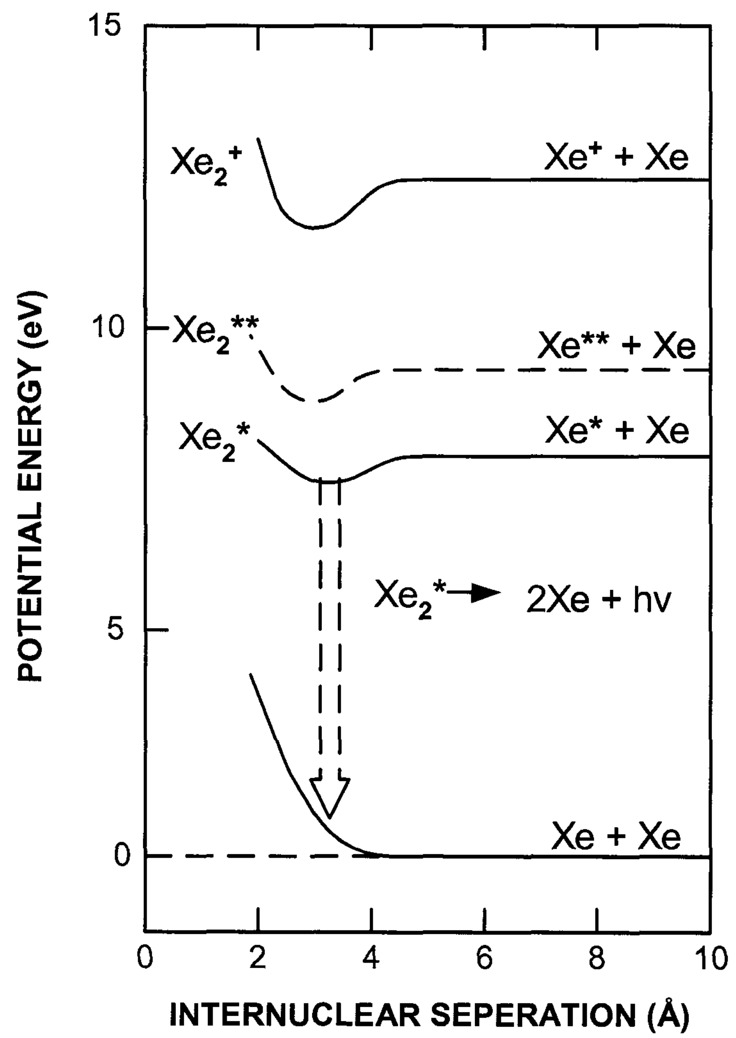

FIG. 2.2 Simplified potential energy diagram of xenon (ref. 44).

From the reactions, one can conclude that to form excimers, atoms and molecules must first be brought to an excited state or ionic state. The atoms and molecules are excited and ionized by high-energy electrons through collisional energy transfer. The excimers are generated by means of a three-body process where the excited atom reacts with two atoms that are generally in the ground state. As for any three-body process, the collision rate increases with pressure, making high-pressure operation mandatory for efficiency excimer generation. Excimer formation mainly depends on these two conditions, a) high-energy electrons which can excite the ground state atoms to an excited level; and b) relatively high pressure which makes three-body collision more favorable.

Excimer decay mechanisms

The fluorescence decay of excimers is mainly dependent on the condition of pressure. The rare gases have two low-lying, but separated excimer states, both of which may radiate; they are the ${}^1\Sigma_u^+$ state that dissociates to ${}^3P_1$ and ${}^1S_0$ atoms and the ${}^3\Sigma_u^+$ state that dissociates to ${}^3P_2$ and ${}^1S_0$. Taking xenon as an example we can clearly show the transition from the resonance line at 147 nm to first continuum at 150 nm and finally to second continuum at about 172 nm with rising pressure [19]. The resonance line dominating at low pressure (50 mbarr) results from a transition ${}^3P_1$-${}^1S_0$, the first continuum appearing at 100 mbarr corresponds to transitions from vibrationally excited excimer states (${}^1\Sigma_u^+, {}^3\Sigma_u^+$) to the shallow minimum of the ground state potential resulting in emission around 150 nm. At higher pressure, the second continuum at 172 nm increase since the vibrational relaxation rate is higher than that of the first continuum emission process (Fig. 2.3).

The change of the emission characteristics from resonance line to first and second continuum corresponds to a visible change of discharge modes. At low pressure, the discharge appears to be a homogeneously radiating glow discharge; at medium pressure, microdischarges emerges on a continuous background; and at high pressure, the discharge ends with many bright microdischarges dominating.

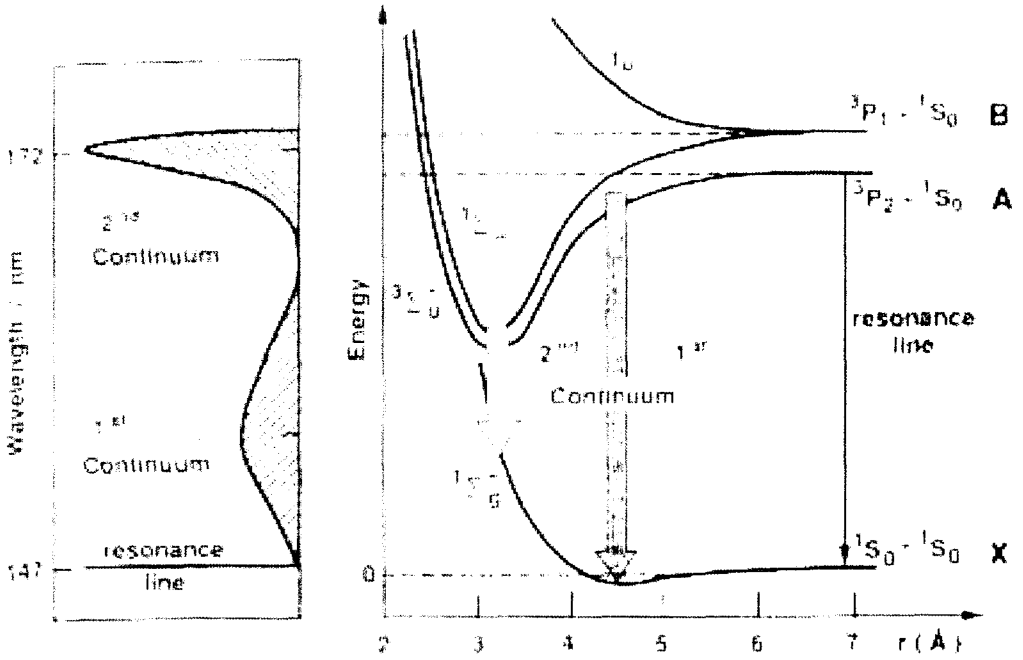

FIG. 2.3 Part of the potential energy diagram of xenon and corresponding excimer emission (ref. 19).

Although the radiative lifetimes of these two states ($^1\Sigma_u^+, {}^3\Sigma_u^+$) are appreciably different, both contribute to the fluorescence observations. Table 2.1 shows the lifetime data for different excimers from the review of Lorents [39].

Several experiments have been made to examine the decay rate of the excimer emission at relatively high excitation densities. At low pressure, the decay rate is low and rises with increasing pressure asymptotically to a limiting value. For xenon, this asymptotic value is $6 \pm 1 \times 10^7 s^{-1}$. This agrees with the value that would be derived assuming that complete population equilibrium exists between the triplet and singlet excimer states. The inverse of the decay time becomes

$$\frac{1}{\tau} = \frac{3}{4} \cdot \frac{1}{\tau_3} + \frac{1}{4} \cdot \frac{1}{\tau_1} \cong 5.2 \times 10^7 s^{-1} \tag{2.1.7}$$

where ¾ and ¼ are the fractional population of the triplet and singlet populations, and τ_3 and τ_1 are the triplet and singlet lifetimes. Electrons are an important factor in establishing this equilibrium. In the presence of an electron beam, the relatively hot plasma electrons will rapidly mix the excimer states as well as their precursors. In addition to the excimer radiative decay, excimer density can be reduced through several other processes, such as super-elastic collision, photoionization, and quenching by neutral atoms.

Table 2.1 Radiative lifetimes of excimer states

Excimer	$^1\Sigma_u^+$ [ns]	$^3\Sigma_u^+$ [μs]	Ref.
Ne_2^*	-	5.1	[45]
	2.8	11.9	[46]
	-	12 ± 6	[46]
		6.62	[47]
Ar_2^*	-	2.8	[48]
	-	3.7	[49]
	4.2 ± 0.13	3.2 ± 0.3	[50]
		4.0 ± 2.0	[46]
		3.22	[47]
Kr_2^*	-	1.7	[49]
	-	0.3	[51]
	-	0.36 ± 0.16	[46]
		0.35	[47]
Xe_2^*	5.5 ± 1.0	0.09 ± 0.05	[50]
	-	0.10 ± 0.05	[46]
	-	0.140 ± 0.45	[46]

Depending on the excimer medium, excimer lasers emit light at several characteristic wavelengths from between 100 nm to 400 nm. Argon excimer radiation has a peak at 126 nm and krypton eximer radiation has a peak at 146 nm. Besides rare gases excimer, there are also halogen dimmers (F_2*, Cl_2*, Br_2*, I_2*), and rare-gas halogen excimers (ArCl*, KrCl*, ArF*, KrF*, ArBr*, and so on). F_2* has strong emission at 157 nm and ArF* at 193 nm [52]. Table 2.2 lists some of the excimer species, the wavelength of the intense laser transitions, and the type of excitation scheme used for each wavelength.

Table 2.2 Selected excimer laser transitions

Laser Excimer species	Emission Wavelength (nm)	Excitation Scheme		
		Electric Discharge	Electron Beam	E-beam Controlled Discharge
Ar_2^*	126		X	
Kr_2^*	146		X	
F_2^*	157	X		
Xe_2^*	172		X	
$ArCl^*$	175	X		
ArF^*	193	X	X	
$KrCl^*$	222	X	X	
KrF^*	248	X	X	X
$XeBr^*$	282		X	
$XeCl^*$	308	X	X	X
XeF^*	351	X	X	X

The excimer transitions in the rare gases or rare-gas halogen have been used to provide powerful, tunable VUV laser radiation. These laser systems require very high pump power densities due to the short lifetime of the upper laser level (20-50 ns), and to date laser oscillation has been demonstrated only in electron beam pumped systems with typically 0.5 – 2 MeV electrons at 0.3 – 7 kA in a 0.5 – 5 ns excitation pulse. The rare gas excimer lasers operate at high pressures since the upper laser level is formed by three-body reactions. Thus, the high pump power density is necessary to achieve laser oscillation in the vacuum ultraviolet.

Several different approaches have been used to pump excimer laser gain media. These schemes include: 1) direct excitation by a high-energy electron beam; 2) excitation by an electric discharge controlled by an electron beam; 3) direct high-voltage electric discharge excitation; and 4) excitation by optical pumping with another laser beam.

2.2 Synchrotron Radiation Source and Free-Electron Laser (FEL)

Synchrotron radiation is a very bright, broadband, polarized, pulsed source of light extending from the infrared to the x-ray [53]. It is an extremely important source of VUV radiation. It is well known from classical theory of electricity and magnetism that accelerating charges emit electromagnetic radiation [54, 55]. In the case of synchrotron radiation, relativistic electrons are accelerated in a circular orbit (storage ring) and emit electromagnetic radiation. In electron storage rings there are three possible sources of synchrotron radiation: dipole (bending) magnets; wigglers, which act like a sequence of bending magnets with alternating polarities; and undulators, which are also multi period alternating magnet systems but in which the beam deflection are small, resulting in coherent interference of the emitted light.

Free-Electron Laser (FEL) is an intense, powerful laser light that can be tuned to a precise color or wavelength. Because the electrons are freed of atoms in an accelerator, free-electron lasers absorb and release energy at any wavelength. The key components of a free-electron laser oscillator include an electron accelerator, which accelerates electrons to high energy, and a wiggler, which "wiggles" the electrons [56]. The interaction between the electron beam and the output radiation field in an FEL is mediated by a periodic wiggler magnetic field. When the electron beam traverses the wiggler magnetic field, it is periodically accelerated transversely and initially emits incoherent radiation. If the electron beam is longitudinally bunched, the coherent radiation emits. The accelerating electrons radiate, and mirrors feedback the optical power at the chosen wavelength until it is amplified and gains the nonlinear saturations. A portion of the light can be transmitted through one mirror for external use by the optical cavity.

Free-electron lasers can be operated over virtually the entire electromagnetic spectrum from microwaves through the ultraviolet and up to an average power levels of kilowatts. FEL can be controlled more precisely than conventional lasers to produce intense powerful light in brief bursts with extreme precision. There are many laboratories, such as Jefferson Lab (USA)[57], DESY (Germany), Argonne (USA), JAERI (Japan), SLAC (USA), and so on, have built free-electron lasers. Some of them are VUV FELs with very high intensity radiation [58,59].

2.3 Plasma Radiation

Plasma radiation sources radiate both spectral line and continuum spectrum in VUV region. Most of the spectral line radiation emitted by gaseous plasmas stems from atomic processes. In this section, we start with atomic spectroscopy for plasma and then describe all kinds of laboratory discharge sources.

2.3.1 Atomic Spectroscopy

Atoms have specific allowed energy levels determined by the rules of quantum mechanics [60]. An isolated atom such as hydrogen has a potential energy that derives from the Coulomb law of attraction between the proton and the electron. There are an infinite number of discrete levels with energies

$$E_q = -\frac{m_r Z^2 e^4}{2\hbar^2 q^2} \qquad q = 1,2,3.....,\tag{2.1.8}$$

where m_r is the reduced mass of the atom, e is the electron charge, Z is the number of protons in the nucleus, and $\hbar$ is Planck's constant. The computation of the energy levels of more complex atom is difficult, because of the interactions among the electrons and the effects of electron spin. All atoms have discrete energy levels with energy differences that typically lie in the optical region. Some of the energy levels of He and Ne atoms are illustrated in FIG. 2.5.

Each atom in a collection continuously undergoes random transitions among its different energy levels. The undergoing downward or upward transitions between its energy levels make an atom emit or absorb a photon. The photon energy due to an energy transition between two energy levels is

$$\Delta E = E_2 - E_1 = h\nu \tag{2.1.9}$$

where $\hbar$ is the Planck's constant and ν is the frequency.

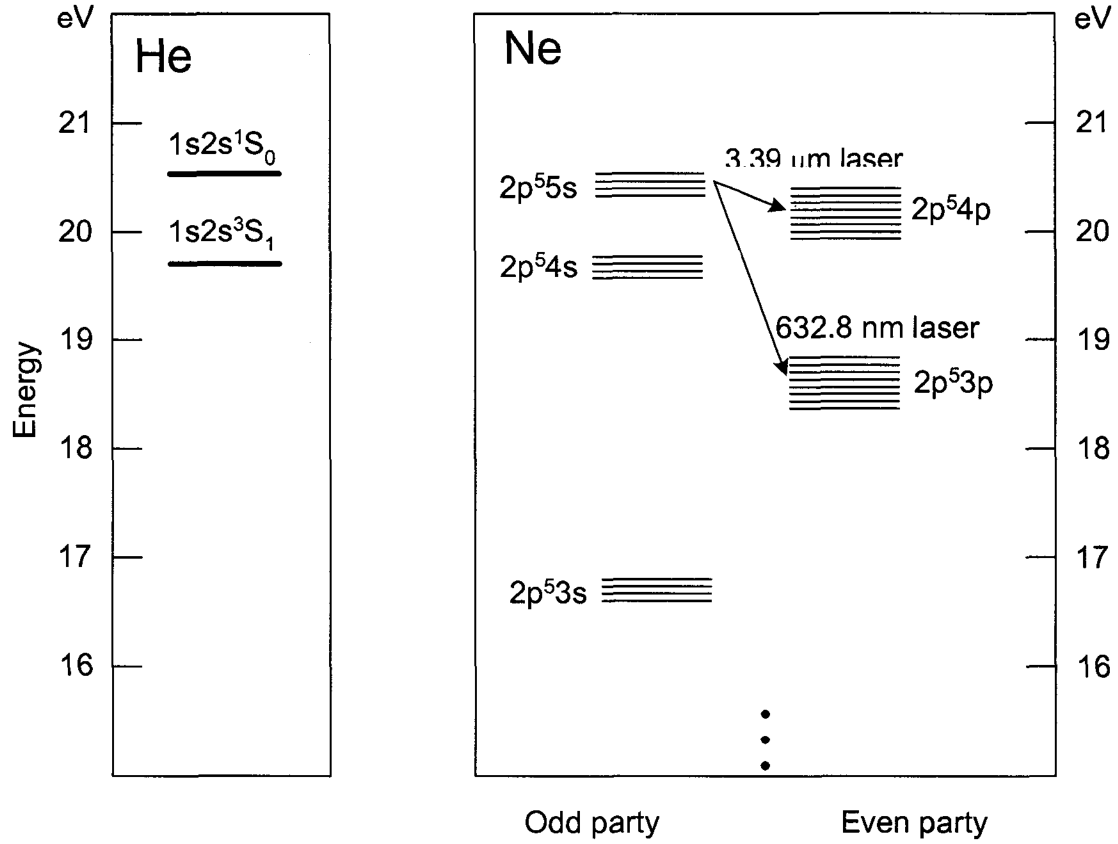

FIG. 2.5 Energy levels of He and Ne atoms (ref. 60).

There are three forms of interaction between photon and atoms – spontaneous emission, absorption, and stimulated emission. Spontaneous emission is an independent transition that the atom is initially in the upper energy level and release its energy in the form of a photon. Absorption is a transition induced by a photon that the atom transits from lower energy to upper energy level. Finally, if the atom is in the upper energy level and contains a photon, the atom may be stimulated to emit another photon in the same mode. Photon emission may also be induced by the presence of the external sources of energy, such as an external source of light, and an electron current or a chemical reaction. The excited atoms can emit light called luminescence light.

The emission intensity at a specific radiation line is dependent on transition probabilities and the number density of excited atoms in the upper level. Table 2.3 shows some spectra lines of hydrogen atom and oxygen at wavelength 100 nm to 130 nm.

Table 2.3 Radiative transitions and atomic lines (from Atomic Spectra Database of NIST) [61].

Spec	**Wavelength Vac. (Å)**	**Rel. Int.**	**A_{ki} (10^8 s^{-1})**	**Acc.**	**E_i -- E_k (cm^{-1})**	**Configurations**	**Terms**	**J_i-J_k**	**g_i-g_k**	**TP Refs**
H I	1025.722	300	1.672	A A'	0. 97492.32	1s – 3p	^2S - $2P^\circ$	1/2- 3/2	2-4	1
H I	1215.668	1000	6.265	A A'	0. 82259.28	1s-2p	^2S - $^2P^\circ$	1/2- 3/2	2-4	1
O I	1302.168	900	3.41	A	0. 76794.98	$2s^2 2p^4$ - $2s^2 2p^3$ ($^4S^\circ$)$3s$	^3P - $^3S^\circ$	2-1	5-3	2,5, LS
O I	1304.858	600	2.03	A	158.265 76794.98	$2s^2 2p^4$ - $2s^2 2p^3$ ($^4S^\circ$) $3s$	^3P - $^3S^\circ$	1-1	3-3	2,5, LS
O I	1306.029	300	0.676	A	226.977 76794.98	$2s^2 2p^4$ - $2s^2 2p^3$($^4S^\circ$) $3s$	^3P - $^3S^\circ$	0-1	1-3	2,5, LS

Where the column **Spec.** means the selected stage of ionization of that element; **Wavelength** is in vacuum region; **Rel. Int.** means relative intensity of that radiation; A_{ki} means the transition strengths; **Acc.** means the accuracy of transition strength (A is the highest level); and $E_i - E_k$ means the lower level and upper level energies. The next two columns show the **configurations** and **terms** of the lower and upper levels; J_i-J_k mean the total electronic angular momentum of the lower and upper level; and g_i-g_k mean lower level statistical weight($g_i = 2J_i+1$) and upper level statistical weight ($g_k = 2J_k+1$).

For example, Lyman-α line at 121.6 nm is a hydrogen atomic line that transits from $2p^2P_0$ to $1s^2S$, has the relative intensity of 1000, transition probability of $6.265x10^{-8}s^{-1}$, and transition energy of 82259.286 cm^{-1} or 10.2 eV.

2.3.2 Discharge Sources

Plasma sources in a laboratory can provide glow discharges, dielectric barrier discharges, wall stabilized arcs, inductively coupled plasma sources, electron cyclotron resonance ion sources, electron-beam excitation sources, capillary discharges, and hollow cathode discharges. All of these discharges may have different ways to excite bound atomic or molecular states and to ionize constituents of the discharge, but they all will radiate both spectral line radiation and continuum radiation. In some cases, the source conditions can be controlled so one or the other of these types of radiation may dominate. The choice of a source often depends on which type of radiation is desired. For example, if a source exhibits a stable well-characterized continuum spectrum in VUV region, then this source could be used as a secondary radiometric calibration standard throughout this spectral region [62]. If the discharge emits primarily narrow, well-know spectral lines, then it might be used as a wavelength calibration source for spectrometers. If the source exhibits line shape with a Gaussian profile, this may be due to the random thermal motion of the emitting atom, which is proportional to its thermal temperature [63].

Glow Discharge is a source that produces enhanced neutral and ion line emission in the VUV spectral by exploiting the principle of the charge particle oscillator [64,65]. The original use of the charged particle oscillator was the production of ion beams. The nature of the sources is that free electrons inside a cylindrical electrode (cathode) follow oscillatory trajectories, passing between two wires (anodes), which are coaxial to the cylinder. Because of this oscillating mode, the electron collisional mean free path can be much longer than the dimensions of the cylinder. The discharge is maintained at low pressures with DC or AC high voltage supply, and can radiation atomic lines depending on the type of gas. These discharges can emit VUV radiation by electron impact ionization and excitation of gases at low pressures.

Wall Stabilized Arc Sources are capable of generating stable plasmas in the temperature range from 6,000 to 25,000 K and high electron density with high gas pressure. Arc discharge has been used to investigate the properties of plasmas, including their stability [66,67]. Their high radiative outputs have made this discharge an important tool in the studies of thermal equilibrium, atomic physics, and quantitative spectroscopy. Because of its high reproducible and stable output, its continuum emission can be calibrated with respect to a primary radiometric standard and used as a transfer radiometric source standard. Wall stabilized arc have been used primarily on the VUV spectral region with a transmitting window as the high-pressure-vacuum interface. The spectral output of the discharge typically consists of a recombination continuum, possibly excimer continua with rare gases, as well as line spectra [68]. Deuterium arc lamp is the most widely used source that continuously emits VUV light in the Lyman band of molecular hydrogen and the hydrogen recombination continuum [69].

Electron Cyclotron Resonance Sources occur at the conditions of a magnetic field conjunction with a microwave frequency electric field to a gas, where these conditions enhance the plasma breakdown. The absorbed power supplied to such magnetized plasmas reaches a maximum near the plasma electron cyclotron resonance

(ECR) frequency [70]. The ECR frequency, V_{ec}, is given in terms of the applied magnetic induction by

$$v_{ec} = eB/2\pi\ m_e = 27.9922 \times B\ \text{(GHz)}. \tag{2.1.10}$$

At an rf frequency of 2.45 GHz, the value of B is 87.5 mT. Therefore, the power input to a rf generated plasma can be enhanced by applying a relatively small magnetic field. The concept of electron cyclotron resonance plasma generation have been applied to make ion sources of highly charged ions, to provide heating in fusion plasmas, and to produce low-temperature, high-density plasmas for semiconductor processing. This charge can also produce VUV radiation [71,72]. An example of microwave discharge used in photoelectron spectroscopy and enhanced by the application of an external magnetic field have demonstrated the effectiveness of this method to generate higher level of ionization and thus shorter wavelength in the VUV region [73].

Inductively Coupled Plasma (ICP) Sources are primarily used in the generation of spectra for species identification and concentration determination [74, 75]. The concept for producing spectra from an ICP is generally that the material to be studied is introduced into the flow of a carrier gas by gas injection, aerosol or evaporation. The plasma is established in an enclosed region surrounded by an inductive coil powered by a rf power supply. The VUV spectra have been investigated with an ICP. One example was to use this source as a quantitative analytical tool for nonmetallic species identification and as a source of emission of argon spectral lines emanating from metastable ${}^3P_2$ and ${}^3P_1$ states [76].

The Capillary Discharge is generated in a small dielectric tube, such as 2 mm i.d. and 60 mm long Al_2O_3 tube [77,78]. The discharge is operated at a pressure about

100 Pa, and could provide high flux VUV photons. The power supply utilized to sustain a discharge in the capillary is a variable voltage and current-stabilized supply up to 6 kV and 200 mA. The discharge is primarily operated in He or Ne and produced both the He I and He II or Ne I and Ne II line spectra.

Hollow Cathode Sources are a special type of glow discharges that have a dominant negative glow [79,80]. The cathode is shaped like a hollow cylinder with a diameter of approximately 10 mm. The buffer gas pressure is chosen so that the negative glow fills the volume of the hollow cathode to create a thin cathode fall covering the interior surface of the cathode with a thickness of typically 1 mm or less. Most of the electric potential of the discharge is dropped within cathode fall, so that the inner volume of the cathode is nearly field free. Electrons emitted from the surface of the cathode acquire nearly the full potential energy by passing through the cathode fall. A proper gas pressure is chosen so that the mean free path of the electrons is larger than the diameter of the hollow cathode. The electrons oscillate between the two opposing cathode falls until their kinetic energy is transferred to the gas atoms by collision. The electrons have sufficient energy to ionize the atoms of buffer gases that fill the interior of the hollow cathode. Because of the features of the hollow cathode source, it is particularly suitable as a windowless VUV radiation source that can be calibrated as a radiometric secondary source standard [81,82,93,84].

In Penning Discharge Sources the discharge is generated by the application of a strong magnetic field parallel to the electric field of the cathode fall [85]. The magnetic field forces the electrons in the discharge to gyrate around the magnetic field lines when they move along the electric field. In this way the effective pathlength of the electron in the discharge is greatly enhanced and thus the collision probability with a neutral atom is increased.

Electron-beam Excitation Sources are the discharges that a high-energy electron beam forms an electron gun pass through the buffer gases and excites and ionizes the gas to create the discharge [86,87]. A highly stable source of VUV line radiation can be obtained by the electron-beam excitation and without the problem of the erosion of the cathode. With sufficient accuracy of the target gas density from pressure and temperature measurements, energy and current of the exciting electrons, observed length of the electron beam, and solid angle of observation, the electron-beam excitation sources can be used as a radiometer source standard [88].

2.3. 3 Dielectric Barrier Discharge (DBD)

Dielectric Barrier Discharges (DBDs) are also referred as Silent Discharges that are a type of non-equilibrium gas discharges created between two electrodes, at least one of which is covered by an insulator [18]. The spacing between the electrodes is typically a few millimeters and the pressure of operation ranges from 0.1 to 10 bars. Fig. 2.6 shows the typical configurations of DBD. As a voltage is applied to the gap, a breakdown is attributed to the buildup of high local electric fields in the space charge along the surface of the insulator. This can produce an avalanche of electrons resulting in a thin, nearly cylindrical conductive filament (micordischarge) from the cathode to the anode, and these filamentary discharges occur over the entire surface of the insulator. Each discharge will transport tens to thousands of picocoulombs of charge with a current density of several hundred amperes per square centimeter. That results in a plasma with characteristics of electron density from approximately 10^{14} cm^{-3} to greater than 10^{15}cm^{-3} and with mean electron energies ranging from 1 eV to greater than 10 eV. The dielectric barrier serves two functions: 1) distributing the micro discharges evenly over the entire electrode area, and 2) limiting the amount of charge and energy that can be fed into an individual micro-discharge.

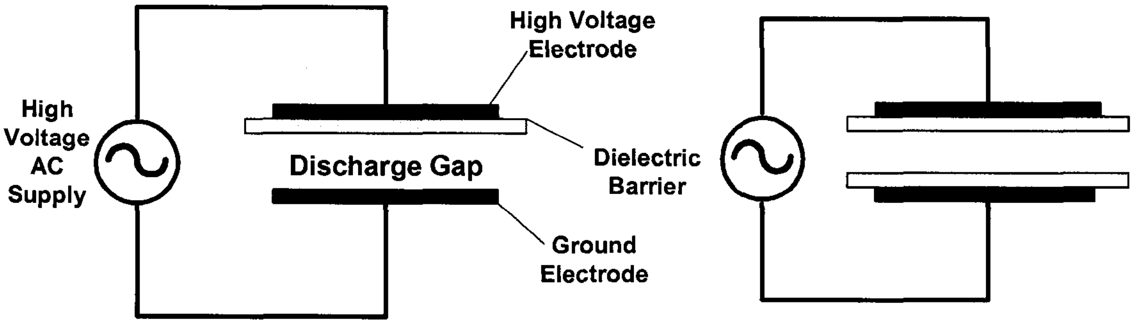

Fig. 2.6 Basic geometries of DBD.

Dielectric Barrier discharges are ideally suited for excimer generation. Based on this discharge one can build efficient high-intensity light sources operating in the VUV region. The spectrum from DBD discharge consists of resonance spectral line and excimer continua. In suitable discharge geometries and gas mixtures, the microdischarges can present an ideal environment for excimer formation. In principle, the double-walled Siemens tube sources, planar sources with flat dielectrics and cylinder tube sources have been used to meet different applications. Different pure rare gases and gas mixtures are used to produce different wavelength radiations [9,10,11,17,90].

Here we use the Xe_2^* excimer as an example for pure rare gases [91]. Under electron bombardment in xenon at sufficiently high pressure, a slightly bound excimer with an excitation energy of roughly 8 eV is formed. Under suitable discharges conditions (mainly dependent on pressure), it decays within nanoseconds and emits VUV radiation, peaking at 172 nm (second continuum) with a half-width of 12 nm.

From the model calculations, the intrinsic efficiencies in excess of 40% at low electron densities and reduced fields close to 50 Td (1 Td = 10^{-17} Vcm^2) have been obtained [18]. According to the experimental results, an intrinsic efficiency of 15 ~ 30% was obtained. Photon fluxes up to 10^{17} per second and per cm^2 of electrode surface can be achieved. The DBD discharge in xenon is a powerful incoherent VUV source, the photon energy of which is high enough to split most chemical bonds.

A large number of other excimers can be formed in DBD discharges. Other rare gas dimers (Ar_2^*, Kr_2^*), halogen dimers (F_2^*, Cl_2^*, Br_2^*, I_2^*), rare-gas halogen excimers ($ArCl^*, KrCl^*, XeCl^*, ArF^*, KrF^*, ArBr^*, KrI^*$), as well as mercury rare gas excimers, were excited. In many cases narrowband VUV radiation of remarkable efficiency was obtained.

There are a number of photochemical and photophysical processes that require intense VUV radiation in certain well-defined spectral regions. VUV curing of certain polymers, paints, and adhesives is already a widespread application of VUV radiation. Photochemical synthesis and the degradation of toxic substances may also be of interest. An extremely fast expanding field is the VUV-induced deposition of thin metal, dielectric, or semiconductor layers [92,93,94]. Especially in applications in which structured material deposition is desired, VUV-induced deposition techniques can provide straightforward, elegant solutions. Some narrowband VUV excimer sources can be applied as a source for advanced lithography applications [10,11,95]. In many of these applications, lasers are the obvious choice for laboratory experiments. However, for industrial applications in which large areas or large volumes have to be irradiated, incoherent excimer VUV sources driven by dielectric barrier discharges may have definite advantages, which could include high reliability, scalability to very high VUV powers, and reduced costs per VUV photon.

Chapter III

DESIGN AND EXPERIMENTAL SETUP

3.1 Lamp System

The experimental setup consisted of a discharge unit, a monochromator, a detector, gas inlet and outlet assembly, a pump system, and an RF power supply with impedance matching network. The system is schematically shown in Fig. 3.1. Fig. 3.2 shows a photograph of experimental setup. The discharge tube was connected to two flanges by two O-rings in order to be able to vacuum-seal the tube. The tube was fixed on a 3 3/8" six-way cross stainless steel cube, on which the monochromator and the photo detector were mounted. The monochromator was connected to the cube chamber by a flange adapter, where a window could be installed. The system could be either with a window or windowless. For Lyman-α line, a LiF or an MgF_2 window was used to transmit the radiation, because their cut-off wavelengths are 105 and 115 nm, respectively. On the other side of the cube, the gas inlet flange, a filter and a silicon photodiode, were mounted. The discharge was ignited with a RF power supply (Model RF5S, RF VII, Inc.) that consists of a 13.56 MHz RF generator and an impedance matching network. For increased efficiency, the impedance of the discharge and that of the RF generator need to be matched. For this purpose, an RF cable from matching network was directly connected to the anode and an RF wattmeter (Model 43 from BIRD Electronic Corp.) was used to measure the RF input power. An ac current probe (Mode P6021 from Tektronix Inc.) was looped around the cable to measure the discharge current.

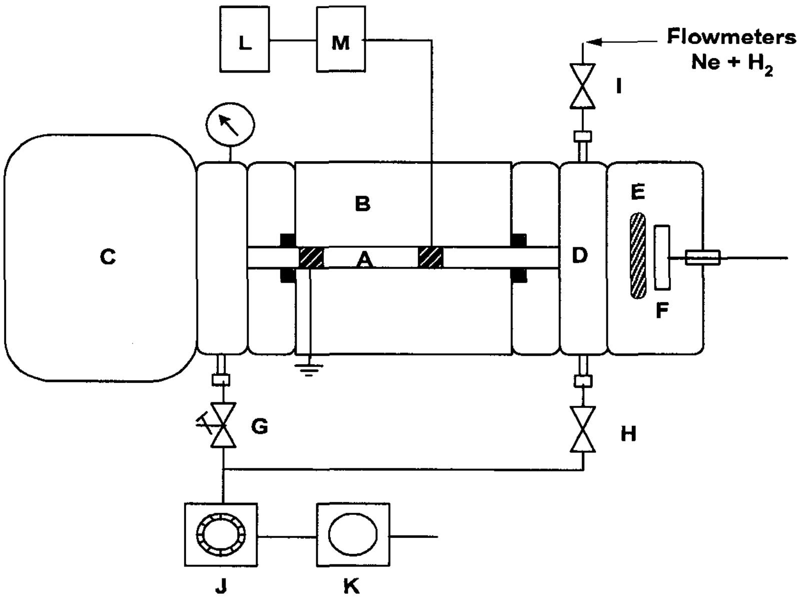

FIG. 3.1 Schematic drawing of the experimental setup. (A) quartz tube, (B) chamber, (C) monochromator, (D) gas inlet and outlet flange, (E) filter, (F) semiconductor detector, (G, H, I) valve, (J) turbo pump, (K) roughing pump, (L) RF generator, (M) matching network.

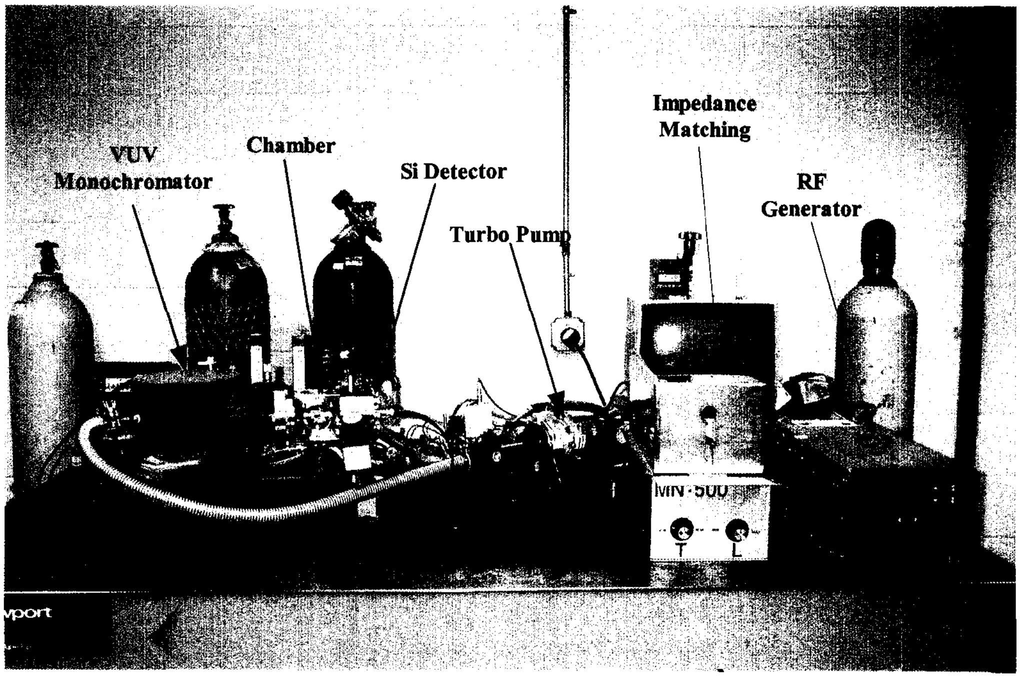

FIG. 3.2 Photograph of the experimental setup.

3.2 Discharge Tube and Electrodes

The discharge geometry used in our experiments was a cylinder, featuring a hollow dielectric (Al_2O_3 or quartz) tube and two copper-ring electrodes wrapped around the outer surface of the tube (FIG. 3.3). Both electrodes, anode and cathode, were water-cooled to keep the discharge tube at room temperature. In order to fit the tube inside the six-way cube, the dimension of the tube was 115 mm length, 8 mm OD and 4 mm ID. The diameter and thickness of tube could be varied. The area of the copper electrodes and the distance between two ring-electrodes were variable. Because the electrodes were out of the discharge volume, electrode erosion and contamination of the plasma with metal vapor could be avoided. This was the major advantage of this configuration [10,11,17].

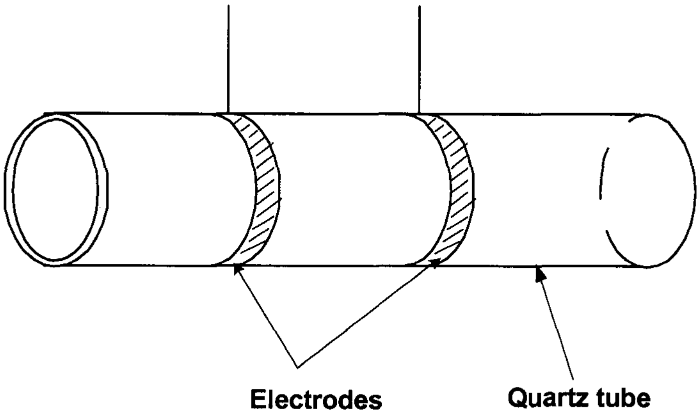

FIG. 3.3 Cylindrical DBD configuration with ring electrodes.

Due to the heating from the RF, both anode and cathode were water-cooled. In our experiment, the anode and cathode were specially designed, so that the water could circulate through the electrodes to keep tube at room temperature. The configuration of electrodes and discharge tube is shown as FIG. 3.4. O-rings were used to vacuum-seal the discharge tube and the flange.

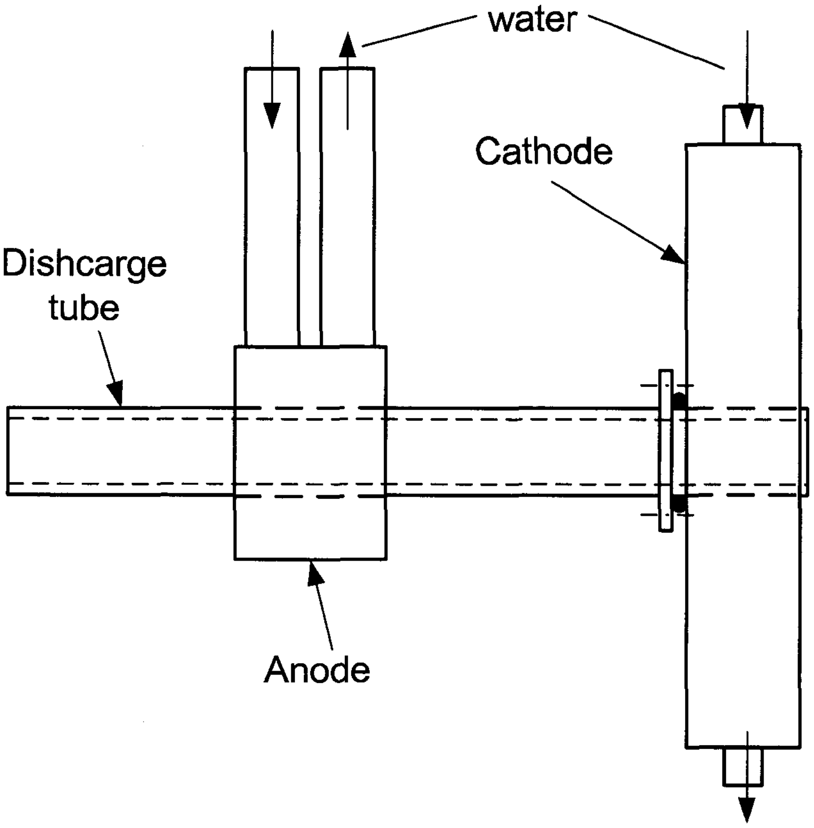

FIG. 3.4 The configuration of electrodes and discharge tube.

3.3 Spectral and Optical Power Measurement

The relative spectral distribution and the intensity of the radiation emitted from the discharge was measured with a VUV monochromator. The absolute optical power at 121.6 nm was measured by a special silicon detector with a filter. Figure 3.5 shows the measurement configuration, which also includes the gas mixture setup and vacuum gauge.

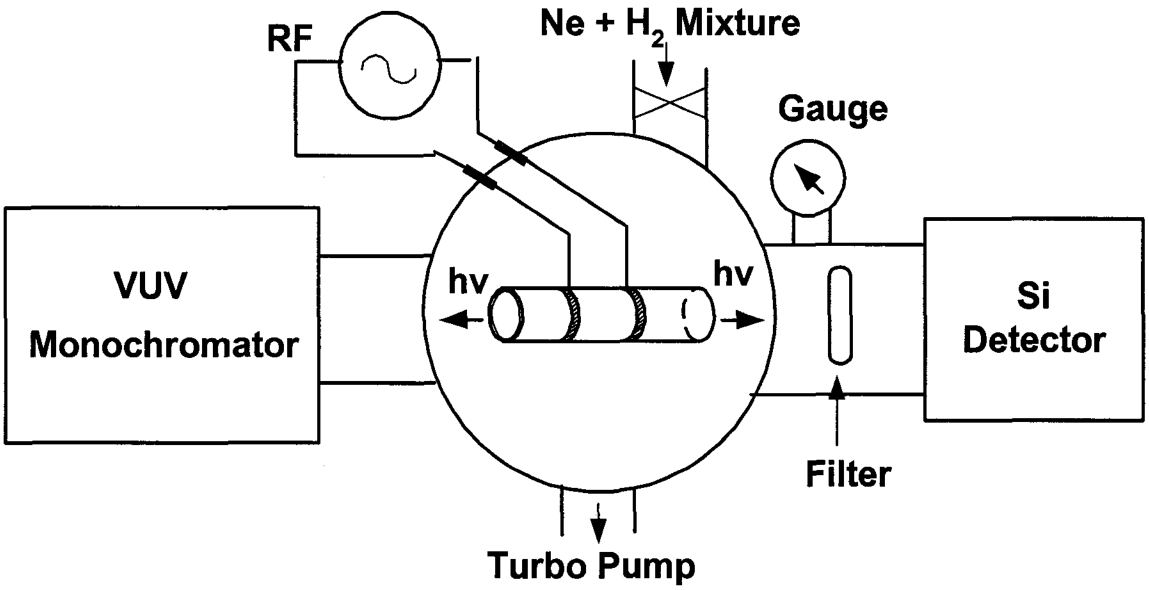

FIG. 3.5 Schematic of the measurement system.

3.3.1 Spectroscopy Setup

A 0.2 m focal length f/4.5 monochromator from McPHERSON (Model 234/302) was used for experiments. A 1200 g/mm type IV aberration corrected concave grating was used that had resolution of 0.1 nm and wavelength range form 30 nm to 550 nm. The grating rotation was controlled by a digital stepping drive or scan controller (Model 789A-3). Two cables were used to link the controller with rotation set. One was used to drive the motor, and the other one was auxiliary that feedback the position. The controller was connected to a computer with a RS-232 cable. Fig. 3.6 shows the schematic of spectral measurement. A detector assembly (Model 650) with a photomultiplier tube (PMT) was directly connected to the exit slit of the monochromator. The PMT tube was sensitive to a radiation wavelength range form 50 nm to 600 nm. The detector assembly was powered by a 1000 V DC power supply, which converted the photon energy into an electrical signal and amplified this signal. A coxical table connected the detector to a picoammeter, so that the amplified signal was measured. The piocoammter (Model 485, Keithley) had IEEE-488 interface that connected with a GBIP cable to the GBIP control mounted in the computer. Fig. 3.7 shows the photograph of experimental setup with monochromator and discharge chamber.

The radiation from the discharge passed through inlet slit and hit on the concave grating. After passing through the grating, a light beam with a specific wavelength left the exit slit and passed directly to a sodium salicylate coated vaccum-tight window, causing it to fluoresce. The fluorescence energy (at a wavelength of approximately 400 nm) passed through the window of the photomultiplier envelope and struck the photocathode surface. With the high voltage DC power supplied, the photocathode converted the light energy striking its cathode into an electrical signal (I) that was amplified enough to measure with the picommeter. The picommeter provides a current read out and at the same time sends the signal to a GBIP card in the computer. Software on the computer shows the signal strength on the screen and records it. The computer sends the signal to a scanning controller through an RS-232 connection, which drives the rotation of grating. Accordingly, the spectral intensity and wavelength were recorded.

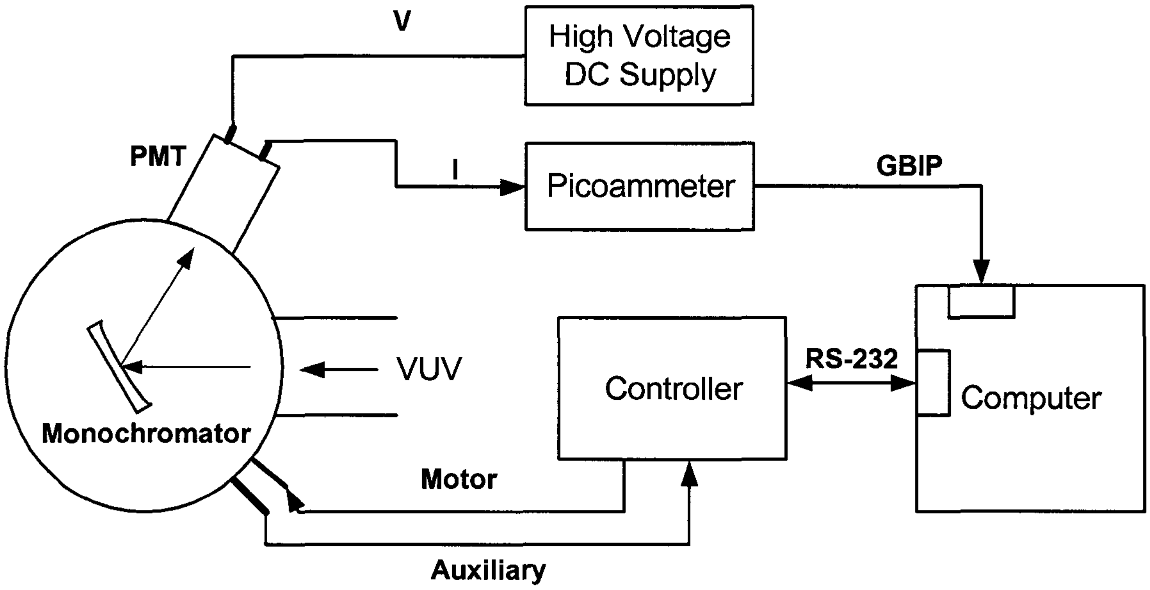

FIG. 3.6 The schematic of spectral measurement setup.

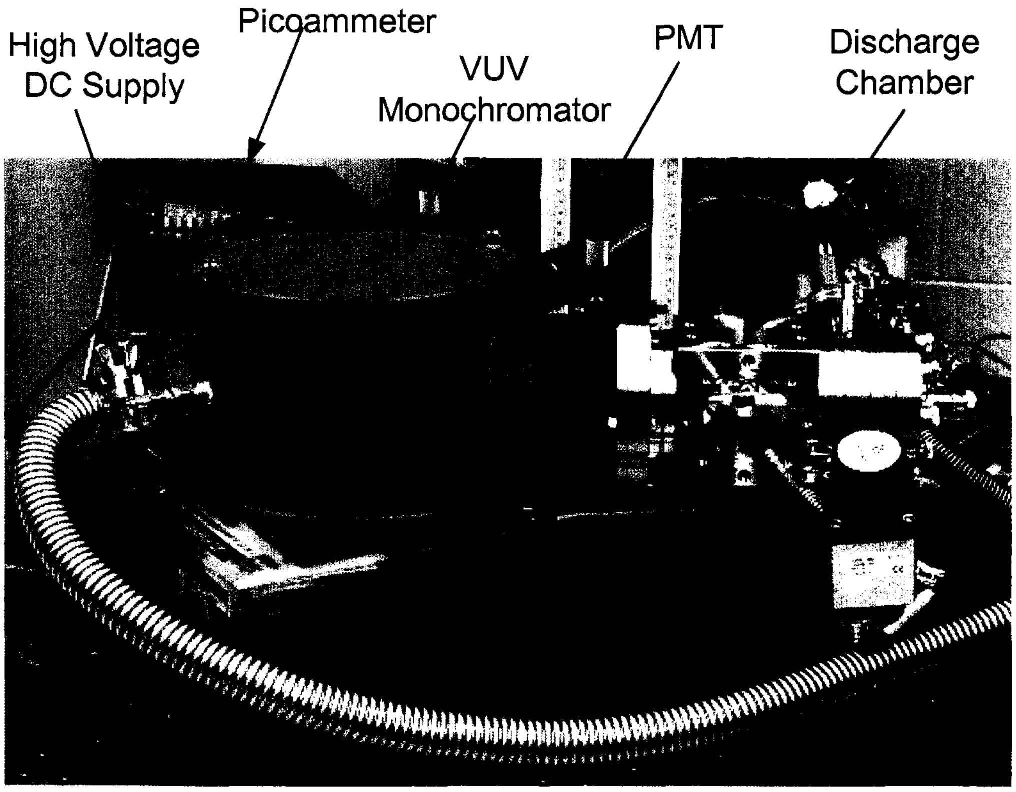

FIG. 3.7 Photograph of the discharge chamber and monochromator.

3.3.2 Absolute Power Measurement

The absolute power of VUV radiation was measured with a photodiode and a filter that selected the specific wavelength. The photodiode (Model SXUV-100, from IRD) was fabricated with an ULSI compatible process [96]. Fig. 3.8 shows the structure of this photodiode that measured VUV radiation intensity. It was an n-p photodiode, having 100% internal quantum efficiency and exhibiting long-term stability to VUV. PtSi front window diodes had been fabricated instead of silicon dioxide window, because the PtSi front window produced an excellent long-term stability and uniformity of responsivity for high level radiation.

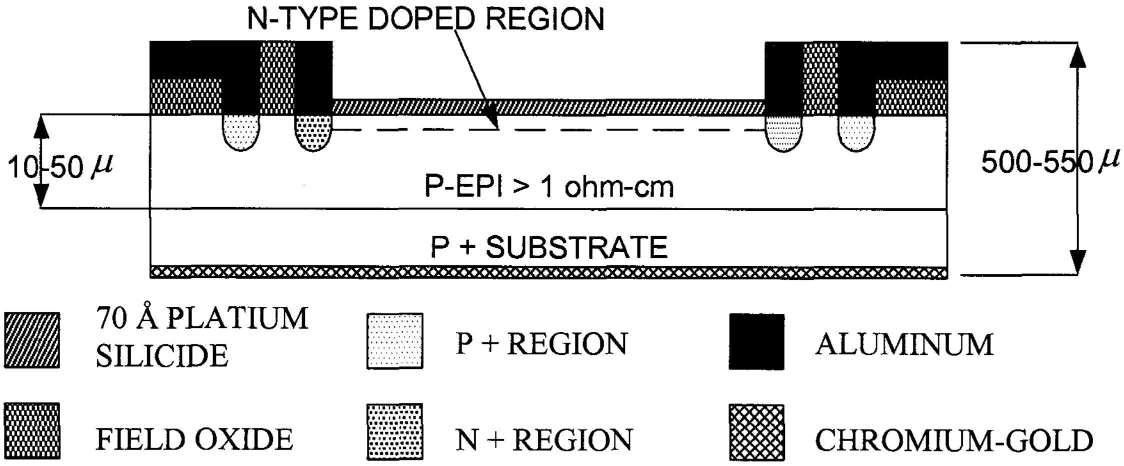

FIG. 3.8 Schematic diagram of a p-n junction photodiode with PtSi window.

The filter was a narrow band filter (Model 122-N-1D, from Acton Research Corp.) with peak transmittance of 15.3% at 119.60 nm and FWHM of 13.50 nm. Figure 3.9 shows the transmittance spectrum of the filter. Only the light with wavelength around 121.6 nm passed through and the light beyond that range was blocked. The photodiode and the filter were put inside the vacuum chamber and were hold with an electric feedthrough and a C-mount holder respectively (FIG. 3.10). The optical power intensity was measured by the picoammeter.

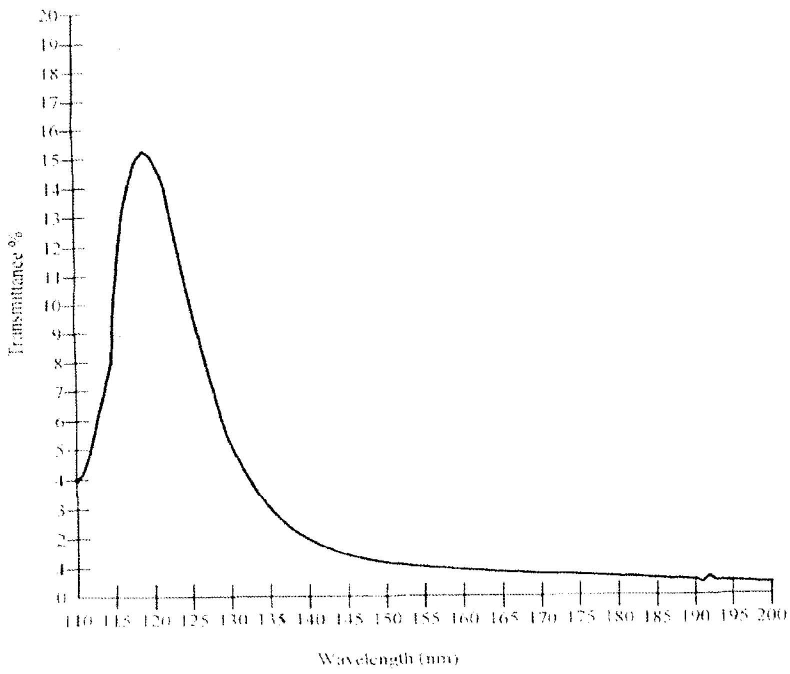

FIG. 3.9 The transmittance spectrum of a filter at wavelength from 110 nm to 200 nm.

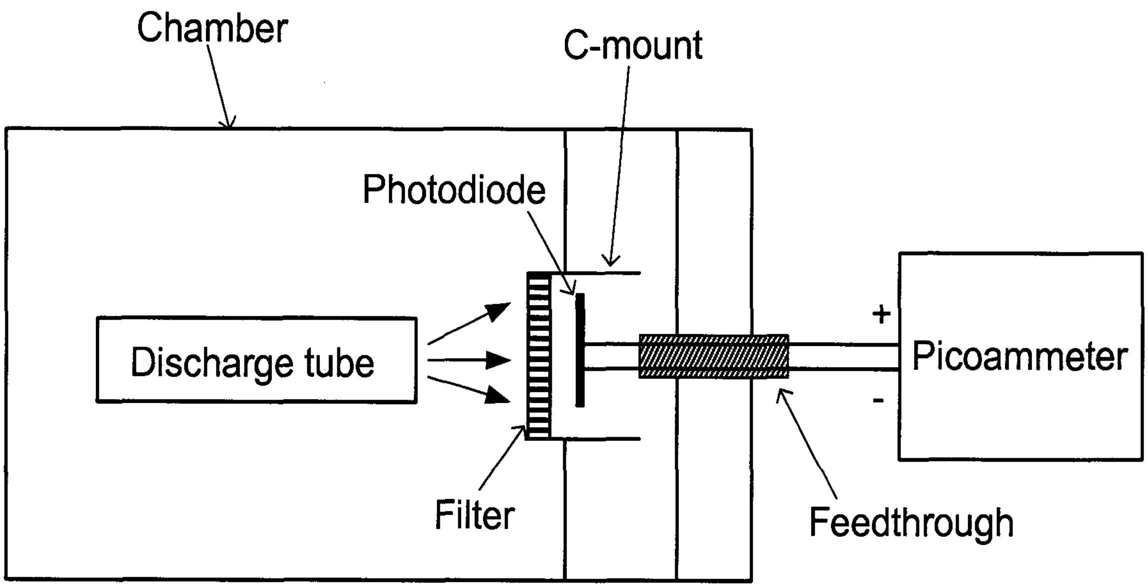

FIG. 3.10 The schematic of optical power measurement setup.

3.3.3 Transient Emission Measurement

The transient emission of Lyman-α was analyzed by the windowless VUV monochromator connected to the discharge lamp (Fig. 3.11). The detector was a scintillator-photomultiplier (Hamamatsu R6095) system with a time resolution of about 4 ns. The VUV radiation was detected by the photomultiplier through the entrance window coated with sodium salicylate. The plasma current was detected by the current probe (Tektronix P6021). Both emission pulses and discharge current signals were recorded by a digital oscilloscope (Tektronix TDS 3032). The waveforms of the radiation and current were saved on a floppy disk. By turning the monochromator to 121.6 nm wavelength, the temporal behavior of Lyman-α radiation was studied.

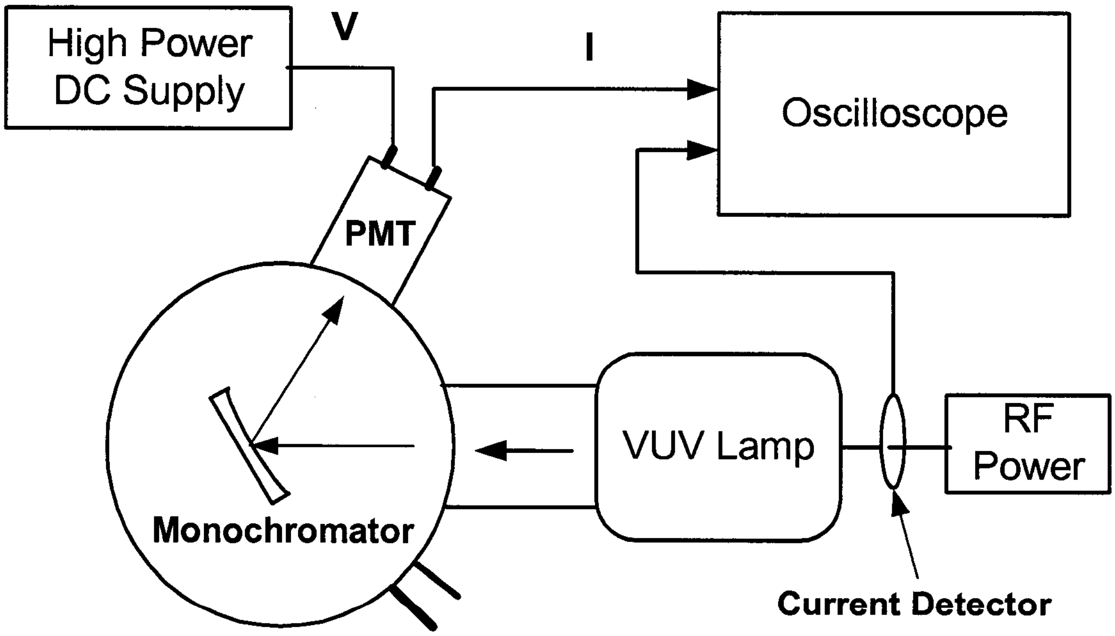

FIG. 3.11 The experimental setup for Lyman-α emission measurement.

3.4 Gas Mixing and Vacuum System

Before generating plasma, the discharge unit, monochromator, and detector were evacuated to 10^{-6} Torr. High vacuum was necessary before filling the neon and hydrogen gas, to avoid emission from impurities such as O, N, CO, CO_2, and so on. A mechanical pump and a turbomolecular pump were used to vacuum the system. The mechanical pump was a dry scroll mechanical pump (Varian, Model TriScroll 300), which could reach vacuum level of $1x10^{-2}$ Torr, and the turbomolecular pump (Varian, Turbo-70) could reach vacuum in a range from $1x10^{-2}$ to 10^{-9} Torr. The advantage of this pumping system was that it was oil free and kept the discharge chamber very clean. Three vacuum gauges were installed to measure the vacuum system. The Diaphragm manometer (Kurt J. Lesker) could measure the pressure range from 1 Torr to 1500 Torr. The 275 Mini-convection vacuum gauge (Granille-Convectron) measured the vacuum range from 1 mTorr to 1000 Torr. The Eyesys Mini-IMG gauge (Varian) measured the vacuum from 0.1 Torr to 10^{-9} Torr. With these gauges, we could monitor all the pressures form high vacuum (10^{-9} Torr) to atmospheric pressures.

A discharge was ignited at relative low pressure, such as 1 Torr to 100 Torr, because at high pressure the rf voltage was not high enough to breakdown the discharge. The RF voltage that ignited the discharge was dependent on pressure (*p*), electrode gap width (*d*), and type of dielectric material of the tube. After breakdown, the discharge was easy to maintain at high pressure. Usually the discharge was ignited at low pressure and gas was increased to desired pressure levels.

Two flow meters, one connected to high purity neon and the other to 1% hydrogen/neon mixture (research grade), controlled the flow rate and ratio of hydrogen to neon. A needle valve (Edwards, Model LV10K) and flow meters were adjusted together to control the flow rate and to maintain a constant pressure in the discharge tube. To obtain maximum radiation intensity, gas flow rate from 300 to 840 sccm was used.

CHAPTER IV

SOURCE CHARACTERIZATION

4.1 Discharge Modeling

4.1.1 The Processes

The purpose of the modeling was to optimize the parameters of the discharge breakdown process in such a way that the chemical species produced and VUV radiation were obtained with the greatest efficiency. Fig. 4.1 gives a schematic illustration of the discharge processes. Seven steps could be identified within the model: 1) the application of an RF electric field; 2) discharge breakdown by the electric field; 3) initiation and formation of a discharge channel; 4) the excitation of the atomic and molecular neon by the electrons; 5) neon excimer formation; 6) resonant energy transfer from neon eximers to molecular hydrogen and excited hydrogen; and 7) spontaneously excited hydrogen atoms emit the Lyman-α line.

The discharge was modeled as a homogenous plasma. When the RF electrical field was applied, the electrons were almost immediately in equilibrium with the applied field. The initial formation of the energetic electrons can be obtained when the RF voltage across the electrode gap exceeds the static breakdown voltage (V_{br}). The breakdown voltage is dependent on the gas pressure (p) and the gap distance (d). The relation is called Paschen's law [97]. The breakdown electric field, or Phachen field, corresponds with the breakdown voltage and is lower than the reduced field (E/n). The electrons get excited corresponding linearly with the reduced field E/n which reached a maximum of E_0/n during the time t_1 and decay with a time constants t_2.

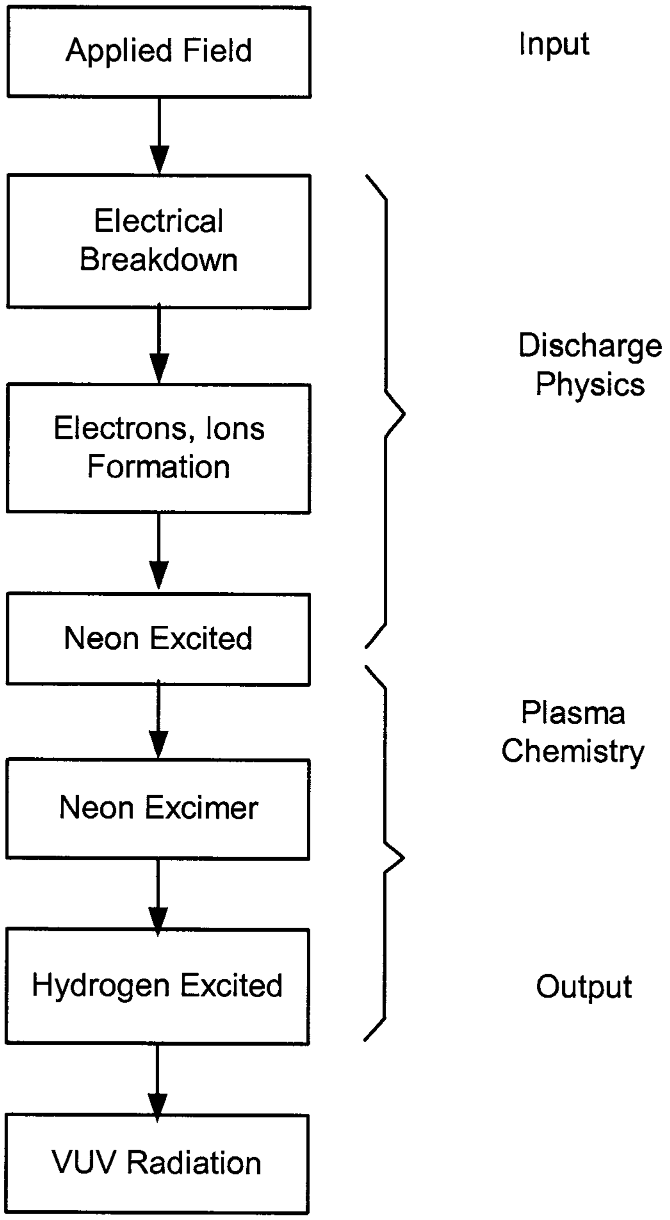

FIG. 4.1 Schematic illustration of the processes in the discharge.

The energetic electrons collide with the gas atoms and molecules and result in the production of other electrons so the total number of electrons increase, which is known as the avalanche multiplication process. In the avalanche the electron density becomes high enough to distort the initial electric field distribution. The field strength distortation results in the appearance of a cathode-directed streamer. The propagation of the streamer results in a growth of the conducting channel. The streamer propagates across the discharge gap and leads to the current pulse $j_e(t)$. The current pulse j_e leads, in turn, to excitation of neon ions. The high energy neon ions leads to chemical reactions, such as, disassoication, recombination, and photons emission. Lyman-α radiation is the final product of the whole process.

In this process, the electron and ion recombination leads to pulse width of τ, viz.,

$$\tau = 1/n_{e0}\rho_r, \tag{4.1.1}$$

where $n_{e0} = n_{i0}$ are the maximum electron and ion density and ρ_r is the recombination rate coefficient. The total current density is given by

$$j_{(t)} = e[n_{e(t)}\mu_e + n_{i(t)}\mu_i]E_{(t)}, \tag{4.1.2}$$

where n_e, n_i and μ_e, μ_i are the electron and ion densities and electron and ion mobilities, respectively. The corresponding energy density is given by

$$J_1 = \int_0^\infty E_{(t)} j_{(t)} dt. \tag{4.1.3}$$

In the discharge, there are a variety of species, such as Ne^*, Ne_2^*, H^*, and photons. The generation of various species can be determined by integrating by the rate equations. The efficiencies η_j for the generation of the various species j in a single microdischarge can be calculated as follows:

$$\eta_j = \frac{number\ of\ species\ j\ generated / cm^3\ in\ disch\mathrm{arg}e}{total\ energy\ input\ in\ disch\mathrm{arg}e / cm^3\ (J_1)} \tag{4.1.4}$$

The efficiency of Lyman-α generation is a function of pressure, total input energy, and the density of hydrogen. In our experiment, we measured the Lyman-α radiation intensity depended on pressure, input rf power and density of hydrogen.

In DBD discharge, the formation of excimer was viewed as a sequence of collisional energy exchanges. The high energy electrons ionize or excite the neon gas (Ne^+). And with three-body association neon molecular ions (Ne_2^+) form rapidly. Subsequently, a dissociative recombination reaction quickly forms an excited neutral (Ne^{**}) in a dissociating state; again with a three-body association reaction the excimer (Ne_2^*) forms. At high-pressure, the excimer formation processes are fast compared with the radiative decay time, thereby enabling the kinetic chain to produce a high density population inversion. Neon gas has two low-lying, but separate eximer states, both of which will radiate. These are the ${}^1\sum{}_u^+(O_u^+)$ state that dissocicates into ${}^3P_1$ and ${}^1S_0$ atoms and the ${}^3\sum{}_u^+(1_u, O_u^-)$ state that dissociates into ${}^3P_2$ and ${}^1S_0$. The radiative lifetimes of these two states are 2.8 ns and 11.9 μs, so the radiative lifetime of excimer neon is at least 11.9 μs.

The time-dependent electron current, neon excimer density, and excited hydrogen density are given as a function of time, with RF voltage (V_{rf}) also indicates (Fig. 4.2). Electron current *Je(t)* is spread over a significant fraction of the RF cycle, when significant voltages exists between the plasmas and the electrode.

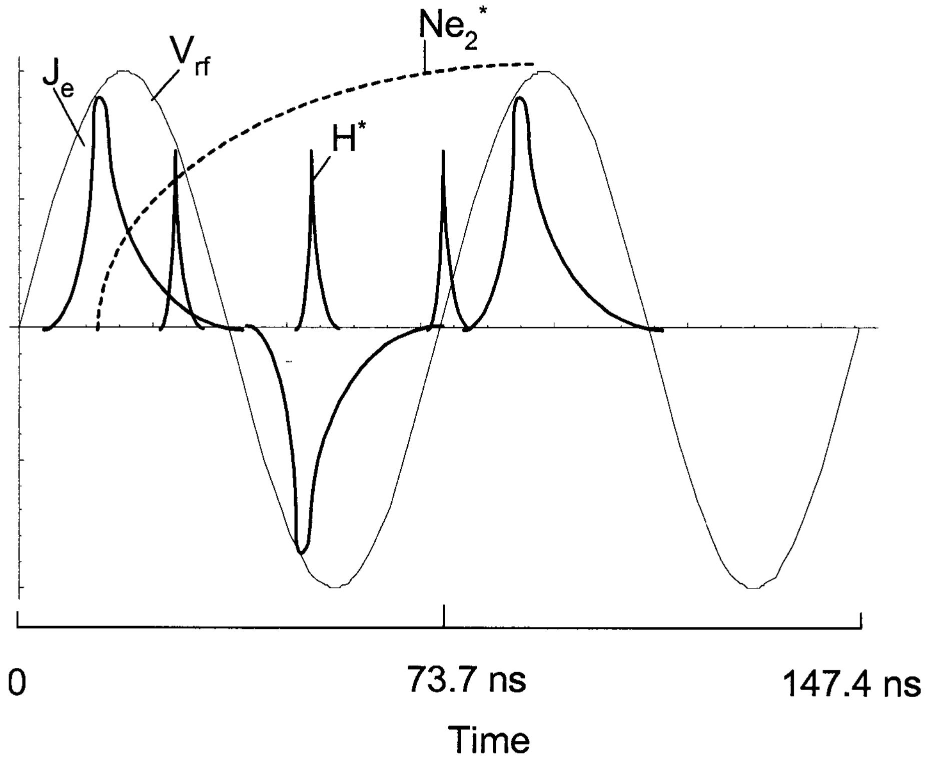

FIG. 4.2 The schematic illustration of electron current, neon excimer, excited hydrogen, and driving rf voltage.

In our experiment, assuming the applied RF voltage was 1000 V at a frequency of 13.56 MHz. With the rf cycle, the voltage increased from 0 to 1000 V in 9 ns. The neon at the pressure of 200 Torr broke down at 1000 V. The width of the electron current pulse was about 27 ns. This time is the characteristic time t_2, mentioned previously, and it depends on geometry and gas pressure. During this time, the energy transfer from electrons to neon atoms and the formation of neon excimer were very rapid, especially in high pressure with high three-body association reactions. The lifetime (> 11.9 us) of excimer was much longer than the cycle of the RF field, so the density of excimer was nearly constant when the plasma was in equilibrium. The energy of the neon excimer was resonantly transferred to the hydrogen molecular and hydrogen atoms were elevated to an excited state. The excited hydrogen had a very short decay time and transferred to a ground state emitting a nanosecond Lyman-α line. Since hydrogen atoms were exited at anytime, the Lyman-α radiation occurred continually and randomly and was not identical to the rf cycle. The pulses of the excited hydrogen atom with a width of nanoseconds were shown in Fig. 4.2.

5.1.2 Discharge Circuit and RF Matching

Our Lyman-α system is driven by an RF capacitive discharge. A complete description of this discharge plasma is quite complicated, even in the simplest plane-parallel geometry. We simplified the plasma as a uniform, symmetric model, so some analytical solutions could be obtained [98]. Here, we are not focusing on the dynamical mechanism of the plasma. We focus on the electrical features so that we can achieve high efficient power transfer and obtain a high power Lyman-α source.

The circuit of the discharge is modeled as shown in Fig. 4.3(a); where C_0 and R_p are the capacitance and resistance of plasma volume; C_s and R_s are the equivalent capacitance and resistance of two sheaths; and C_d is the capacitance of the dielectric layers between the electrodes. The model is further simplified as depicted in Fig. 4.3(b) with a discharge resistance R_D and a reactance X_D. So, the discharge model is considered as a load having impedance $Z_D = R_D + jX_D$.

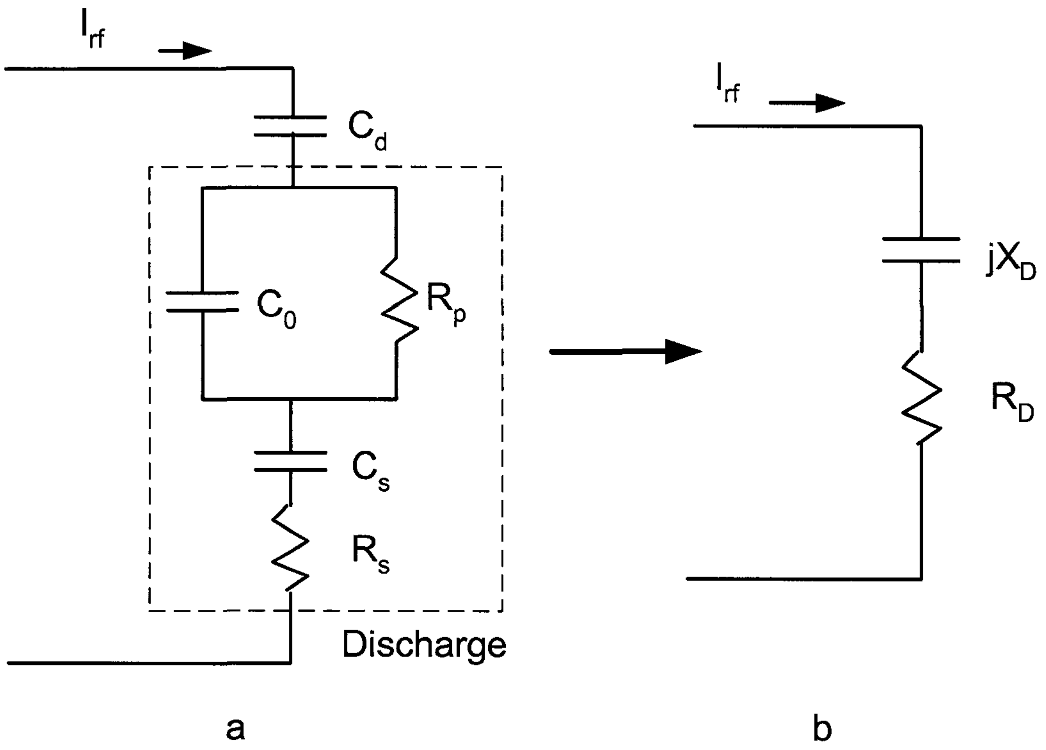

FIG. 4.3 A circuit model of the discharge.

If the discharge is driven directly by an rf power source, then generally power is not transferred efficiently from the source to the discharge. The connected power source Z_D, is modeled as a Thevenin-equivalent circuit, consisting of a voltage (V_T) source with a source resistance, R_T(Fig. 4.4). The time average power flowing into the discharge is

$$\overline{P} = \frac{1}{2}\mathrm{Re}(\widetilde{V}_{rf}\widetilde{I}_{rf}^{*}) \qquad (4.1.5)$$

where $\widetilde{V}_{rf}$ is the complex voltage across Z_D. Solving for $\widetilde{I}_{rf}^{*}$ and $\widetilde{V}_{rf}$, we have

$$\widetilde{I}_{rf} = \frac{\widetilde{V}_T}{R_T + R_D + jX_D} \qquad (4.1.6)$$

$$\widetilde{V}_{rf} = \widetilde{I}_{rf}\left(R_D + jX_D\right) \qquad (4.1.7)$$

Substituting (4.1.6) and (4.1.7) into (4.1.5), we obtain

$$\overline{P}=\frac{1}{2}\left|\tilde{V}_T\right|^2\frac{R_D}{\left(R_T+R_D\right)^2+X_D^2} \tag{4.1.8}$$

For fixed source parameters $\tilde{V}_T$ and R_T, the maximum power transfer is obtained by setting $X_D = 0$ and $R_D = R_T$. The maximum power supplied by the source to the load is

$$\overline{P}_{\max}=\frac{1}{4}\frac{\left|\tilde{V}_T\right|^2}{R_T} \tag{4.1.9}$$

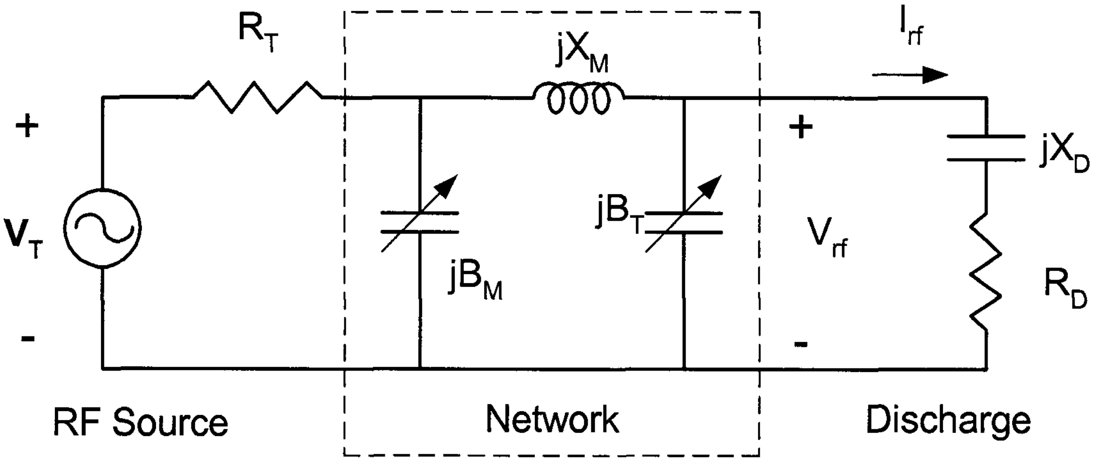

FIG. 4.4 Equivalent circuit for matching the rf power source to the discharge using an Π-network.

If maximum power transfer is obtained, then we say that the source and load are matched. Since the rf source and the load may not be matched directly, a lossless matching network is placed between them. In our system a “Π-network” was inserted between the source and the load. In the network, the inductive element is fixed, and two capacitors, which have reactance of B_M and B_T, are varied to achieve the matching point.

The advantage of this network is that it can match any discharge and provide added flexibility. Because R_D and X_D are actually functions of the discharge absorbed power (P_{abs}), we can apply the following equations

$$P_{abs} = \frac{1}{2} I_1^2 R_D \tag{4.1.10}$$

and

$$X_D = -\frac{1}{\omega\, C_{ab}}\ , \tag{4.1.11}$$

where I_1 is the conduction current across the plasma and C_{ab} is the plasma capacitance. Determine the current and voltage across the discharge to be

$$I_{rf}(t) = I_1 \cos\omega t \tag{4.1.12}$$

$$V_{rf}(t) = V_{rf} \cos\left(\omega t + \frac{\pi}{2} + \psi\right) \tag{4.1.13}$$

for a typical discharge $X_D >> R_D$, and we have

$$V_{rf} = \left(R_D^2 + X_D^2\right)^{1/2} I_1 \approx X_D I_1 \tag{4.1.14}$$

$$\psi = \tan^{-1} \frac{R_D}{X_D} \tag{4.1.15}$$

The time-average power absorbed by the discharge is

$$P_{abs} = \frac{1}{\tau} \int_0^\tau V_{rf}(t) I_{rf}(t) dt \tag{4.1.16}$$

$$= \frac{1}{2} I_1 V_{rf} \sin(\psi) \tag{4.1.17}$$

where $\tau = 2\pi / \omega$. Under matched conditions, the voltage and current at the source are in phase with each other, $\tilde{V}_T = R_T \tilde{I}_T$, given the power ($P_T$) supplied by the source,

$$P_T = \frac{1}{2}\frac{\left|\tilde{V}_T\right|^2}{R_T}. \tag{4.1.18}$$

For a lossless matching network, $P_{abs} = P_T$, we obtain

$$\left|\tilde{V}_T\right| = \frac{\left(R_D R_T\right)^{1/2}}{X_D} V_{rf} \tag{4.1.19}$$

under typical discharge conditions, where $\left|\tilde{V}_T\right| << V_{rf}$.

In our system, an rf wattmeter was placed between the source and the matching network to measure the time-averaged power, P_T. The forward power (P_f) and reflected power (P_r) were measured using the following relation

$$P_T = P_f - P_r. \tag{4.1.20}$$

When the system is matched, the reflected power is much less than the forward power. Hence, rf wattmeters cannot be placed between the discharge and the matching network to determine the power P_{abs} absorbed by the discharge. For a lossless matching network, $P_{abs} = P_T$, but in practical application there is a small fraction of source power lost due to the wire with which the matching inductor is wound. In our experiment, we considered the absorbed power equal to the source power. We maintained the ratio of reflected power to source power at less than 2%.

We measured the absorbed power P_{abs} to be 100 W, and V_{rf} to be 1500 V. Using a current probe, we measured the current I_l to be 0.6 A. The current waveform is shown in Fig. 4.5. From equation (4.1.10), we obtain

$$R_D = \frac{2P_{abs}}{I_1^2} = 555\ \Omega \tag{4.1.21}$$

From equation (4.1.17) we calculate

$$\sin(\psi) = \frac{2P_{abs}}{I_1 V_{rf}} = 0.22 \tag{4.1.22}$$

From equation (4.1.15), (4.1.21), and (4.1.22), we obtain

$$X_D = 2460 \ \Omega \tag{4.1.23}$$

Substituting (4.1.23) into equation (4.1.11), we calculate the discharge capacitance to be

$$C_{ab} = \frac{1}{X_D \omega} = 4.77 \ pF. \tag{4.1.24}$$

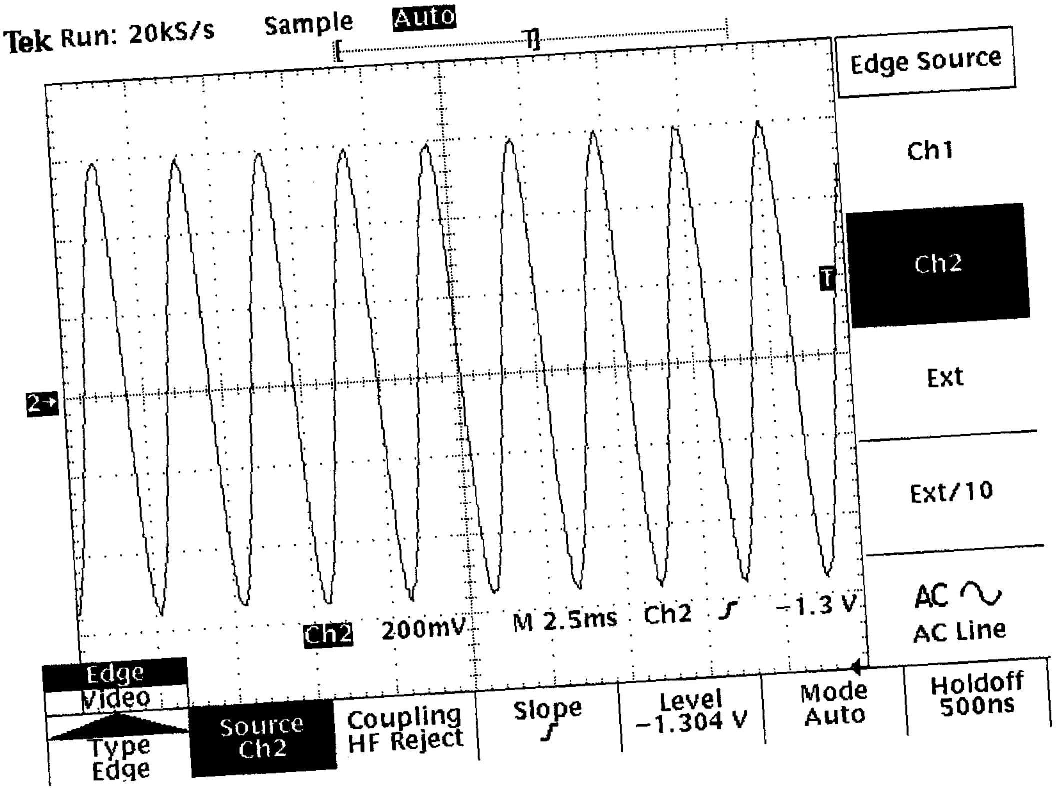

Tek Run: 20kS/s Sample Auto

Ch2 200mV M 2.5ms Ch2 ∫ -1.3 V

Type Edge

Source Ch2

Coupling HF Reject

Slope ∫

Level -1.304 V

Mode Auto

Holdoff 500ns

FIG. 4.5 The waveform of the discharge current, where I_1= 0.6 V and frequency f= 13.56 MHz.

We measured discharge current and voltage at different input powers, and using these parameters we calculated R_D, $sin(\psi)$, X_D, and C_{ab}. Table 4.1 lists these results. From the table, we conclude that these values provide a stable discharge.

In our discharge setup, there are two layers of dielectric between the electrodes. The capacitance of the dielectric layers is C_d and plasma capacitance is C_p. So we have

$$C_{ab} = \frac{C_d * C_p}{C_d + C_p} \tag{4.1.25}$$

C_d can be expressed as

$$C_d = \frac{\varepsilon_0 kA}{2d} \tag{4.1.26}$$

where ε_0 is the permittivity of free space; k is the relative dielectric constant; A is the area of the dielectric; and d is the thickness of the dielectric layer. When voltage V_{rf} is applied to the discharge setup, we anticipate the voltage load on the plasma will breakdown the discharge effectively. In order to achieve this, the capacitance (C_d) of the dielectric layers is made as large as possible in comparison with the voltage on the plasma capacitance (C_p). According to equation (4.1.26), there are three ways to increase C_d,

1) Increase the dielectric constant k. To accomplish this, we used high dielectric constant materials, such as quartz and alumina, for the discharge tube.
2) Increase electrode area, A. To achieve this, we designed electrodes that have enough area to efficiently produce discharge.
3) Decrease the dielectric thickness, d. In general, the thickness of dielectric layer should be as thin as possible, but in our system the dielectric tube was part of vacuum chamber, so it had to be thick enough to hold the pressure. We used a 1 mm thick tube and found it better than a 2 mm thick tube.

Table 4.1 Calculation of the discharge parameters from RF input power, discharge voltage and current.

RF Power (W)	I_l (A)	V_{rf} (V)	R_D (Ω)	Sin(ψ)	X_D (Ω)	C_{ab} (pF)
40	0.38	958	554	0.22	2460	4.77
60	0.46	1160	567	0.225	2457	4.78
80	0.54	1360	548	0.218	2458	4.77
100	0.60	1514	555	0.22	2461	4.77
120	0.66	1665	550	0.218	2462	4.77
140	0.71	1790	555	0.22	2459	4.77
160	0.76	1918	554	0.22	2462	4.77
180	0.81	2040	548	0.218	2458	4.78

4.2 Experimental Results

4.2.1 Spectra Measurement

Emission spectra were measured with a 0.2 m McPherson Scanning Monochromator (model 320). Intense Lyman-α radiation at 121.6 nm was observed as the only strong radiation across the VUV spectral region. Fig. 4.6 shows the emission spectrum at a pressure of 500 Torr with a neon gas containing 0.058% hydrogen and an input RF power of 200 W. Compared with the Lyman-α line, the other lines in the VUV spectrum are very weak and considered negligible. This means that the energy transfer from neon excimers to hydrogen is very efficient in the VUV region and such a discharge will be an ideal source for lithography and other applications. In our experiment, the emission line had a bandwidth of about 0.1 nm (FWHM) and was limited by the resolution of the monochromator, which has a resolution of 0.1 nm. Fig. 4.7 shows the Lyman-α peak intensity ranging from 121.5 nm to 121.7 nm. If a high-resolution monochromater were used, the measured linewidth would be narrower. Fig. 4.8 shows the spectrum of the 121.6 nm peak with a bandwidth of 0.03 nm from a Ne-H_2 mixture microhollow cathode discharge, which was measured by Dr. Kurt H. Becker in Stevens Institute of Technology.

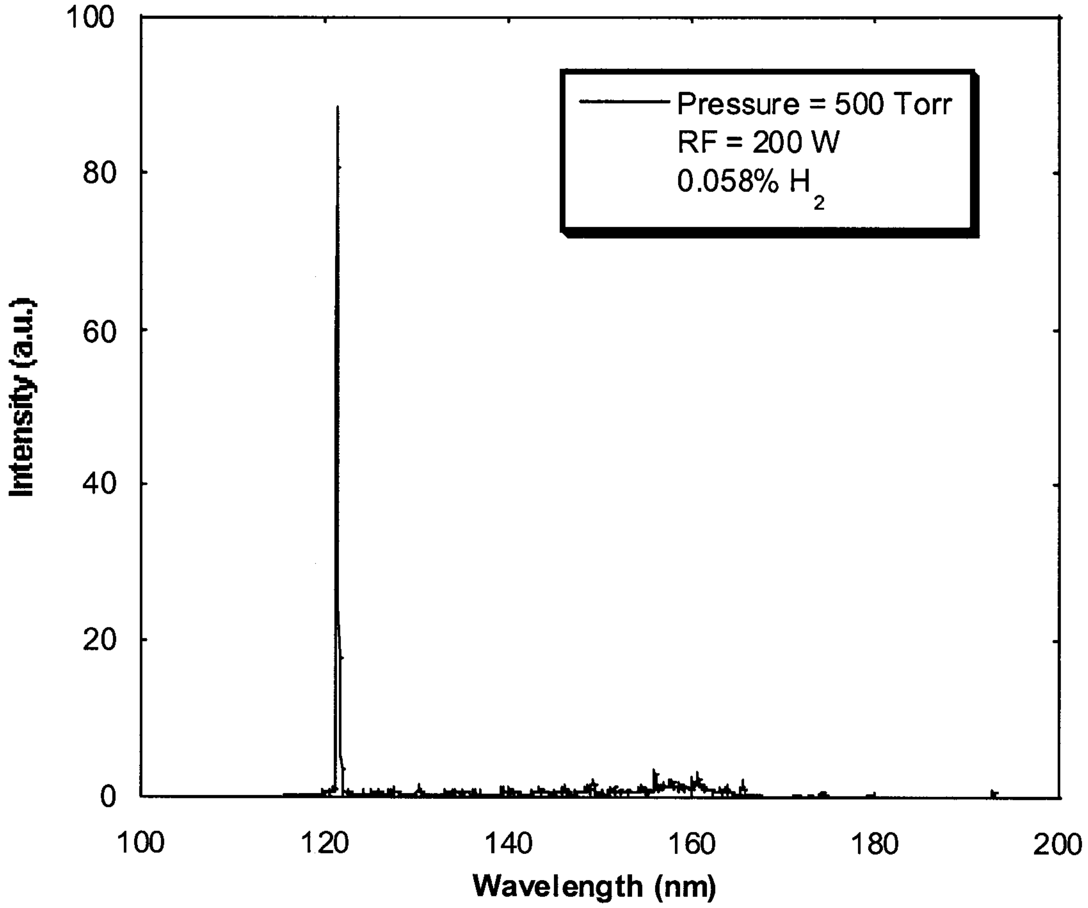

FIG. 4.6 Emission spectrum of neon/hydrogen mixture at a pressure of 500 Torr, with 0.058% H_2, and an rf power of 200 W.

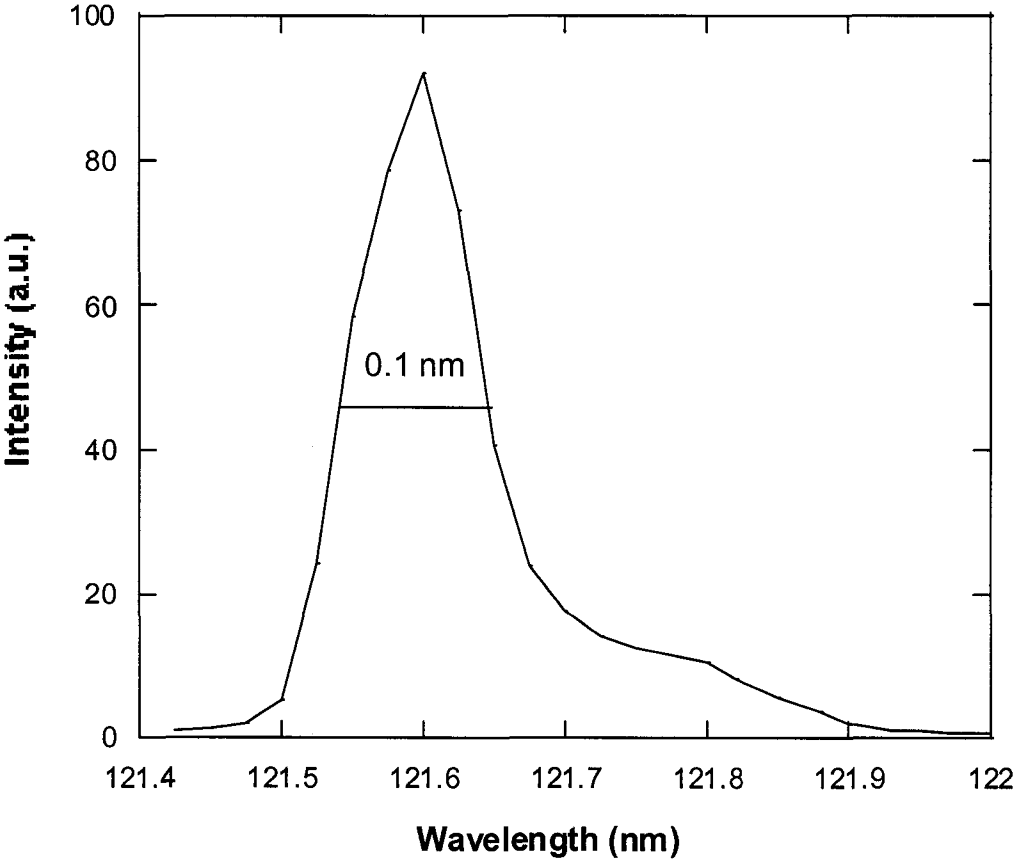

FIG. 4.7 The peak of a Lyman-α line with 0.1 nm linewidth.

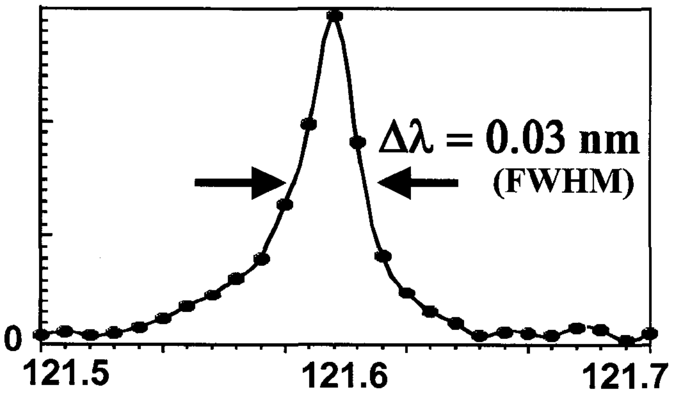

FIG. 4.8 Lyman-α peak with a bandwidth of 0.03 nm, which was measured by Dr. Kurt H. Becker in the Stevens Institute of Technology.

Gas mixtures

In order to obtain strong Lyman-alpha line radiation, the purity of the Ne and H_2 mixture is crucial. In our experiment, we used research grade neon (99.999%) gas and research grade H_2 (99.995%) gases. Before injecting the gas, the chamber was pumped under a high vacuum of about 10^{-6} Torr. Usually under low vacuums, background gases such as N_2, O_2, CO, CO_2, and He are present. If the discharge chamber was not under high vacuum before injecting the neon and H_2 mixture, the Lyman-α line was not strong and there would be some other radiation lines in VUV region. In addition to the Lyman-α line, we have observed several lines which originate from the presence of gaseous impurities in the neon supply and background gases (Fig. 4.9). Atomic nitrogen (N I) was detected at 113.4, 120, 149.2, and 174.3 nm. Atomic oxygen (O I) exhibited a partially resolved triplet at 130 nm. Atomic carbon (C I) lines occurred at 133, 156, 165.7, and 193nm.

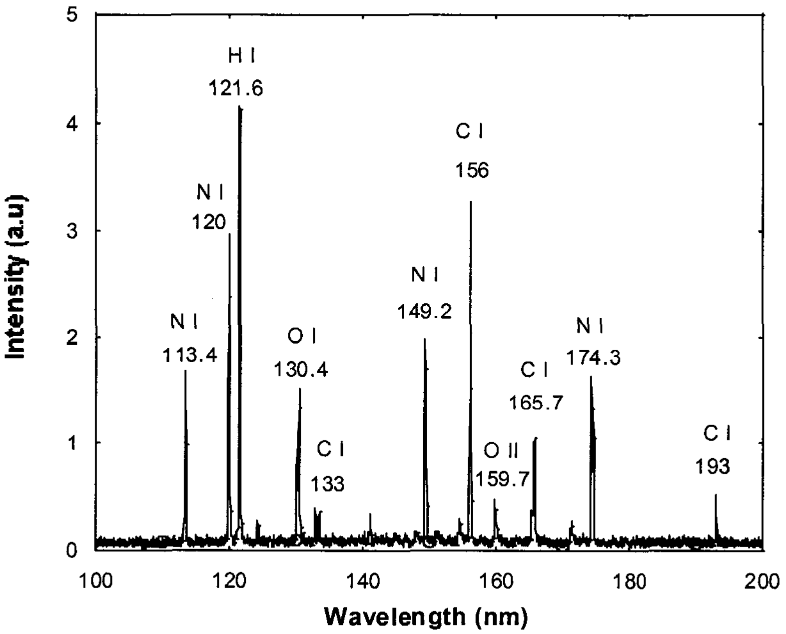

FIG. 4.9 Spectrum of VUV region of a neon and hydrogen discharge with impurities.

A hydrogen/neon ratio in the range of 0.03% to 0.12% was found to be the ideal range to achieve a Lyman-α line dominated spectrum. Beyond this range, the intensity of the 121.6 nm line would dramatically decrease, and other lines, 130 nm for oxygen and 156 and 165 nm for carbon, would increase. According to our experimental results, the optimum ratio for intense Lyman-α line is about 0.06% hydrogen to neon. Fig. 4.10 shows the Lyman-α peak intensity versus the hydrogen/neon ratio.

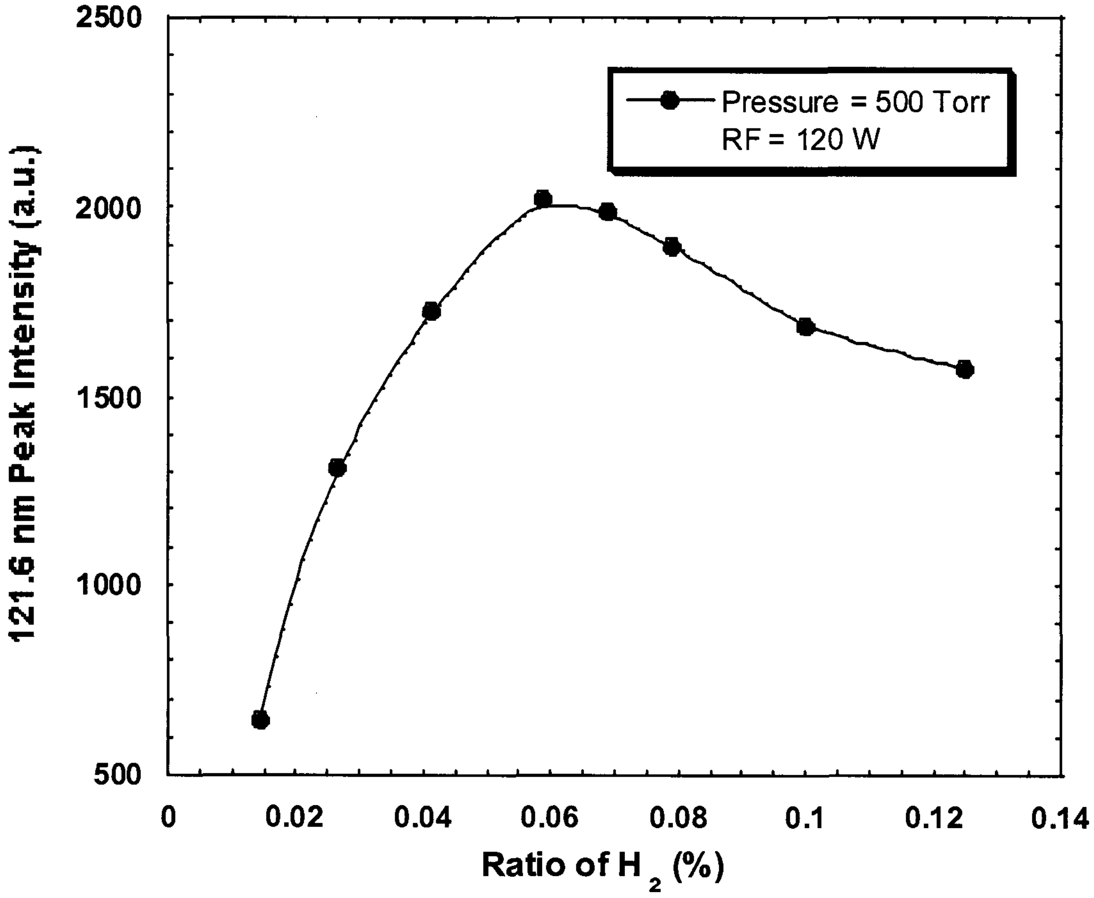

FIG. 4.10 The 121.6 nm peak intensity versus the ratio of hydrogen to neon, with a gas pressure of 500 Torr and an RF power of 120 W.

When the ratio of hydrogen to neon is low, the radiation intensity of Lyman-α is also low. This is due to an insufficient number of hydrogen atoms to be excited. When the density of hydrogen increases, the Lyman-α radiation intensity again decreases. This is due to atomic hydrogen recombination into hydrogen molecules. The recombination is more predominant at higher H_2 densities, which results in a faster decrease in the Lyman-α radiation.

Gas pressure

The pressure and electrode gap also influence the intensity of Lyman-α. From our experiment, the optimum range for the *pd* value is between 50 Torr cm to 1000 Torr cm. The mean electron energy is dependent on the product of gas density and discharge gap. In our setup, the electron energy of neon excimer discharge is dependent on *pd* value, which affects the formation of neon excimer. Since a small percentage of hydrogen is mixed with neon, the density of hydrogen also produces an effect on the discharge and altered the intensity of Lyman-α radiation. Fig. 4.11 shows the variation in Lyman-α peak intensity as a function of gas pressure when the electrode gap equals 2 cm and the hydrogen to neon ratio is 0.058%. A maximum intensity was obtained at 180 Torr. At low pressures the intensity of the 121.6 nm radiation is lower due to high breakdown fields and insufficient neon excimer generation. In the high pressure region, the intensity decreases with pressure. This drop is due to a quenching process that increases with increasing electron density and increasing excimer density.

The relative simplicity of changing the pressure-electrode gap product (*pd*) in our setup gives it a significant advantage over many other discharge types. Thus, in a fairly simple way, one can adjust a critical plasma parameter to optimize the yield of the excimer and Lyman-α emission.

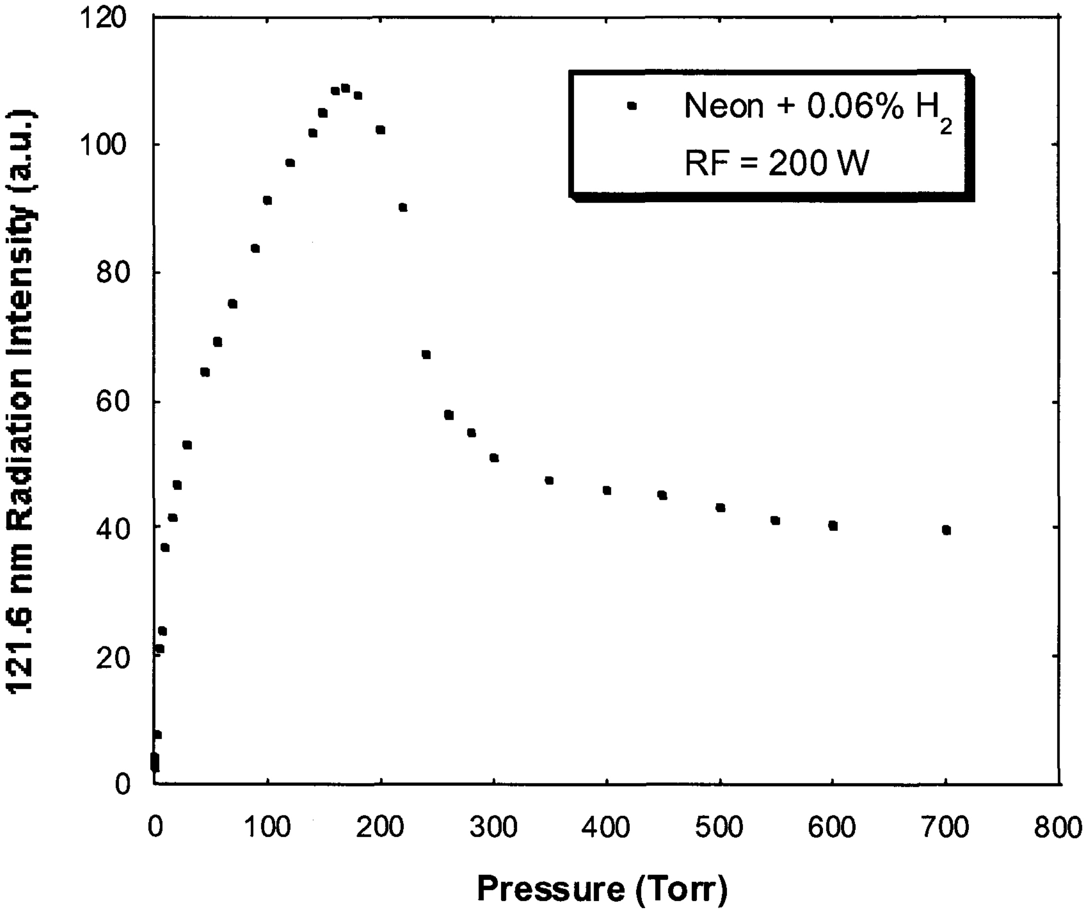

FIG. 4.11 The 121.6 nm peak intensity versus the pressure of the neon and hydrogen mixture.

4.2.2 Optical Power Radiation Intensity

The absolute intensity of the Lyman-α radiation was measured using a silicon photodiode (IRD company, model SXUV-100), which has a 1 cm x 1 cm active area and a 0.01 A/W responsivity at 121.6 nm. A narrowband filter located between the discharge unit and the detector was used. It has a transmission efficiency of 15% at 121.6 nm.

Using the current value on a picoammeter, we can calculate the radiant emittance, radiant intensity, and optical power. Figure 4.12 shows the setup that we used to calculate those values. The radiant emittance on the photodiode can be easily calculated as follows,

$$I = Q / A, \tag{4.2.1}$$

where Q is the flux on photodiode and A is area of photodiode.

The absolute total power is quite difficult to measure because it is difficult to actually collect all the radiation from a lamp and direct this to a suitable measuring device. We calculated the absolute power using a mathematical integration over a surface area which incorporated the detector surface and upon which essentially all the radiation from the lamp fell. In our experiment, the light source in the discharge was calculated as a line source.

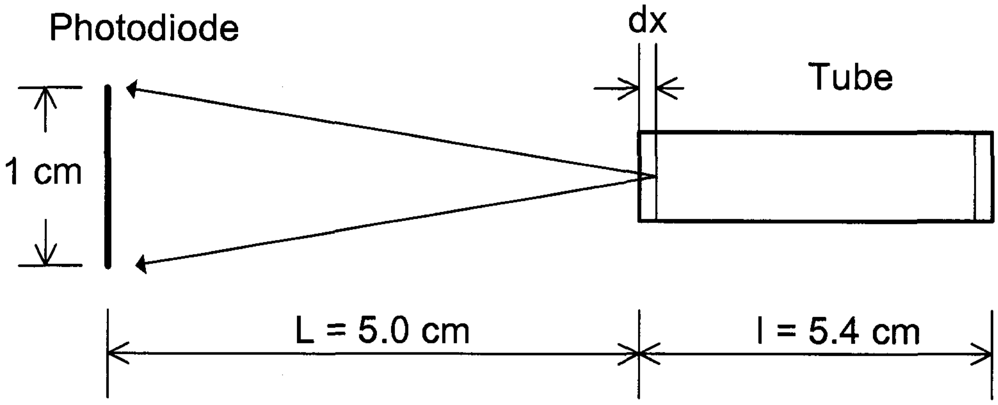

FIG. 4.12 The setup of the discharge to calculate the radiant emittance, radiant intensity, and optical power.

First, we divide the tube into many slides. Each slide has the width of dx and the optical power of dp. Giving

$$dp = \frac{W}{l} dx \tag{4.2.2}$$

where W is the total optical power and l is the length of source. The detector will obtain optical power of dp from each slide. Giving

$$dI = \frac{dp}{4\pi(L+x)^2} \tag{4.2.3}$$

where L is the distance from the detector to the front end of the discharge. The radiant emittance on the photodiode is calculated as integration of the power from all of the slides.

$$I = \int dp \tag{4.2.4}$$

$$= \int \frac{1}{4\pi(L+x)^2}\frac{W}{l}dx \tag{4.2.5}$$

$$= \frac{W}{4\pi\, l}\int_L^{L+l}\frac{1}{(L+x)^2}dx \tag{4.2.6}$$

$$= \frac{W}{4\pi * L(L+l)} \tag{4.2.7}$$

So the discharge has total optical power (4π) of

$$W = 4\pi * L(L+l)I \tag{4.2.8}$$

If $L = 5.0$ cm and $l = 5.4$ cm, then we have

$$W = 653 \times I\,. \tag{4.2.9}$$

The current measured from the picoammeter is $i = 15$ μA, the responsivity is $R = 0.01$ A/W. After including the loss from the filter, we had a radiant emittance of

$$I = i/R \times \textit{filter transmittance}$$

$$= i/R \times \frac{100}{15} = 15/0.01 \times 100/15 = 10 \;\; mW/cm^2\,. \tag{4.2.10}$$

So the total power will be

$$W = 653 * I = 6.53 \ (W). \tag{4.2.11}$$

Figure 4.13 shows total optical power variation versus RF input power from 50 W to 900 W at 200 Torr gas pressure, 0.06% H_2 gas mixture, and a gas flow rate of 660 sccm. A total radiation power of 8 W at 800 W of RF input power was obtained. The emission intensity at this power was 12.3 mW/cm^2 at a distance of 5 cm between the detector and the front edge of the source. The maximum electrical to optical conversion efficiency is 1.65 % when the RF input power is approximately 200 W. The VUV output increases with increasing input energy due to the corresponding increase in the electron density. But if the density increases significantly, the VUV efficiency drops due to quenching collisions of excited species with electrons.

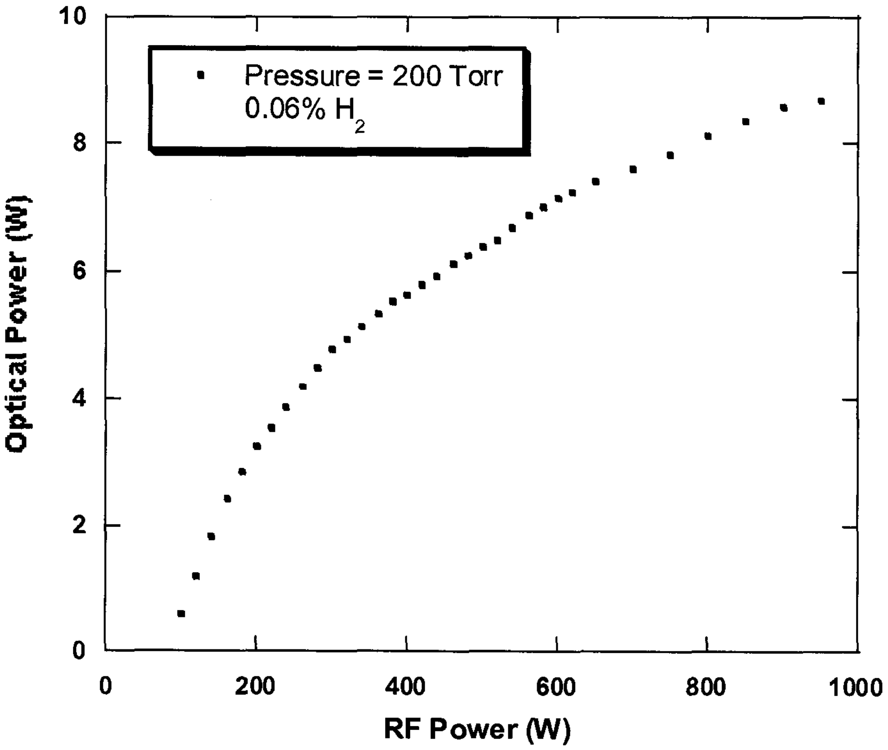

FIG. 4.13 Total optical power dependence on the input RF power at a pressure of 500 Torr.

4.2.3 Stability

Power stability is an important criterion for lamps used in lithography applications. Preliminary tests showed that our source was capable of continuous operation over a 24 hour period at an RF input power of 120 W and total optical power of approximately 1.8 W (FIG. 4.14). The average emission intensity on the detector was 3.34 mW/cm^2. During the 24 hours of operation, the power fluctuation was less than ±2% without significant power degradation.

Due to collisional momentum transfer between the oscillating electrons and the neutrals, some portion of the power deposited in the bulk plasma causing heating. Heat generated in the high-pressure non-equilibrium plasma wastes energy and often causes an unfavorable temperature rise in the discharge fields. In the DBD discharge setup, most of the input power is selectively transferred to the dielectric electrode. This is because microdischarges spread into a surface discharge on the dielectric wall, covering a much larger area than the original filament diameter. In our system, the temperature could reach over 1000 °C. Such high temperatures could significantly damage the copper electrode and the quartz tube, so water-cooling of the system is necessary. Both electrodes were equipped with water-cooling circuits, and the temperature was controlled appropriately for better operating conditions. With water-cooling, the discharge tube can run hundreds of hours and electrode life is almost unlimited. Factors that affected the lifetime of tube are deposition of impurities, such as carbon from chamber, and ion bombardment.

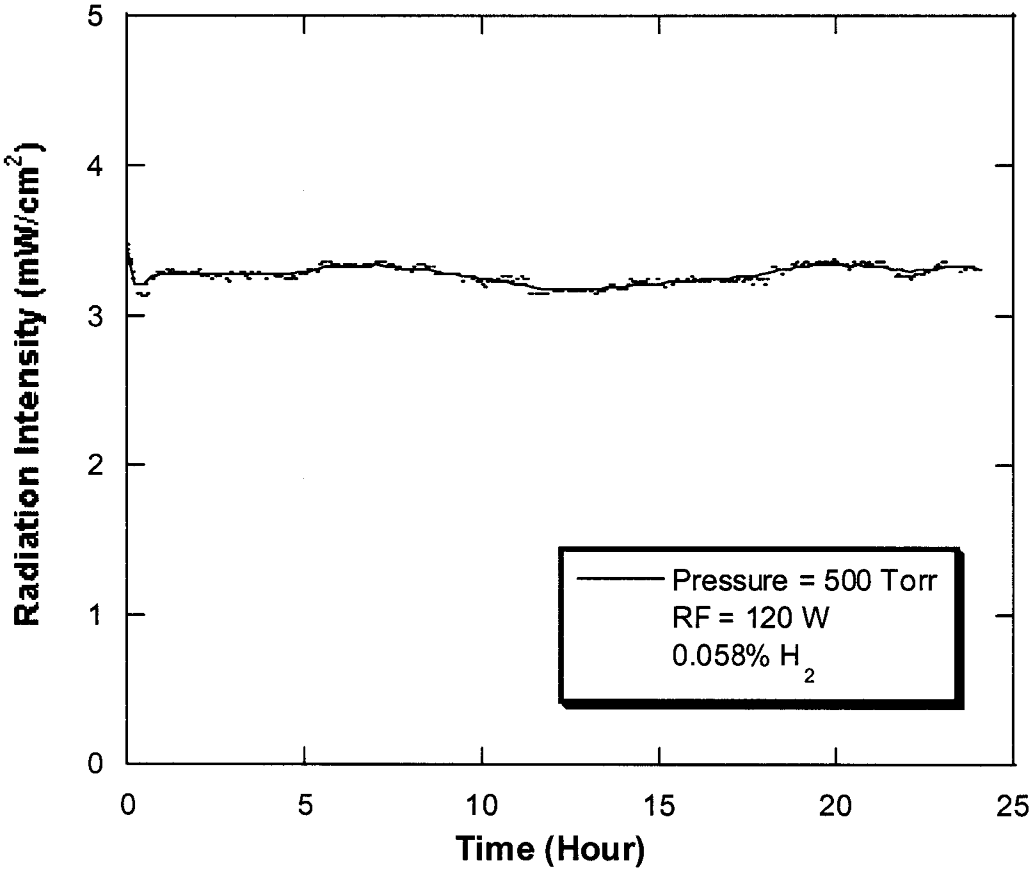

FIG. 4.14 Radiation Intensity versus operating time at a pressure of 500 Torr, an RF power of 120 W, and 0.058% H_2.

4.2.4 Transient Measurement

The transient emission of Lyman-α was measured with the monochromator-photomultiplier system as described in Chapter 3. We set the monochromator at a wavelength of 121.6 nm, so only light at that wavelength could reach to the photomultiplier. Electrons emitted from a photoemissive cathode traveled to the anode, which was maintained by a high electric potential. The electric potential in turn amplified the initial electron density to a current that could be measured using digital oscilloscope.

The oscilloscope registered the transient current pulses that were correspondent with the transient Lyman-α emission. Figure 4.15 shows the waveform of rf current and the current pulses from the photomultiplier with a time range of 8 x 10^{-7} s. The Lyman-α peaks occur continually and randomly, and it is not identical with RF phase. That is same with the modeling result we mentioned prevously. Figure 4.16 shows the Lyman-α peaks without the RF waveform. From our experiment, we found the density (peaks/second) and the average intensity of peaks increased with input power. That means the intensity of Lyman-α emission is dependent on both the peak density and intensity. Figure 4.17 shows a single peak of Lyman-α radiation with a width (FWHM) of 4 ns that is identical to the decay time of excited hydrogen atoms (H*).

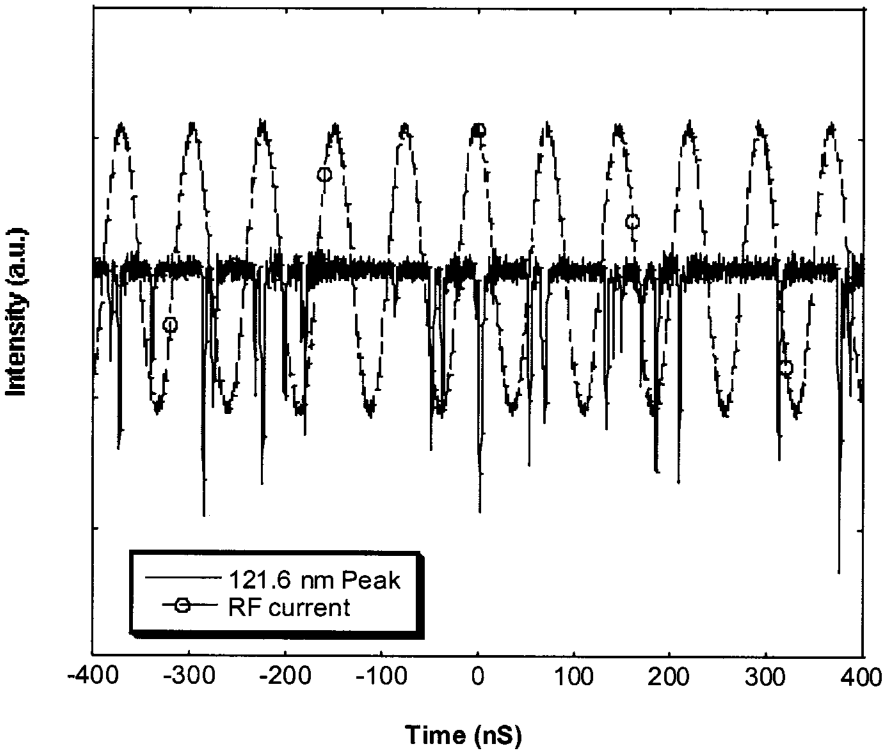

FIG. 4.15 The waveform of RF current and transient pulses of 121.6 nm peaks.

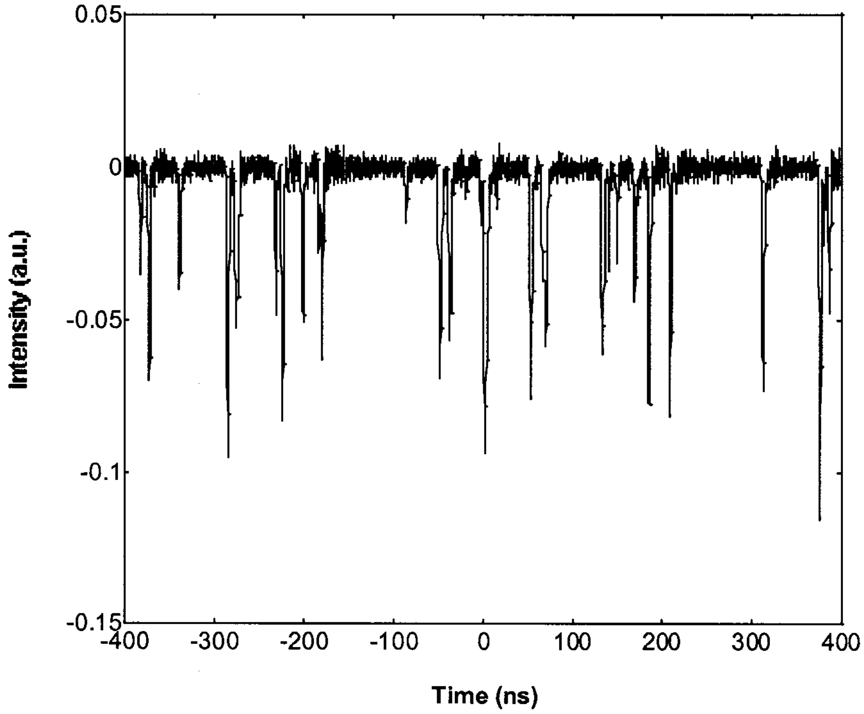

FIG. 4.16 The transient pulses of 121.6 nm radiation.

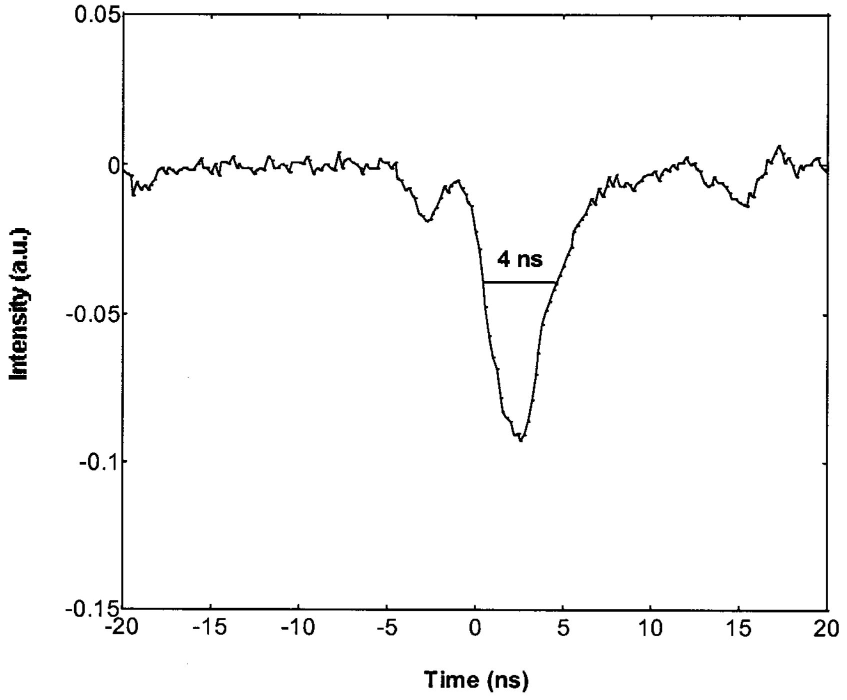

FIG. 4.17 Single pulse of 121.6 nm.

4.2.5 Beam Profile

Beam profile was measured to identify the emission intensity across the beam cross section. At low pressures, the tube was filled with the discharge, and the whole section had a nearly uniform intensity. As the pressure increased, the discharge became restricted toward the center and the intensity in the center area was much higher than the surrounding area. The front view of the discharge appeared like a 1~2 mm diameter disk, and the side view was a line source. If the pressure continually increased, the discharge would shrink to a small filament on the tube center. This change also indicate that the discharge mode transited form a homogeneously radiating glow discharge to a microdischarge dominating silent discharge. Figure 4.18 shows the front view and top view of discharge that was generated in an 8 mm o.d. x 6 mm i.d. quartz tube at a pressure of 200 Torr with 100 W of input RF power.

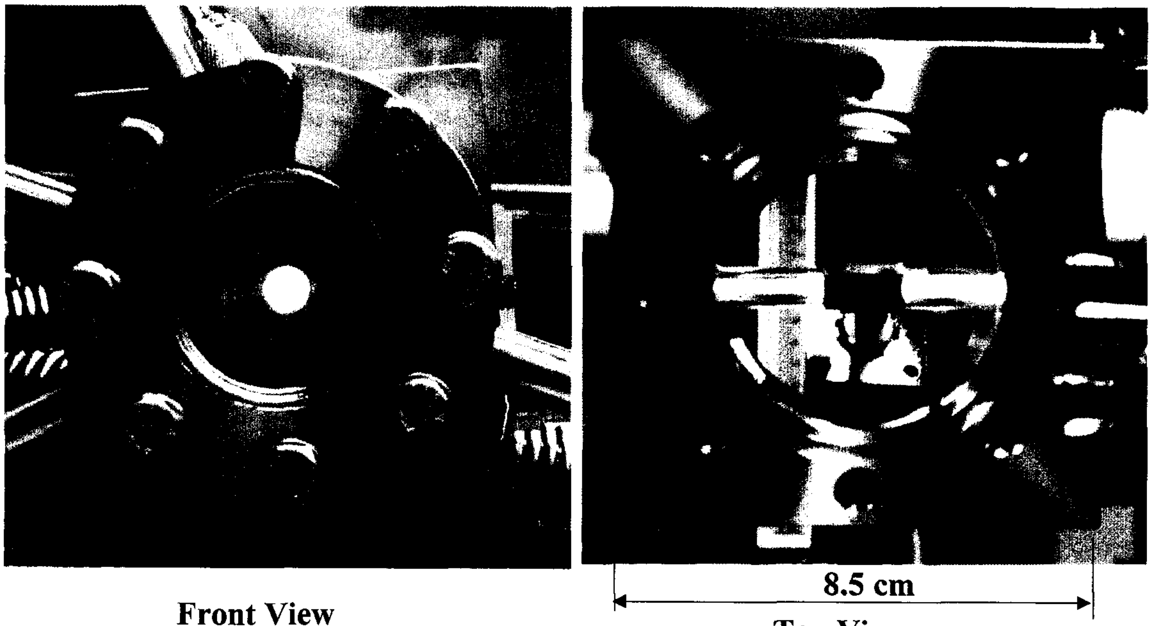

Front View

Top View

FIG. 4.18 Picture of the discharge in a quartz tube.

The beam profiles were measured using a beam profiler based on the visible light generated in the high-pressure discharge. Fig. 4.19 shows the two-dimensional (2D) and three-dimensional (3D) beam profiles at 500 Torr. From the 2D-profile, it can be seen that the most intensive radiation was at the center of discharge tube with a spot approximately 2 mm in diameter. The distribution of the discharge was Gaussian.

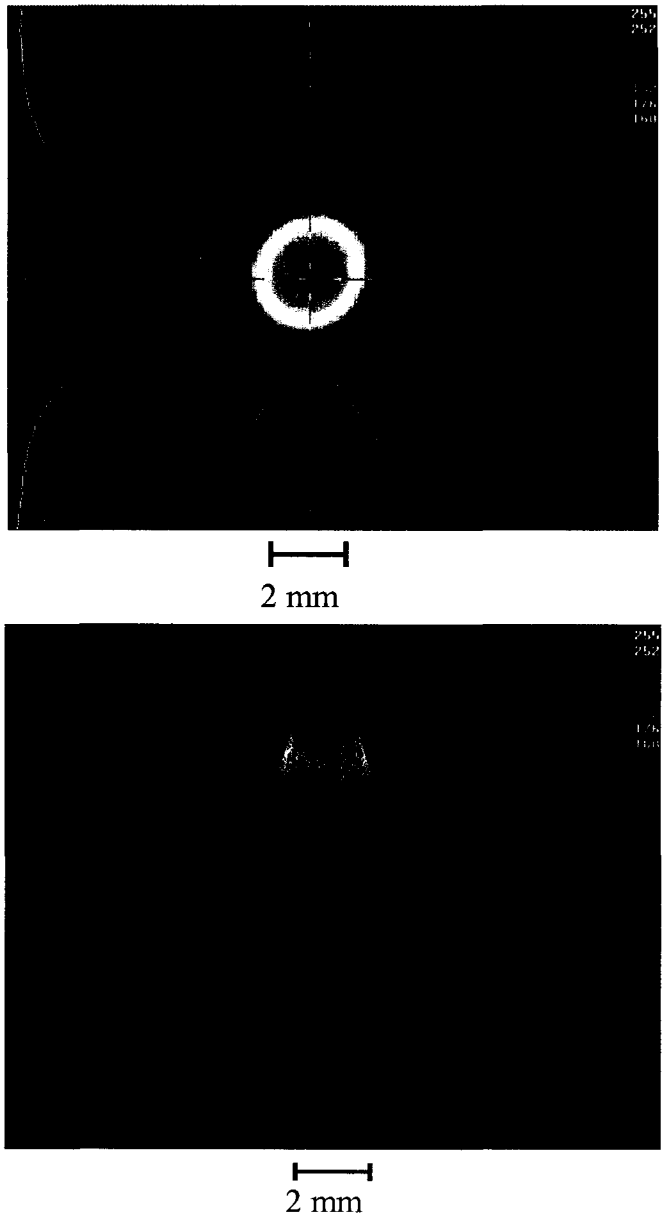

FIG. 4.19 2-D (up) and 3-D (down) beam profiles at high pressures.

4.3 Simulation

XOOPIC is object-oriented two-dimensional relativistic electromagnetic particle-in-cell (PIC) code developed at the University of California at Berkeley[99]. The XOOPIC code can handle electrostatic and electromagnetic simulations and relativistic and non-relativistic particles. It has been used to simulate a wide range of challenging problems, including plasma [100], ion implantation, high-power microwave devices, and next-generation particle accelerators [101].

The program simulates plasma experiments by modeling the plasma as discrete macroparticles interacting with an EM field at points on a grid. Given initial and boundary conditions, the program solves Maxwell's equations and determines macroparticle positions after each discrete time step. The XOOPIC code has implemented Cartesian and Cylindrical geometries. Our discharge structure has a cylindrical (r-z) geometry, as shown in figure 4.20, and can be modeled using the XOOPIC program. The simulation geometry was a 2-D cylindrical region with a radius of 8 mm and a tube length of 45 mm. The anode and cathode were located outside the dielectric tube and each one had a width (w) of 10 mm. The distance between two (g) was 15 mm. The thickness of the tube wall (d) was 1 mm. The boundary was closed with dielectric material. In our experiment, we downloaded and installed the XOOPIC software in a Linux operating system. According to the simulation model, we coded the input file and ran the simulation.

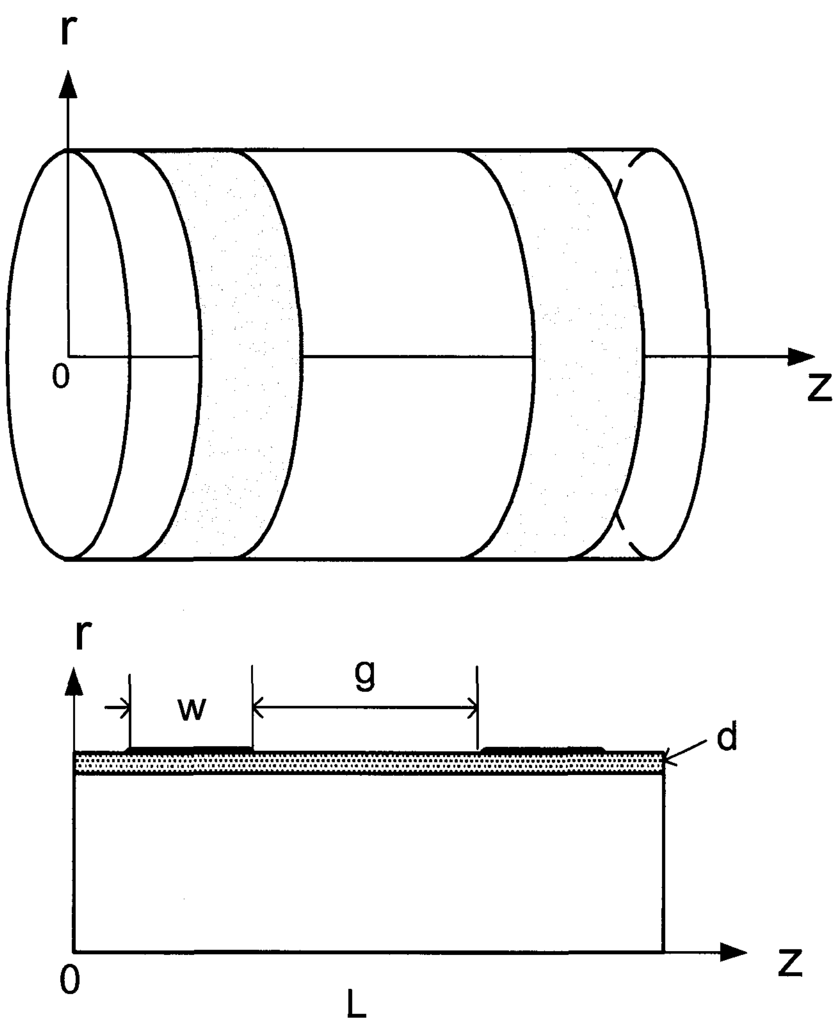

FIG. 4.20 2-D Cylindrical geometry and simulation model parameters.

The discharge was simulated using XOOPIC code with an RF voltage, which has a frequency of 13.56 MHz. Results of the simulation were the electric field, electron energy, and the electron and ion density-profiles. These values were taken after 10^{-6} seconds, which is approximately thirteen times of the RF period. Over this time, the values did not change significantly, so we considered it was approaching the steady state. The initial input parameters were an RF voltage of 1000 V in a neutral neon gas with a pressure of 100 Torr. Initially, the electrons and ions were distributed evenly over the whole volume with a density of 10^{15} cm^{-3}. Figures 4.21 and 4.22 show this initial distribution of electrons and neon ions in r-z cylindrical geometry. When an electric field was applied, electrons gradually moved to the center of the cylinder, so the density in the center area was much higher than the area near the tube wall (Fig. 4.23). The high-energy electrons collided with the neutral gas and ionized the neon atoms, thus more ions were formed and more Lyman-α radiation was emitted from the center of the tube (Fig. 4.24). According to the simulation, the discharge filament was about 2-mm in diameter, which was consistent with our experimental results. At the steady state, the center of the tube had a high electron density of 2 x 0^{17} cm^{-3} (Figure 4.25).

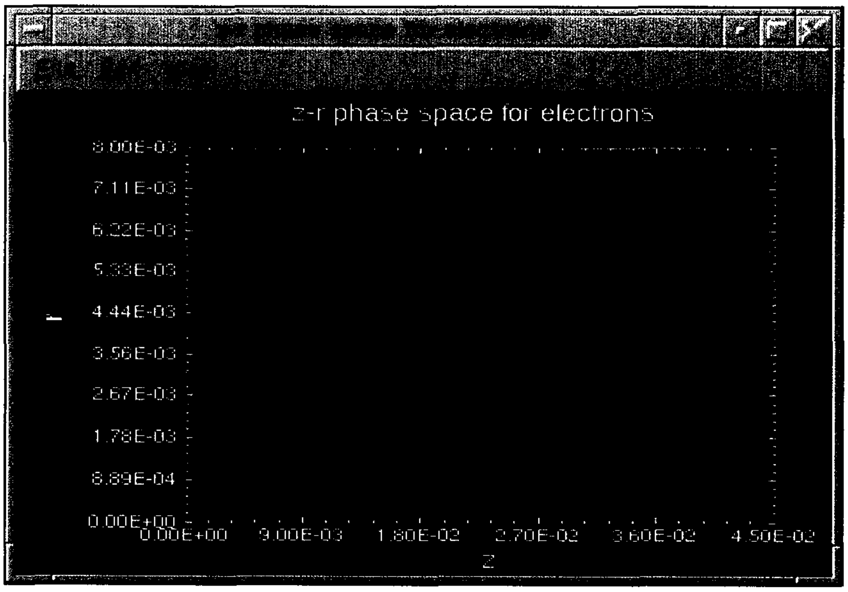

FIG. 4.21 The initial electron distribution in the discharge cell.

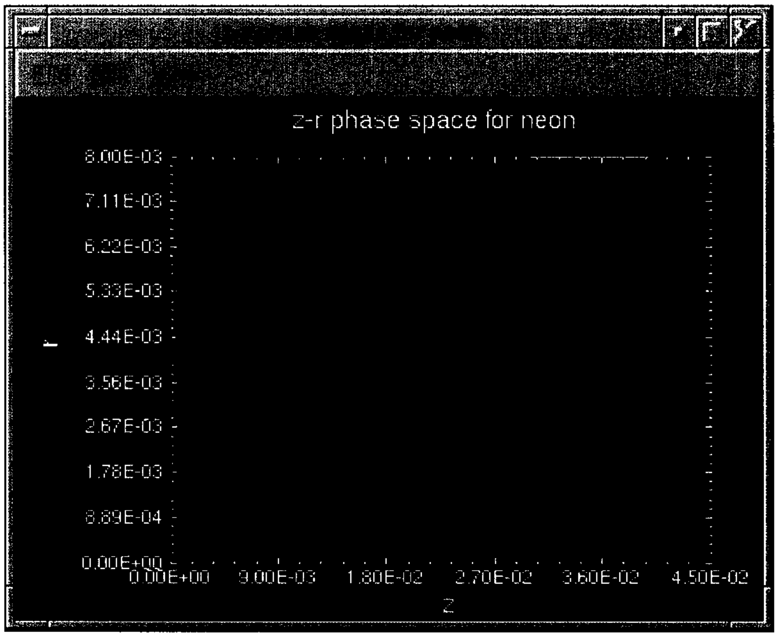

FIG. 4.22 The initial neon ion distribution in the discharge cell.

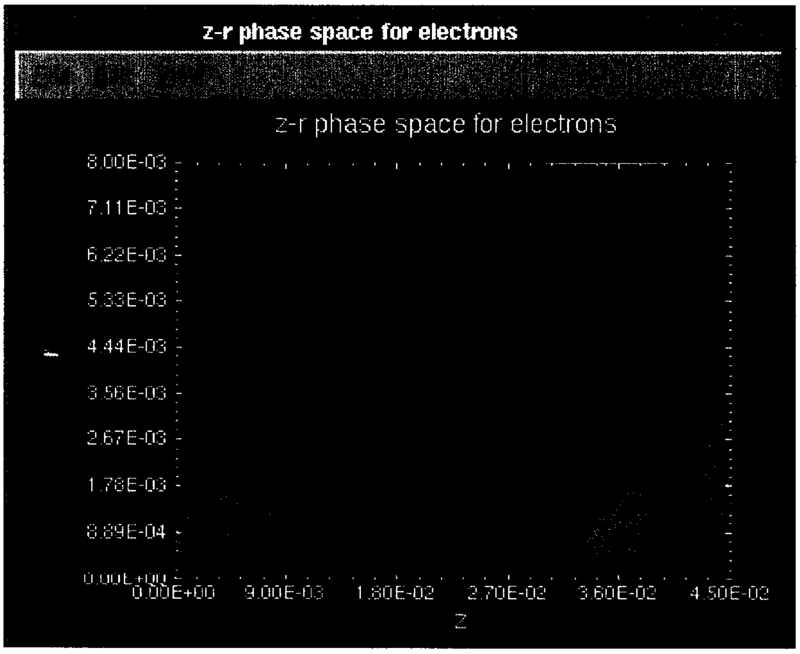

FIG. 4.23 The electron distribution in a stable state.

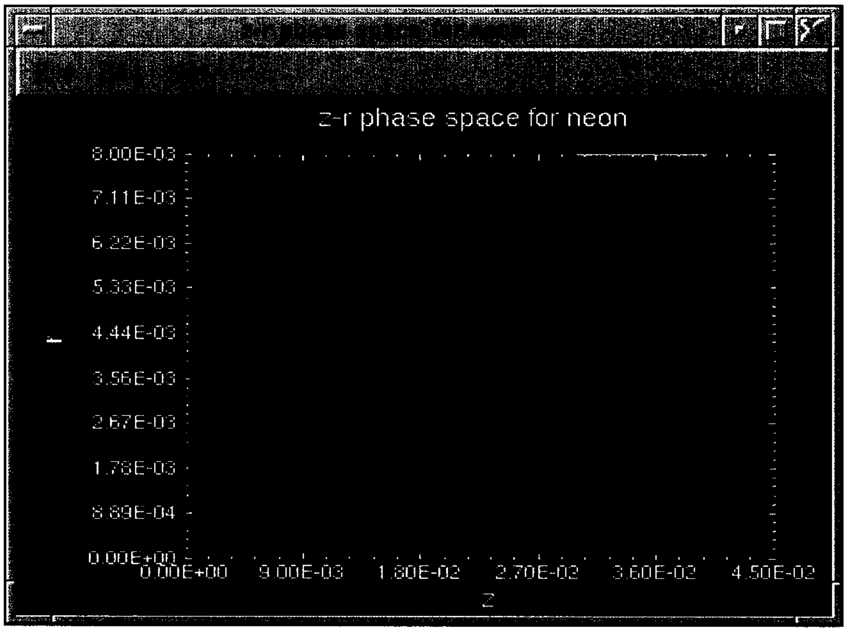

FIG. 4.24 The neon ion density distribution in a stable state.

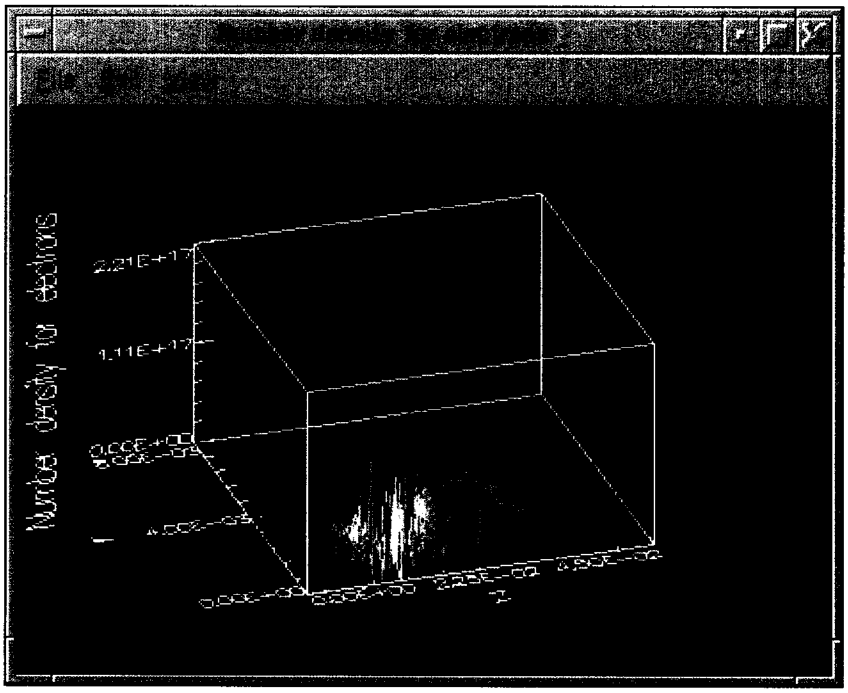

FIG. 4.25 The number density of electron in 3-D model.

Figures 4.26 and 4.27 show the variation in electric field along the radial (r) and axial (z) directions. The electric field in the electrode region was higher than other regions, and had peaks at the edge of the electrodes, which had an intensity of 6 x 10^5 V/m. The high electric field in the electrode region pushed the electrons and ions to the center of the tube. The average temperature of the electrons was determined to be 8 eV in the steady state (FIG. 4.28). This energy was adequate for the excitation of rare gas atoms and the formation of the excimer.

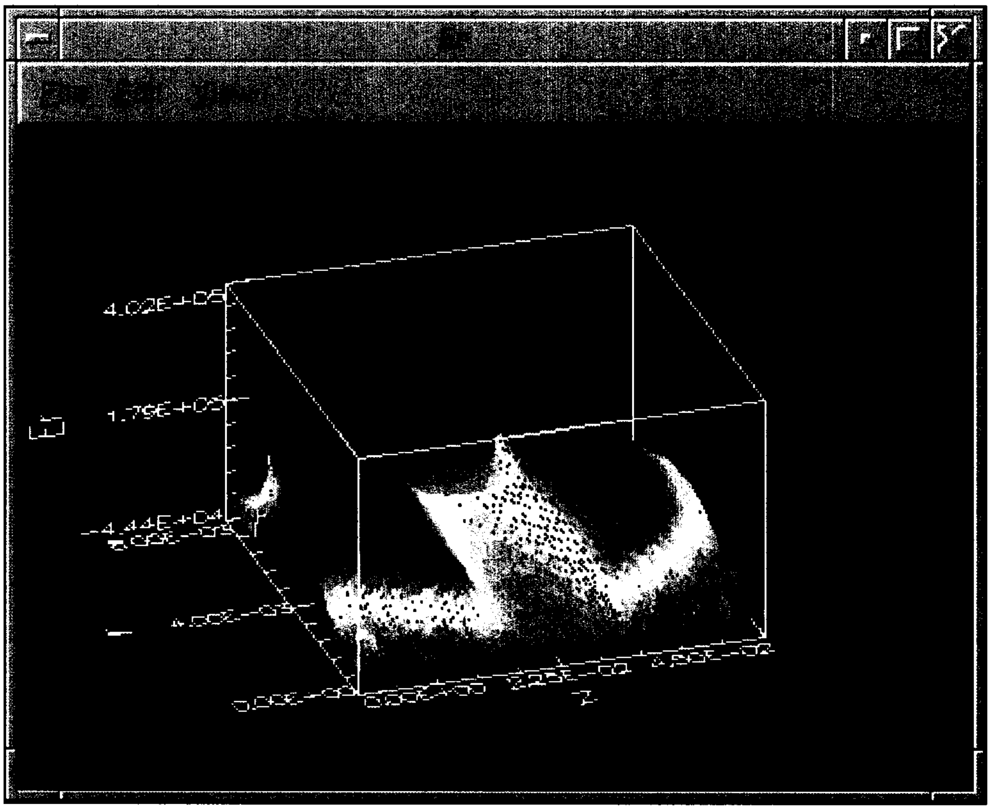

FIG. 4.26 Variation in electrical field along the radial (r) direction in the 3-D model.

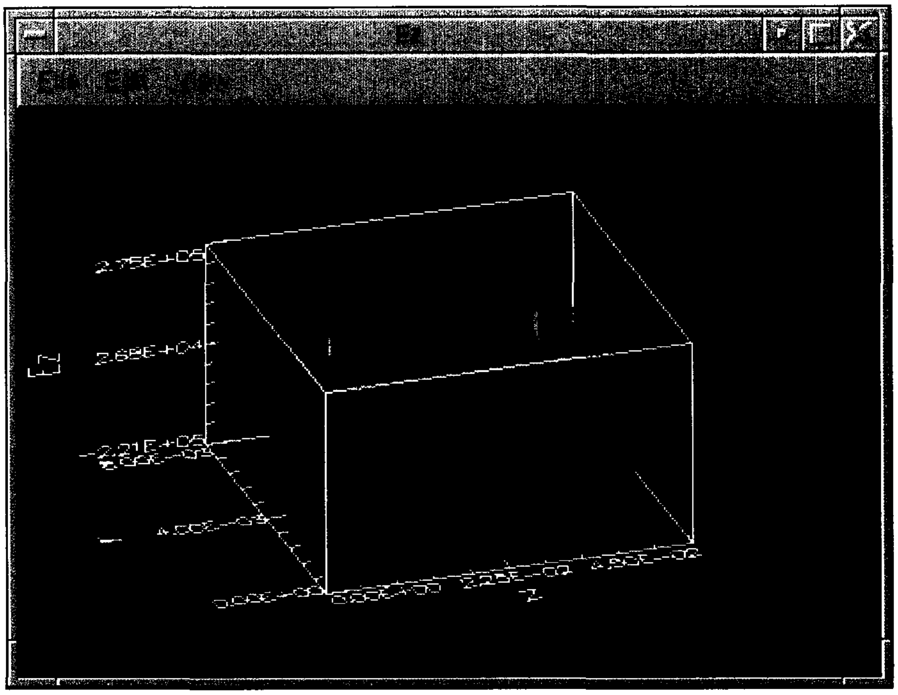

FIG. 4.27 Variation in electrical field along the axial (z) direction in the 3-D model.

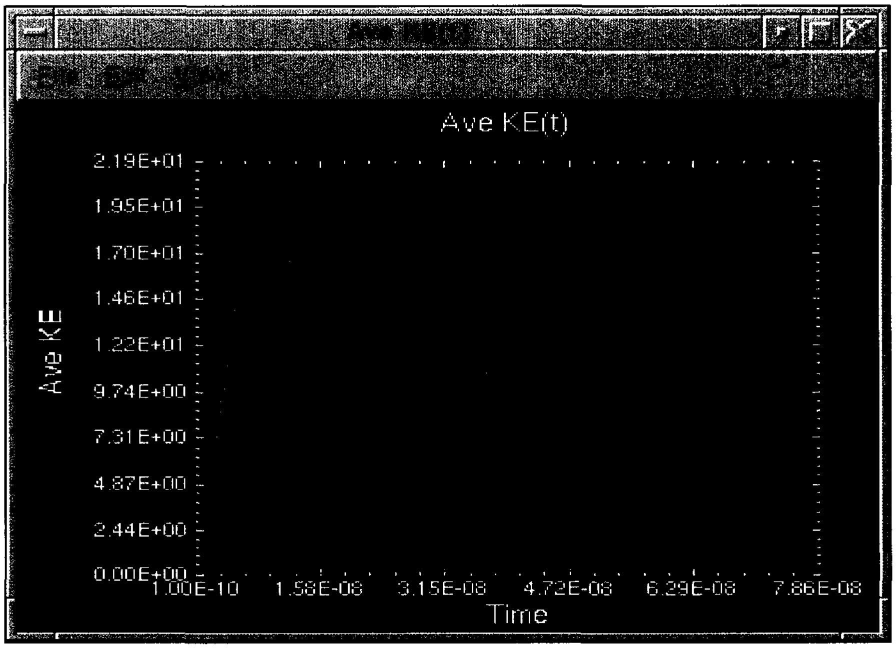

FIG. 4.28 Average electron energy (eV) variation over time (s).

4.4 Argon Discharge

We have discussed the generation of strong Lyman-α radiation in the DBD setup with a high-pressure neon and hydrogen mixture. From our experiment we also found that strong Lyman-α radiation could be generated in low-pressure discharges of neon, argon, and helium gases. In this section we discuss the spectral features of argon discharge in the presence of impurities such as hydrogen, nitrogen, and oxygen. The reason that we selected an argon discharge is because it holds the potential for the analysis of many atomic resonance transitions at VUV wavelengths. Most of the experiments that have investigated argon discharge were low-pressure discharge [14,76,102]. We investigated emission features of pure argon, argon hydrogen mixtures, and argon oxygen mixtures on both low-pressure and high-pressure regions.

5.4.1 Radiation in the Argon Discharge

The discharge was generated in low-pressure (less than 1 Torr) argon gas. We measured the spectrum of the VUV region with a monochromator. Fig. 4.29 shows the argon radiation lines at 104.8 nm and 106.6 nm, the Lyman-α lines at 121.6 nm, and the atomic oxygen line at 130 nm. The atomic lines, beside argon atomic, are emitted by background gas impurities such as oxygen, hydrogen, nitrogen, and carbon present in the discharge system. At low pressure, the plasma is comprised of a complex mixture of charged particles (electrons and ions) and neutrals (ground- and excited-state molecules and free radicals) and energy transfer processes between them.

Argon has the atomic resonance transitions (ArI) at 104.8 nm and 106.6 nm. The $^1P_1$ and $^3P_1$ levels from which these lines emit are intercalated with the metastable $^3P_2$ and $^3P_0$ states. The metastable levels rapidly equilibrate with the resonant levels and radiation trapping leads to an overpopulation of all four of these highly energetic states of ArI. The two argon metastables $^3P_2$ (11.55 eV) and $^3P_0$ (11.72 eV) play a very important role in the overall excitation mechanism. In the presence of trace amounts of H_2, we observed intense Lyman-α emission (FIG. 4.29). The metastables increased the ground-state H atom concentration by collisional dissociation of H_2 molecules through low-lying repulsive states based on the following reactions:

$$Ar^* + H_2 \rightarrow Ar + H + H, \qquad (4.4.1)$$

$$Ar^* + H_2 \rightarrow ArH^* + H. \qquad (4.4.2)$$

Then the Lyman-α radiation was enhanced by the following energy transfer mechanism:

$$Ar^* + H \rightarrow ArH^* \rightarrow Ar + H^*, \qquad (4.4.3)$$

$$H^* \rightarrow H + h\nu\ (121.6\ \text{nm}). \qquad (4.4.4)$$

At low pressure, the population of metastable states was enhanced and the above reactions dominated, so very strong Lyman-α emission was observed. With increasing pressure, the metastable population decreased due to the lower electron excitation rate, resulting in the intensity of the atomic lines decreasing. Fig. 4.30 shows variation of the Lyman-α radiation intensity at 121.6 nm across different pressures at an input RF power of 200 W. We obtained maximum Lyman-α radiation intensity at a pressure of approximately 600 mTorr. At high pressure (more than 10 Torr), the Lyman-α intensity is very weak.

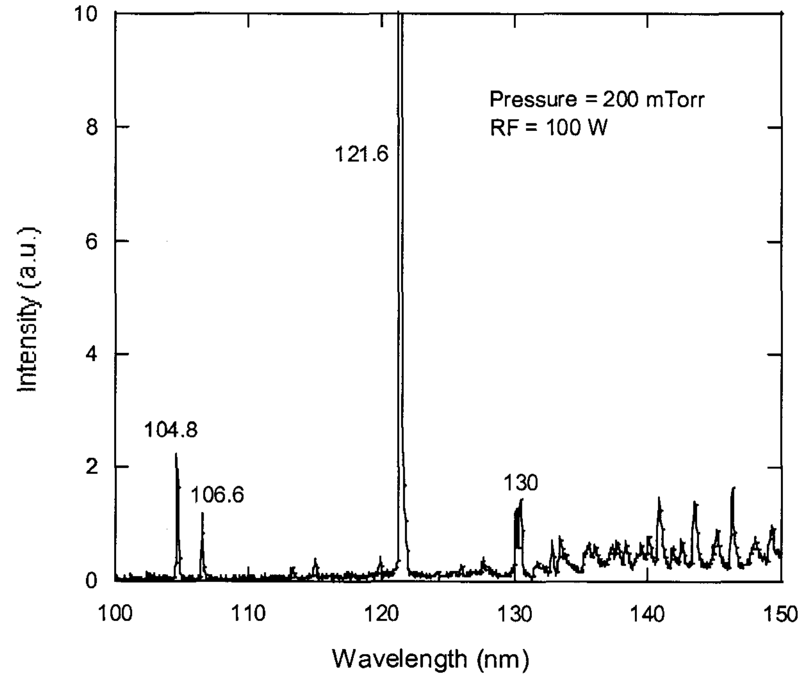

FIG. 4.29 Wavelength scan of VUV region extending from 100 nm to 150 nm for a low-pressure argon discharge.

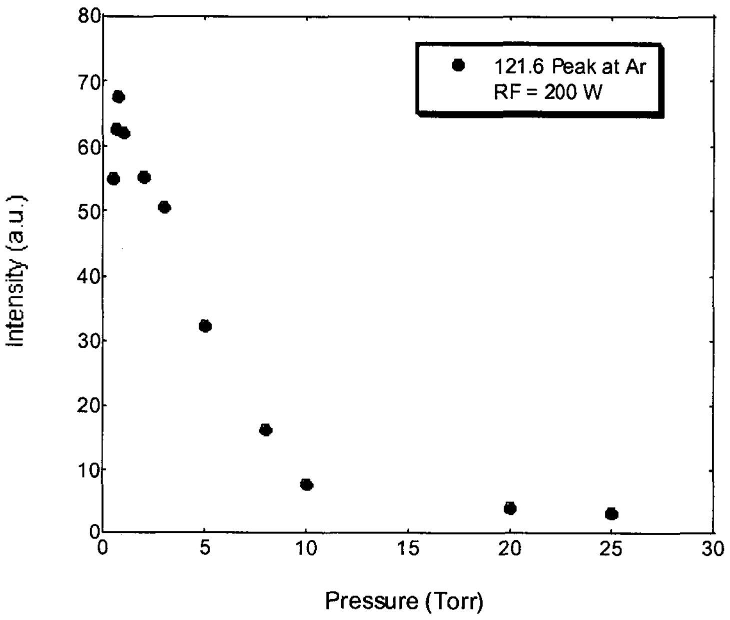

FIG. 4.30 Lyman-α radiation intensity in an argon discharge as a function of pressure.

Fig.4.31 shows the spectra of an argon discharge at different pressures with an RF input power of 100 W. Variation in other atomic lines such as oxygen, nitrogen, and carbon lines was observed. Among them, the hydrogen atomic line at 121.6 nm and the oxygen atomic line had dramatic variations with pressure. At low pressure, Lyman-α was dominate, but the carbon lines at 156 and 165 nm were strong while the oxygen lines at 130 nm were very weak. As the pressure increased, the VUV radiation decreased with Lyman-α dramatically reducing and the oxygen lines increasing. The emerging and increasing oxygen lines result from the following reactions:

$$Ar^* + O_2 \rightarrow Ar + O + O, \qquad (4.4.5)$$

$$Ar^* + O \rightarrow ArO^* \rightarrow Ar + O^*. \qquad (4.4.6)$$

Proceeding these reactions, the O* excited state decays by the radiative cascade emission,

$$O^* \rightarrow O + h\nu \text{ (130.4 nm)}. \qquad (4.4.6)$$

As the pressure continually increased, the argon excimer radiation peaking at 126 nm with a 14 nm broad linewidth (FWHM) was enhanced (FIG. 4.31d). We observed strong excimer radiation above atmospheric pressure (FIG 4.32). The discharge mechanism at high pressure was very different from the low-pressure discharge. At high pressure, the three-body reaction dominated and promoted excimer formation. The Ar_2^* excimers then resonantly transfer energy to molecular oxygen, exciting the oxygen atoms, which emit a strong atomic line at 130 nm [103, 104]. Other atomic lines such as NI (120, 149, 173 nm), and CI (156, 165,193 nm), were also observed.

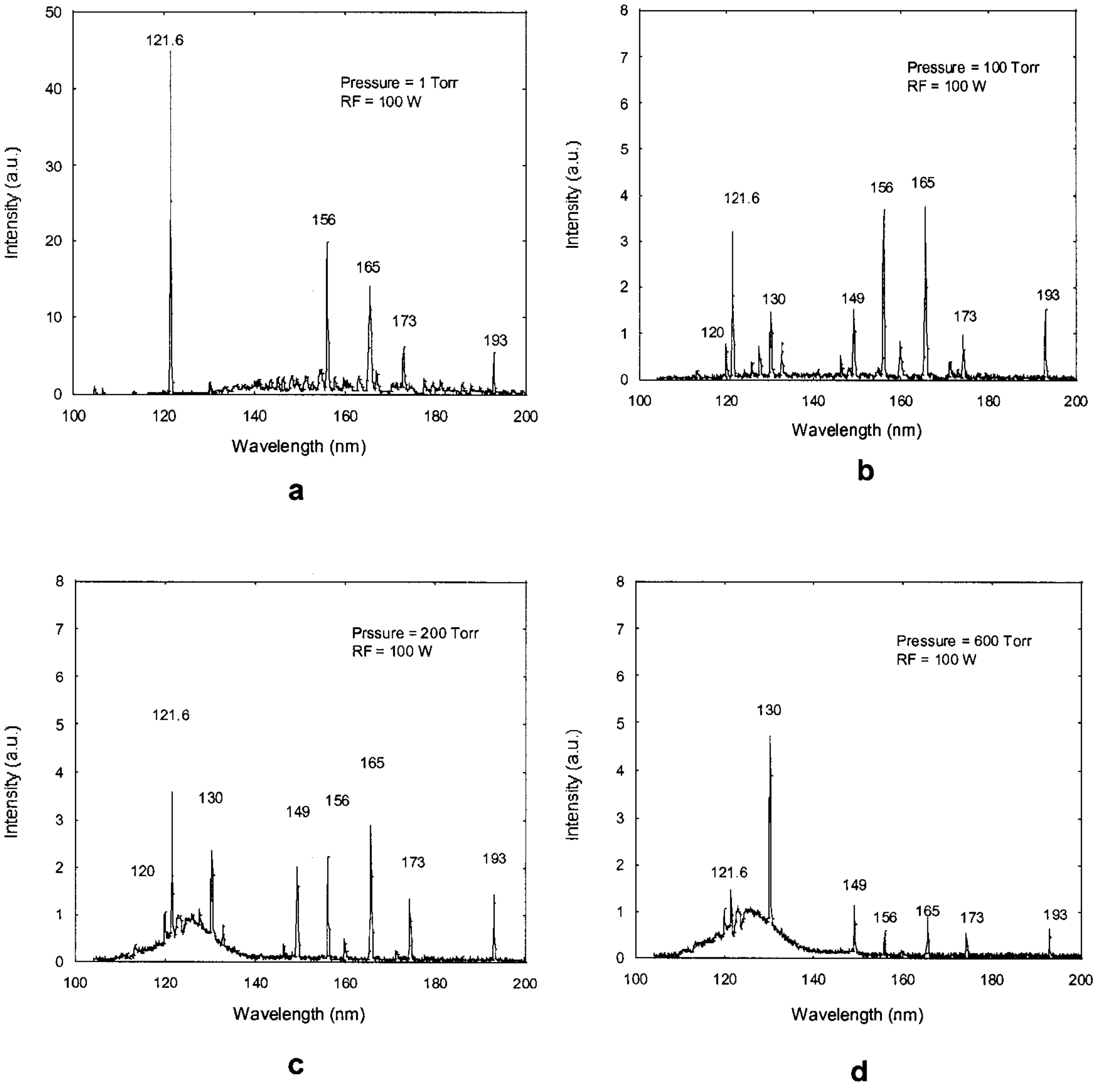

FIG. 4.31 The VUV spectra of an argon discharge at different pressures, a) pressure = 1 Torr, b) pressure = 100 Torr, c) pressure = 200 Torr, d) pressure = 600 Torr with an input rf power of 100 W. The Lyman-α line (121.6 nm), nitrogen atomic lines (120, 149, 173 nm), oxygen atomic line (130 nm), carbon atomic lines (156, 165, 193 nm), and the argon excimer line at 126 nm can be seen.

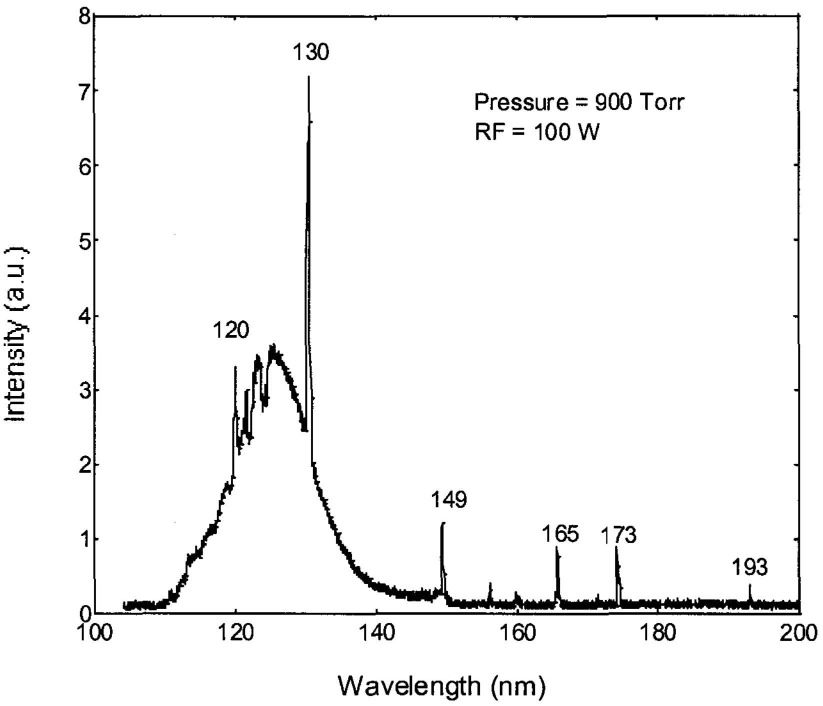

FIG. 4.32 VUV spectra of an argon discharge at high pressure (900 Torr) with an RF input power of 100 W.

5.4.2 Mixture of H_2 and O_2 with Argon

The spectra of argon-H_2 mixtures were measured. At low-pressure (600 mTorr), we observed the most intense Lyman-α emission at 0.5% H_2 in Ar (Fig. 4.33). Under these conditions, the other atomic lines were very weak. This means most of the energy of the metastable states of argon was transferred to hydrogen atoms by collisional dissociation which excited the hydrogen atoms. Again, when the pressure increased, the intensity of Lyman-α radiation decreased dramatically. Fig. 4.34 shows the spectra of an Ar-H_2 discharge at 400 Torr with an RF input power of 200 W. Only very weak lines of Lyman-α and NI at 149 nm were observed.

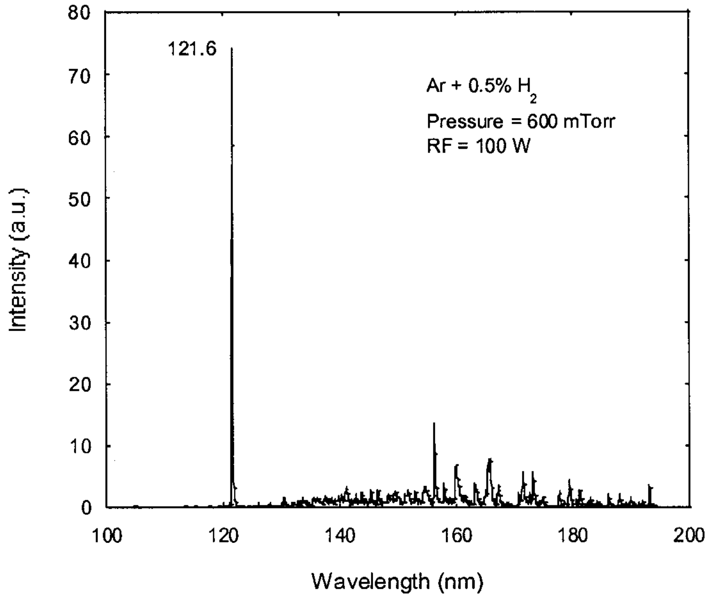

FIG. 4.33 VUV spectra of an argon and hydrogen mixture discharge at low pressure (600 mTorr) with an RF input power of 100 W.

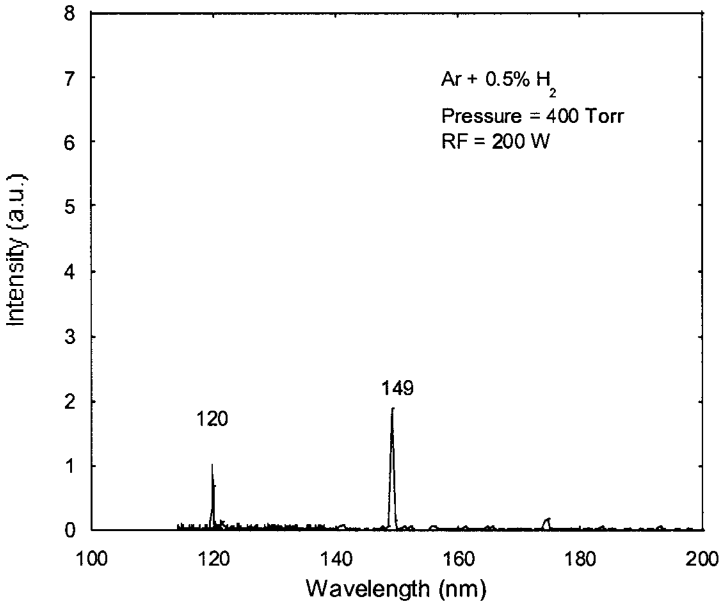

FIG. 4.34 VUV spectra of an argon and hydrogen mixture discharge at high pressure (400 Torr) with an RF input power of 200 W.

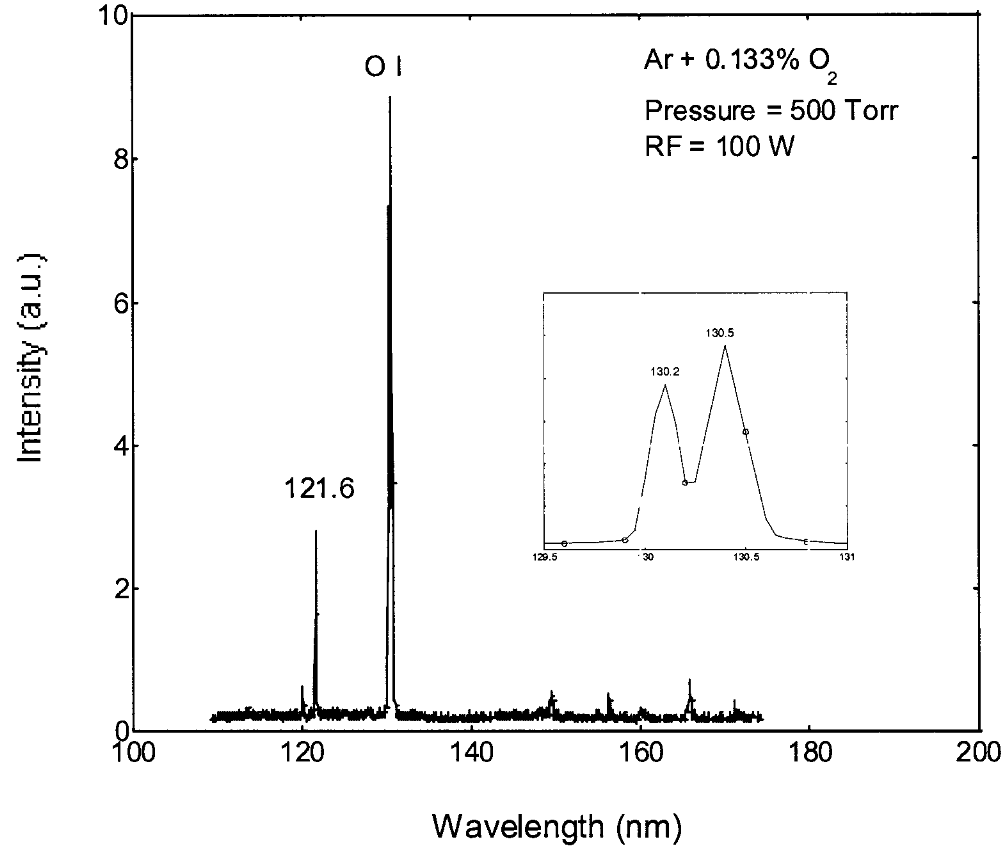

FIG. 4.35 Spectrum of Ar with a 0.133% oxygen mixture at a pressure of 500 Torr, and an RF input power of 100 W.

For an Ar-O2 mixture at low pressure, we did not observe a strong Lyman-α line nor strong oxygen lines at 130 nm. Strong oxygen atomic line peaking at 130.2 and 130.5 nm was obtained when a discharge was generated in high-pressure argon with a mixture of oxygen below 1%. Fig. 4.35 shows the spectra of argon and 0.133 % oxygen at a pressure of 500 Torr with an RF input power of 100 W. The second peak at 130.5 nm was a little higher than the 130.2 nm peak and slightly asymmetric, indicating the presence of a third line at 130.6 nm. This spectrum seems to correspond to the atomic oxygen transition $2p^4\ ^3P \leftarrow 2p^3(^4S^0)3s\ ^3S^0$ triplet. The excitation of the oxygen triplet was due to resonant energy transfer from Ar_2^* excimers, causing the argon excimer spectrum to almost disappear. Energy transfer was probably due to the following reactions:

$$Ar_2^* + O_2 \rightarrow 2Ar + O + O$$

$$Ar_2^* + O \rightarrow 2Ar + O^*$$

The intensity of the oxygen line was measured and a high radiation power was obtained. Because the triplet occurred at 130 nm, the linewidth (FWHM) was 0.5 nm.

Some radiation lines from 100 nm to 130 nm were observed. The goal of the argon discharge experiment was to find an ideal radiation source with a wavelength from 100 nm to 130 nm for advanced lithography. There were two argon atomic lines at 104.8 nm and 106.6 nm, but they can not be a good source for lithography because, first, the radiation is not intense enough for lithography and, second, these two lines are too close to be suitable for imaging. The nitrogen atom line at 120 nm is also not intense enough for lithography. Argon excimer peaking at 126 nm provides strong radiation, but the linewidth is too broad to provide at ideal source for lithography. Oxygen atomic lines at 130 nm also provide strong radiation, but this triplet would have a linewidth of about 0.5 nm. So only the Lyman-α line at 121.6 nm has potential for an optimum radiation source for lithography applications.

CHAPTER V

APPLICATIONS OF THE VUV SOURCE

The spectrum of VUV radiation spans a broad and important range of photon energies from 6 to 12 eV which correspond to the energies of many atomic and molecular states. Accordingly, VUV radiation has potential important applications in spectroscopy and photochemistry.

VUV radiation provides a method for the study of the excited states of many atomic and molecular species that possess energies of several eV using single-photon spectroscopy. If the VUV sources has sufficiently narrow bandwidth to allow single-photon excitation of single rotational levels, the absorption spectra may be studied by VUV induced fluorescence techniques or perturbations in the molecular structure may be investigated by measuring the radiative lifetime as a function of rotational quantum number. The detection of atomic or molecular species is another related application of VUV radiation. More specifically, it is possible to probe the nascent distribution over energy levels of product species in photochemical reactions. Another area of application of VUV radiation is in photochemistry because a large number of the molecular states accessible via absorption of a VUV photon are dissociative. Related applications are excited state chemistry in which photodissociation is employed to selectively produce excited state fragments, which would then initiate chemical reactions. There are also applications of VUV radiation in lithography. At present the attainable feature size is limited by diffraction and consequently shorter wavelengths are necessary to achieve smaller components in semiconductor devices. Finally, there are possible applications in

VUV-induced etching and deposition techniques, material surface processing, and remediation of pollutants and waste streams.

The strong, and often continuous, absorption in the VUV by many atoms and molecules makes VUV radiation very useful. However, absorption by impurities is a problem for the operation of VUV. The absorption bands of molecular oxygen are very strong throughout the VUV [105,106]. Fig. 5.1 shows the absorption spectrum of molecular oxygen in the VUV region. It is apparent that absorption coefficients in the VUV region are large. Consequently, all experimental apparatus must be evacuated or flushed with a non-absorption gas such as helium or argon. Also, impurities inside the VUV sources further reduce the intensity of the VUV radiation. In our experiment, the VUV lamp was operated under high vacuum.

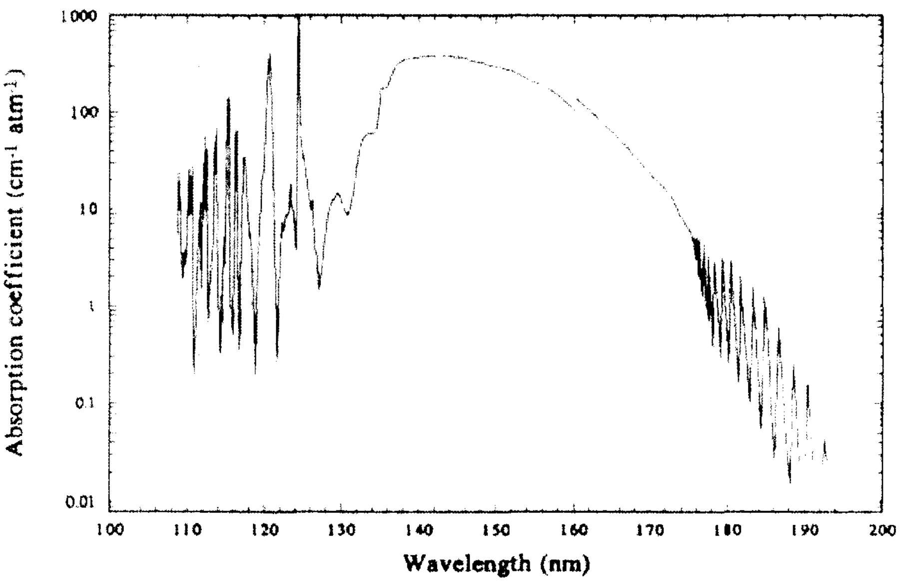

Fig. 5.1 Absorption coefficient of molecular oxygen in the VUV region (ref. 105, 106).

The 121.6 nm lamps were used for two kinds of applications. One was high-resolution lithography conducted in the MIT Lincoln Lab and the other was direct metal-pattern writing by VUV photodissociation [107].

5.1 High-resolution Lithography

We have sent our lamp to the MIT Lincoln Lab for lithography experiments and studied the feasibility of the lamp for advanced lithography.

5.1.1 Optical Materials

One of the biggest obstacles to implementing 121.6 nm lithography is optics for high-resolution printing. The availability of high-quality lens material is a critical requirement for an optical projection system. These materials must satisfy stringent requirements, such as an internal transmission of more than 95% per cm to avoid thermally induced aberrations in elements of the projection system and the defect-free processes for polishing and figuring refractive elements.

Optical materials in 193 and 157 nm lithography are not suitable for 121.6 nm lithography because these materials, fused silica and calcium fluoride, are not transparent at 121.6 nm. Fig. 5.2 shows the external transmission of materials commonly used for optical components in VUV [108]. Obviously, optical materials that transmit 121.6 nm are MgF_2 and LiF with fundamental cut-off wavelengths at 105 nm and 113 nm, respectively. LiF is more hygroscopic and mechanically softer than MgF_2. If it is carefully stored and treated, its transmission loss is negligible and can be usable for 121.6 nm lithography. The cut-off wavelength of LiF is 105 nm, and therefore its intrinsic transmission is usable at 121.6 nm. The theoretical extrinsic transmission of an LiF window, after correcting for Fresnel losses, is 89.5%. However, in practice, the transmission of commercial LiF is only 40% for a 2-mm-thick window. Because of the oxide- and hydroxide-related impurities, high transmission LiF windows are difficult to obtain. MgF_2 is not hygroscopic and is harder than LiF. Although its birefringence at 121.6 nm is $\sim 4x10^{-3}$, which is too large for fabrication of high quality lenses, it is still the preferred material for work at 121.6 nm.

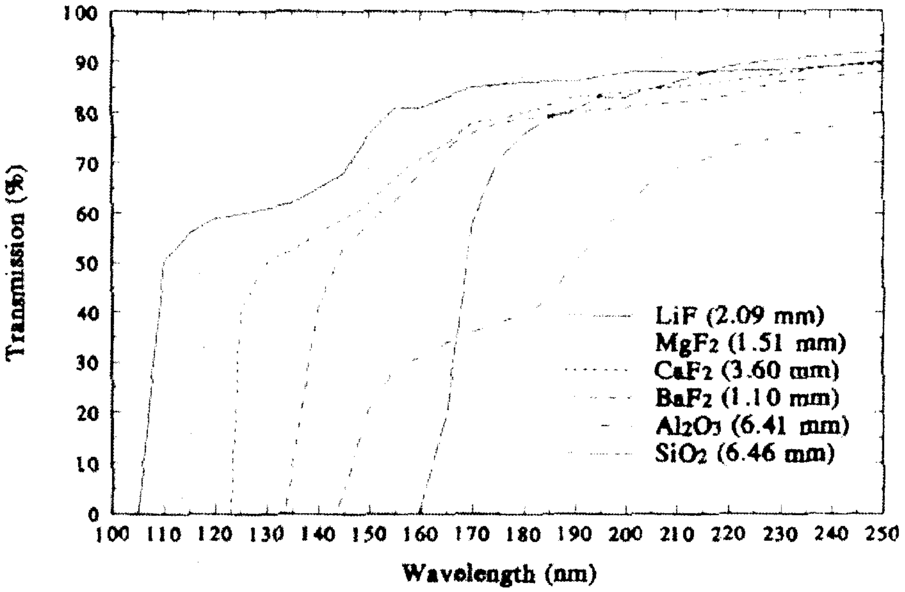

Fig. 5.2 The external transmission of VUV window materials (ref.114).

5.1.2 Experimental Setup

Because of the difficulties involving high-transmission LiF and MgF_2 lenses, no 121.6 nm optical projection system has been constructed. Instead, Lincoln Lab has demonstrated high-resolution printing by employing near-field photolithography with a phase shifting mask. Fig. 5.3 shows the setup for near-field contact printing, which includes a 121.6 nm radiation source, a MgF_2 phase shift mask that was patterned and etched to form steps whose height corresponded to a 180° phase shift, and a silicon wafer coated with 20 nm thick of photoresist.

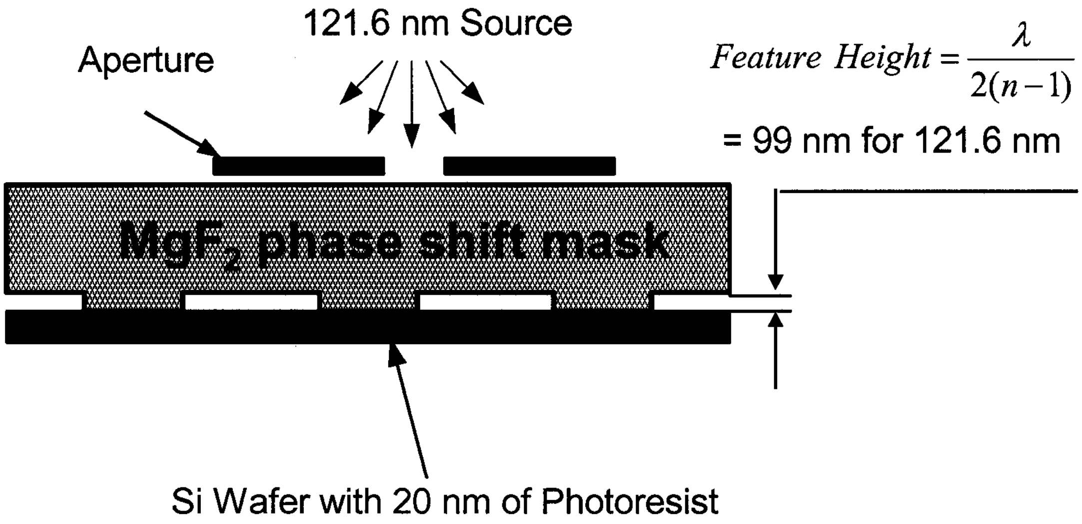

Fig. 5.3 Schematic of near-field contact mode photolithography with shifting mask (Provided by the MIT Lincoln Lab).

The 121.6 nm source was calibrated before being used in near-field lithography. The discharge was ignited with an rf power supply and tuned with the matching network. Initially, the plasma was conditioned for about half an hour. During that period, the discharge was not stable due to imperfect rf power matching and heating. After half an hour, the discharge became stable providing a constant optical output as shown in Fig. 5.4. The intensity of lamp output was measured by a photo diode detector.

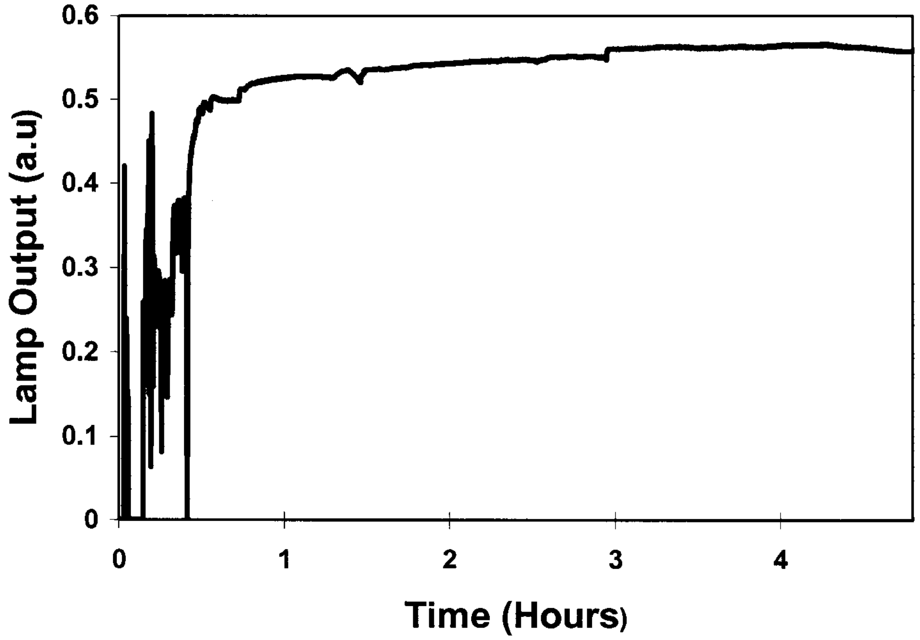

Fig. 5.4 The 121.6 nm radiation output versus time (Provided by the MIT Lincoln Lab).

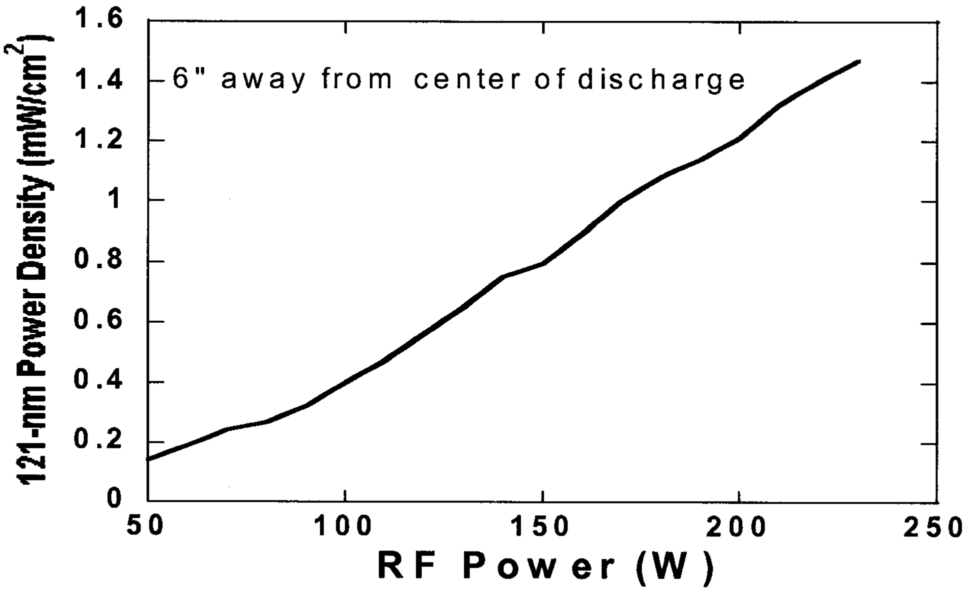

Fig. 5.5 The 121.6 nm radiation power density versus RF input power (Provided by the MIT Lincoln Lab).

The power density of 121.6 nm was measured with a photodetector. Fig. 5.5 shows that the power density linearly increases with RF power. The detector was 6 inches away from the center of the plasma. A power density of more than 1 mw/cm^2 was obtained, which meets the requirements of lithography.

5.1.3 Near-field Phase Shift Mask

The mask in the experiment was based on the technique of near-field phase shifting [109]. Consider light passing through a transparent mask (Fig. 5.6). The phase, φ (x), of the light with wavelength λ that emerges from the mask is related to the relief of the surface, u(x), and to the difference between its index of refraction and that of the surroundings, Δn, by Eq. (5.1.1).

$$\varphi(x) = \frac{2\pi}{\lambda}\Delta n u(x) \tag{5.1.1}$$

If the finite thickness of the relief on the surface of the mask is neglected, the electric field just after emerging from the mask (at position z=0$^+$) can be related to the electric field just before emerging from the mask (at position z=0$^-$) by equation (5.1.2),

$$\begin{aligned} E(x, z=0^+) &= E(x, z=0^-)\exp[i\varphi(x)] \\ &\equiv E(x, z=0^-)\tau(x). \end{aligned} \tag{5.1.2}$$

Equation (5.1.2) defines the transmission function of the phase mask, $\tau(x)$. When the relief of the surface is binary and has magnitude u$_1$ and periodicity of d, then $\tau(x)$ can be described as equation (5.1.3).

$$\tau(x) = \begin{cases} \exp\left(\frac{2\pi\, i}{\lambda} u_1 \Delta n\right) & md < x < \left(m + \frac{1}{2}\right)d, \quad m = 0, \pm1, \pm2, \pm3.... \\ 1 & otherwise. \end{cases} \tag{5.1.3}$$

When $u_1 = \lambda/(2\Delta n)$, the phase shift equals π, and the electric field undergoes abrupt changes in sign at the edges where the phase shift occurs. According to the wavelength, the surface relief of the mask, and the difference between the index of refraction of the air and the mask ($\Delta n = n - 1$), the phase of the light passing through the mask is modulated. Modulations of the phase create modulations in intensity in the near field. Theoretically, near-field phase-shifting lithography has the ability to print features with dimensions approximately one third of the wavelength.

In the experiment, a transparent MgF_2 substrate was patterned and etched to form periodic steps with a height corresponding to a 180° phase shift. According to equation (5.1.3), the height u_1 was given by $\lambda/[2(n-1)]$, which was 99 nm for the 121.6 nm wavelength and for a refractive index n = 1.61 of MgF_2. The periodic steps in the MgF_2 substrate were formed by patterning gratings in photoresist using i-line contact lithography. First, a master fused silica mask, which had patterns with chromium lines, was duplicated into photoresist on a 0.2-mm-thick fused-silica flex mask. The flex mask was then contacted to the MgF_2 substrate, which had been coated with 0.5 μm i-line resist. After exposure and development, the MgF_2 substrate was etched by argon ion milling. By accurately controlling the etching time, the depth of the etched lines was obtained. After striping the remaining photoresist, the etched pattern was formed on the MgF_2 substrate.

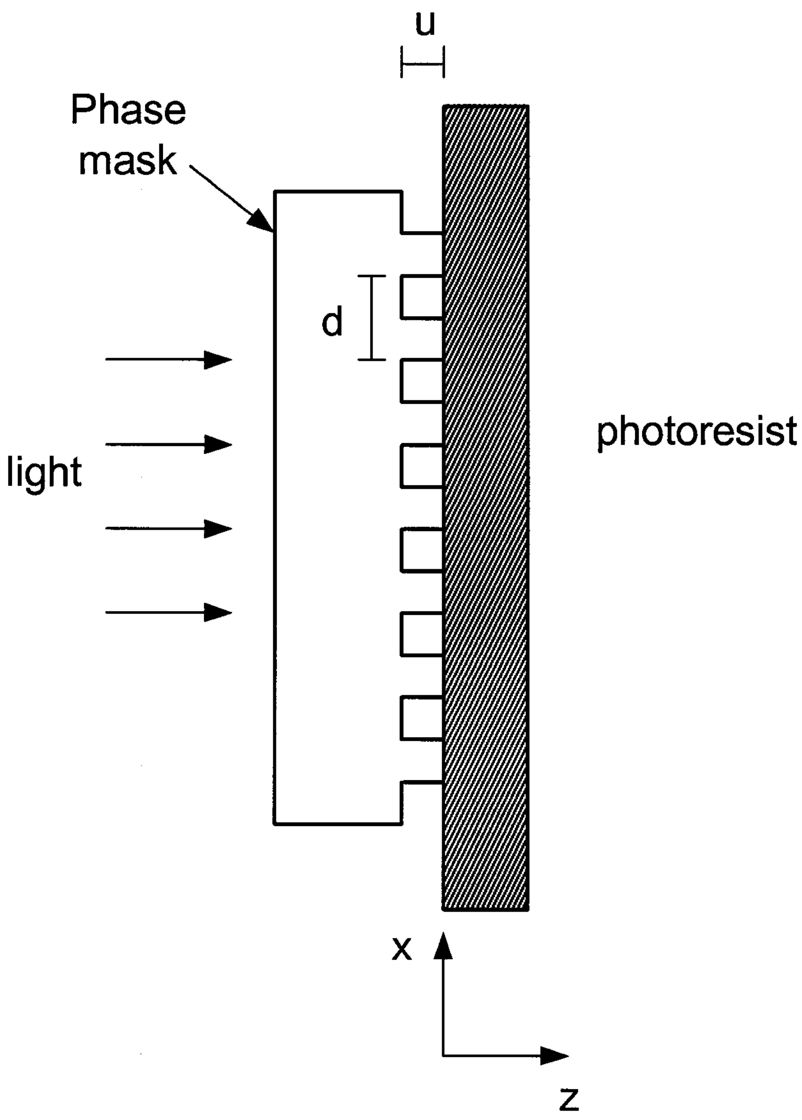

Fig. 5.6 Geometry of the phase mask, the photoresist, the exposure light, and the qualitative definition of the near field.

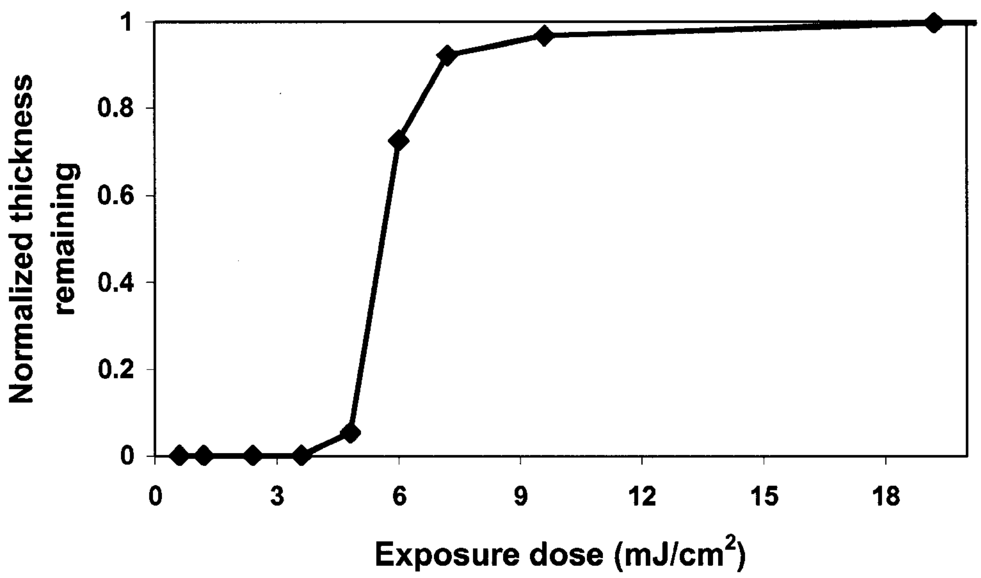

Fig. 5.7 Normalized thickness remaining versus incident 121.6 nm dose (Provided by the MIT Lincoln Lab).

A negative photoresist (Hydrogen silsesquioxane from Dow Corning) was spin-coated on the silicon wafer. The thickness of the resist was about 20 nm. Intimate contact between the wafer and the MgF_2 mask was essential for obtaining high contrast in the resist. The resist coated on the Si wafer was exposed to 121.6 nm light through a 6 mm aperture. Exposure was followed by a post exposure bake and 60 second development in a commercial LDD24W aqueous base developer. The normalized thickness remaining (NTR) was plotted versus 121.6 nm exposure dose in Fig. 5.7. Based on thickness measurements with an ellipsometer, the resist exhibited very high contrast.

The patterns were examined using a scanning electron microscope (SEM). From the SEM graphic, relatively small structures over a fairly large area were obtained. Figure 5.8 shows many patterns in a large area. Figure 5.9 shows a single pattern with a line width of 63 nm.

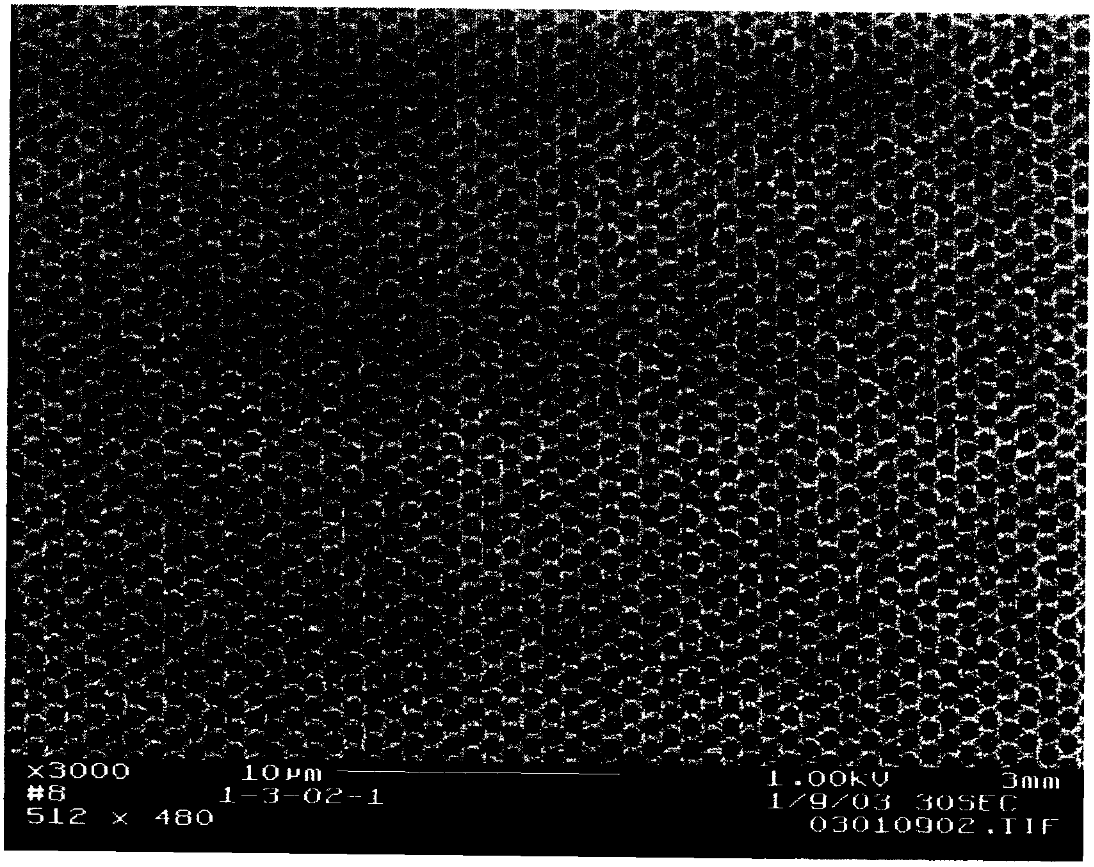

Fig. 5.8 The SEM graphic of a large scale pattern.

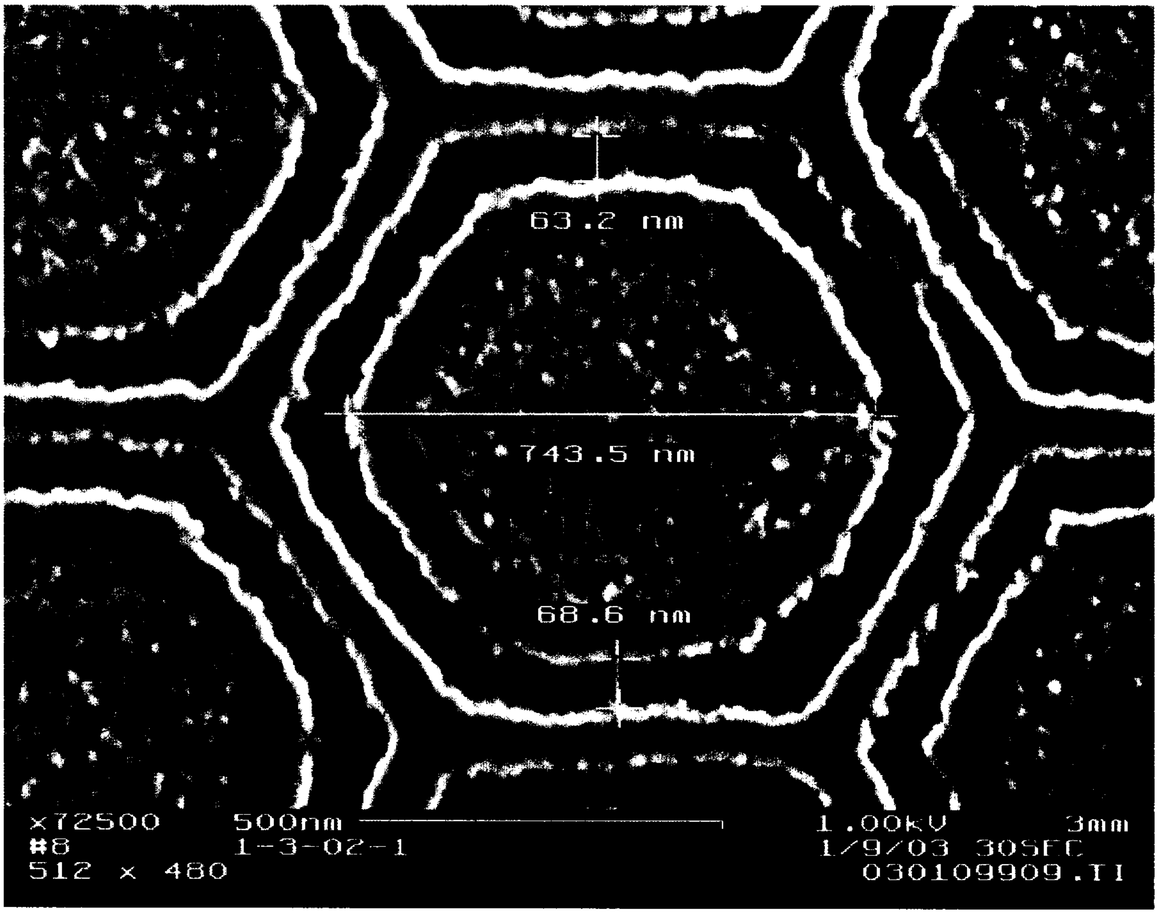

Fig. 5.9 The SEM graphic of a single pattern.

This work evaluated the potential of extending optical lithography to another wavelength in the VUV, the 121.6 nm Lyman-α emission. It has proven the feasibility of lithography at this wavelength that would enable extension of many of the optical technologies developed at 193 and 157 nm. From the source operation, it has been proven that our 121.6 nm DBD-based lamp is a stable source for 121.6 nm lithography and other advanced imaging work.

5.2 Direct Pattern Writing with Photodissociation

In the past, metalorganic materials for growing thin films of metals, dielectrics, and semiconductors have generally been gases, as used in laser-induced chemical vapor deposition (LCVD). Metalorganic gases, such as $Al_2(CH_3)_6$, $Ge(CH_3)_4$, and $Cr(CO)_6$, have been decomposed into metal films using lasers and VUV [110,111,112,113,114]. Unfortunately, depositing metals from gaseous precursors requires a complex and expensive vacuum system. Recently, metal deposition by large-area VUV induced decomposition of metalorganic compounds have appeared [107,115,116,117]. Metalorganic decomposition is a liquid-based method of depositing thin films, and does not require a vacuum. A metalorganic precursor, dissolved in appropriate solvent, is dispensed onto a substrate. After the solvent is evaporated, a VUV is used to decompose the metalorganic film, converting the metalorganic precursors to their constituent metal elements. A variety of thin films (Au, Cu, Pd, etc) have been deposited onto various substrates using different types of VUV radiation sources. The production of thin films by VUV-induced metalorganic decomposition offers several advantages over other thin film deposition methods. The process occurs at ambient temperature and pressure without gas transport and, therefore, needs no complicated vacuum equipment. Precursor materials can also be synthesized to incorporate a wide variety of metals. Since the metal ion and the organic radicals in the metalorganic materials are held together by weak bonds, the compounds decompose at relatively low temperatures. As a result, temperature-sensitive materials can also be coated.

Large-area VUV sources with high photon fluxes provide a relatively low cost method for industrial large-area processing. In our experiments, we have demonstrated that palladium, copper, and gold thin film deposition from their corresponding organic compounds using the DBD VUV source, which radiates a high intensity Lyman-α line at 121.6 nm. The high energy (10.2 eV) of Lyman-α photons is sufficient to break the bond between the metal ion and the organic radical in most metalorganic materials. Very uniform thin palladium film and direct pattern writing have been achieved in our experiment. Palladium thin films may act as catalysts for subsequent electroless metal deposition. This method can be used for deposition and patterning of various types of metallic, semiconducting, and nonconducting films for various applications.

5.2.1 Experimental Procedure

Palladium acetate ($Pd(OCOCH_3)_2$, Pdac) was dissolved in chloroform solution, and Pdac films of 100 ~ 1000 nm thickness were prepared by spin-on coating on glass, quartz, and silicon substrates. The resulting palladium acetate thin films were then directly irradiated with the high intensity Lyman-α line (121.6 nm) from the cylindrical DBD based VUV lamp source operating in a Ne and H_2 mixture with varied operation pressures from 1 Torr to 500 Torr. Fig. 5.10 shows the experimental setup. The discharge chamber had two quartz windows installed on the front and back sides and aligned with the discharge tube so that a laser beam could pass through the center of tube. The glass substrate was a round plate with thickness of 100 μm and coated with palladium acetate at a spin-speed of 1500 rpm. The precoated substrate then was located in the same chamber as the discharge tube, allowing the film to be directly exposed to the Lyman-α radiation with a power density of about 10 mW/cm^2. A photon detector and an Nd:YAG laser of wavelength 622 nm were used to measure the film's transmission. The changing of transmission was read from a power meter. The progress of palladium deposition could be determined by measuring the change in the transmission at different pressures and exposure times. The palladium acetate film thickness was measured using a Tencor Alpha step 200 profilometer. After exposure, the resulting palladium film thickness was measured with AFM (Digital Instruments Dimension 310). The transmission and reflection of palladium acetate films and palladium films were measured from UV to NIR by using a Perkin-Elmer Lambda 9 spectrophotometer.

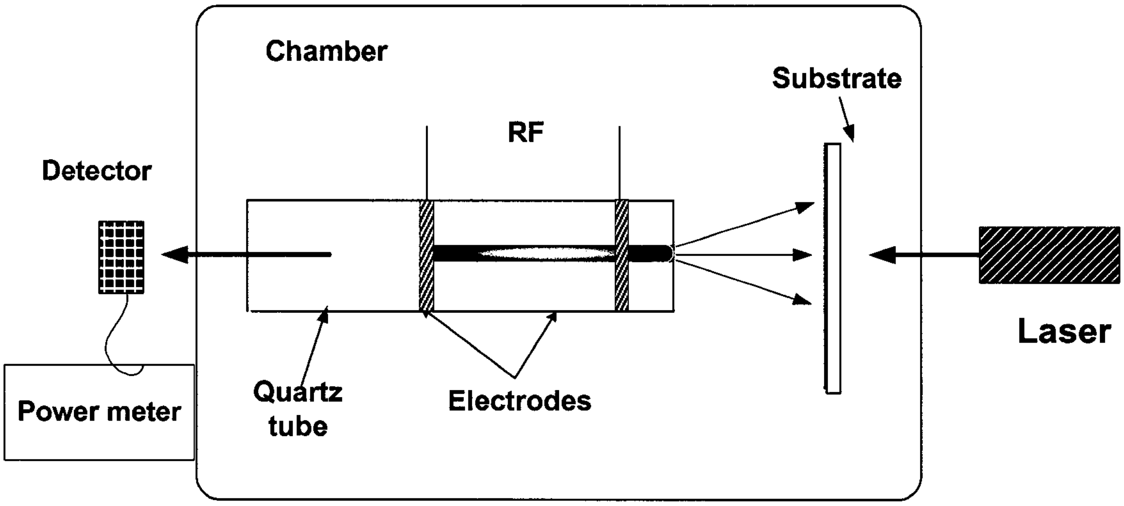

Fig. 5.10 Experimental setup for VUV photodissociation.

5.2.2 Palladium Thin Film and Its Characterization

Palladium Acetate Decomposition

The absorption of photons ($h\nu > 3.0$ eV) in palladium acetate initiates a photoreaction that leads to decomposition into palladium and volatile products of organic species as follows:

$$Pd(OCOCH_3)_2 \rightarrow$$

$$Pd + COCH_3^+ + CCH_3^+ + CH_3^+ + CO_2 + H_2O \qquad (5.2.1)$$

Ref.118 described the decomposition mechanisms of palladium acetate with VUV radiation. In that experiment, all the products have been observed with mass spectrometry (MS). From the evolution of the FTIR spectra of the palladium acetate films after exposure to VUV radiation, it showed that products such as $^+COCH_3$, $^+CH_3$, CO_2, and H_2O were decomposed from palladium acetate and the lamp-induced decomposition appeared to be mainly photochemical.

Pd Formation

By measuring the transmission of 622 nm laser light through Pd acetate films, the formation of the Pd layer versus time was examined. The transmission of the films decreased very quickly at the beginning (60 seconds). After that, a flat transmission curve was observed (Fig. 6.11). This indicated that palladium film had been completely decomposed and pure Pd film had formed. Comparing with other VUV sources, the time to totally obtain the palladium film was shorter with our 121.6 nm radiation lamp.

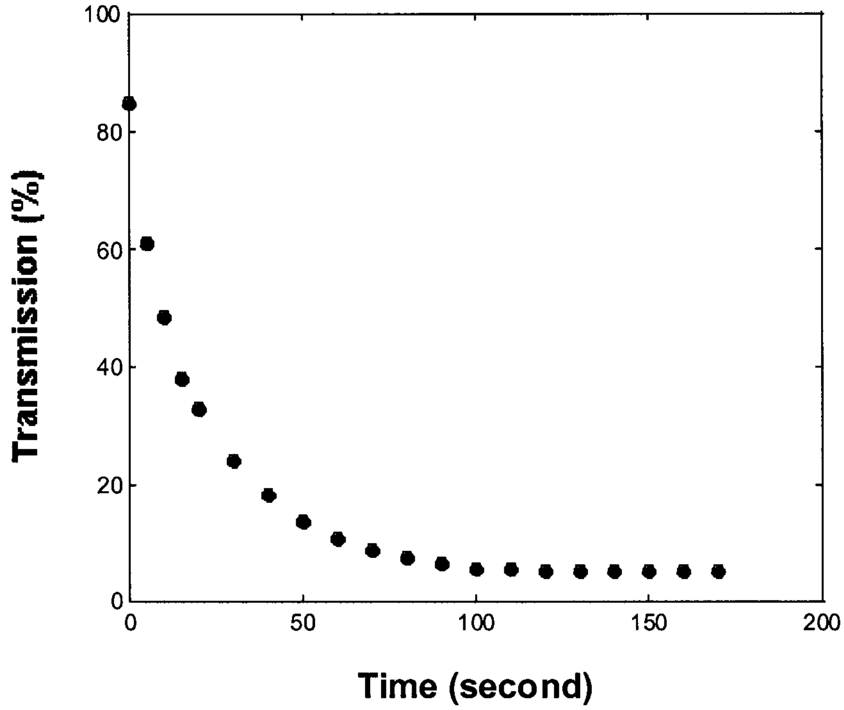

Fig. 5.11 Evolution of transmission of palladium and palladium acetate film as a function of exposure time at a pressure of 3 torr.

The decomposition rate of palladium acetate was dependent upon the pressure. The change of transmission in the palladium acetate and palladium films under different pressures is shown in Fig. 5.12. At a pressure of 3 Torr, the complete decomposition of palladium acetate was achieved in 1 minute. At higher pressures, the transmission change was dramatically less than that at lower pressures. Clearly, the decomposition rate of palladium acetate at higher pressures was much less than at lower pressures. This result was in agreement with other experiments in ref.119. In our system, the discharge gas was ventilated, so the volatile decomposition products, which would attenuate the radiation of Lyman-α, could be removed from the chamber.

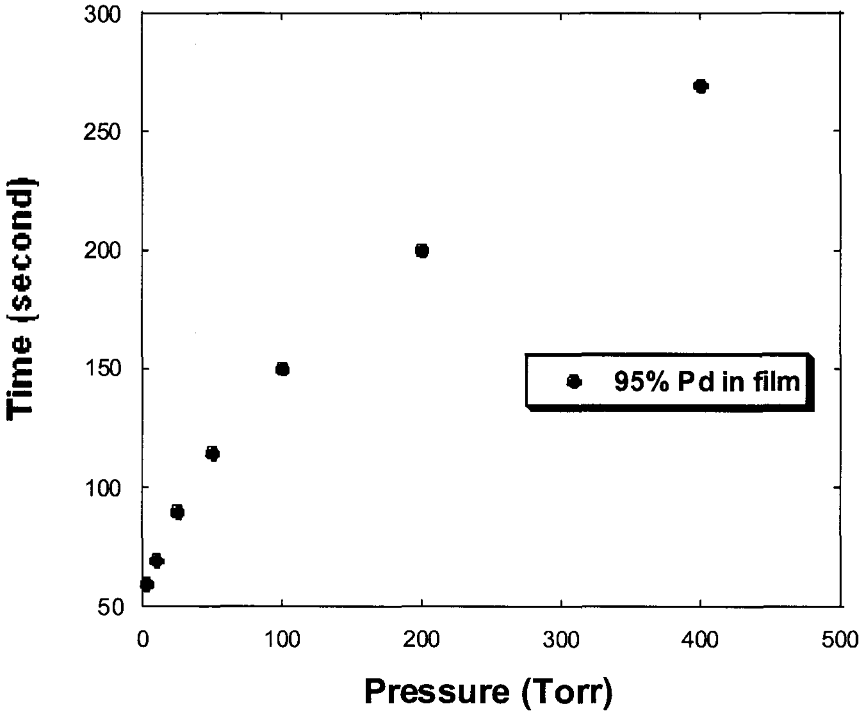

Fig. 5.12 The time to obtain 95% palladium at different pressures.

Transmission and Reflection of Pdac and Pd Films

With the spectrophotometer (Perkin-Elmer Lambda 9), we measured the transmission and reflection of palladium acetate films and palladium films (100 nm thick) from wavelengths of 200 nm to 1000 nm. Fig. 5.13 shows the transmission of palladium acetate film without the exposure of 121.6 nm radiation. From 600 nm to 1000 nm the transmission of palladium acetate film is about 80%, and it is transparent. Fig. 5.14 shows the transmission of the palladium acetate film exposed to 121.6 nm radiation for a couple of minutes and formation a palladium film. As shown in the figure 5.14, the transmission of the thin film is less than 5%. This means the palladium film was formed on the glass substrate and had less transmission.

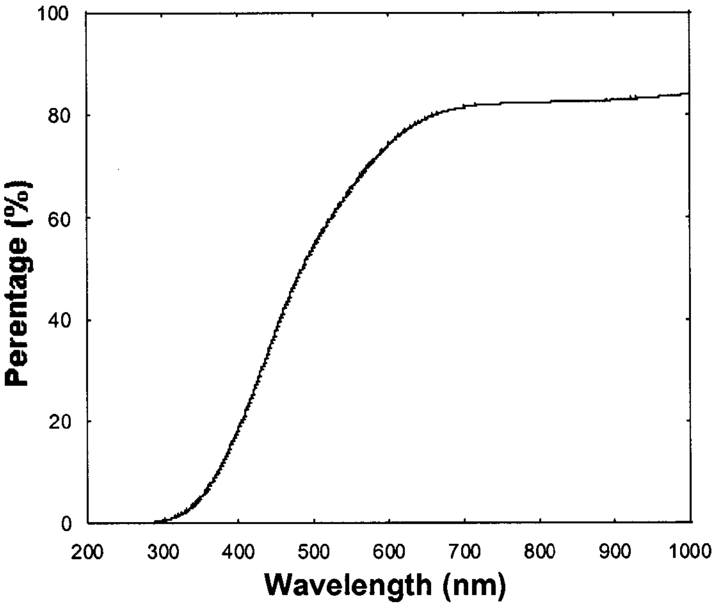

Fig. 5.13 The spectrum, measured with spectrophotometer, of the transmission of palladium acetate film.

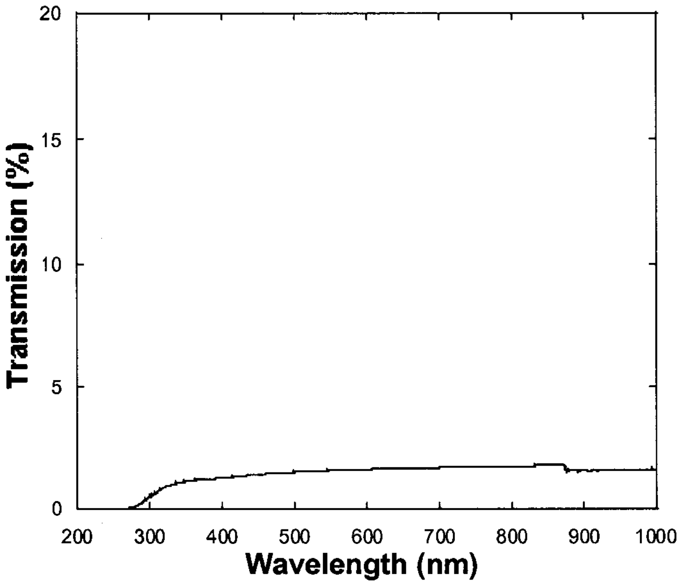

Fig. 5.14 The spectrum, measured with spectrophotometer, of the transmission of palladium film.

Figures 5.15 and 5.16 show the reflectivity of palladium acetate and palladium films, respectively. The reflectivity of palladium acetate film is about 17% from 200 nm to 1000 nm and the reflectivity of palladium film is increasing with wavelength and obtained 60% at 1000 nm. From literature we know that the reflectivity of pure palladium bulk is 72% at 1000 nm.

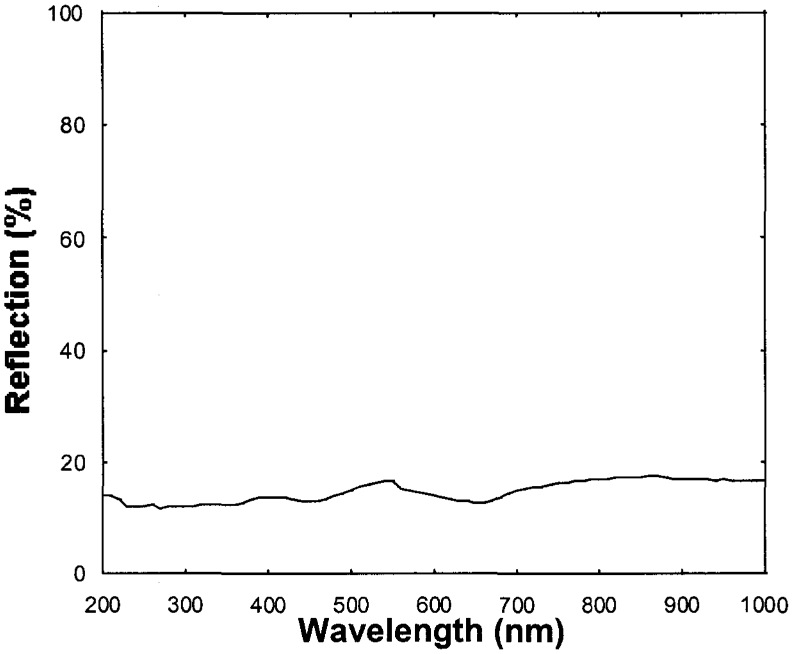

Fig. 5.15 The reflectivity of palladium acetate film.

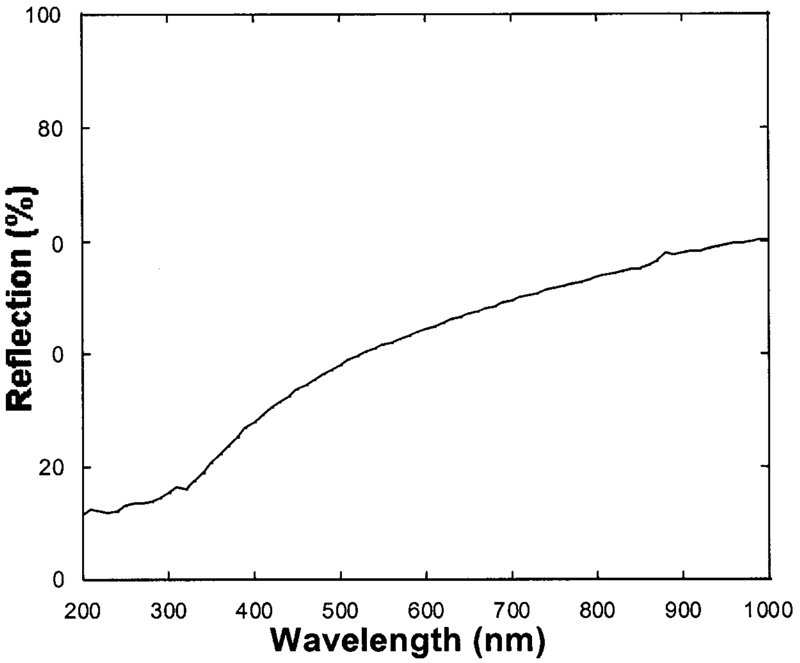

Fig. 5.16. The reflectivity of palladium film.

X-Ray Diffraction

Under continuous illumination by the Lyman-α line, the first Pd crystallite appeared and started to grow until it formed a homogeneous thin conductive metallic palladium film over the glass substrate. Using X-Ray diffraction (XRD), the crystal structure of the palladium film was studied. In our experiment, a Rigaku X-Ray diffractometer (λ = 1.538 Å) was used to measure the spectra. First, we measured palladium acetate film and we did not find the diffraction peak (Fig. 5.17). After the sample was exposed to Lyman-α, we then measured the sample. Fig. 5.18 shows the XRD spectrum of the palladium thin film.

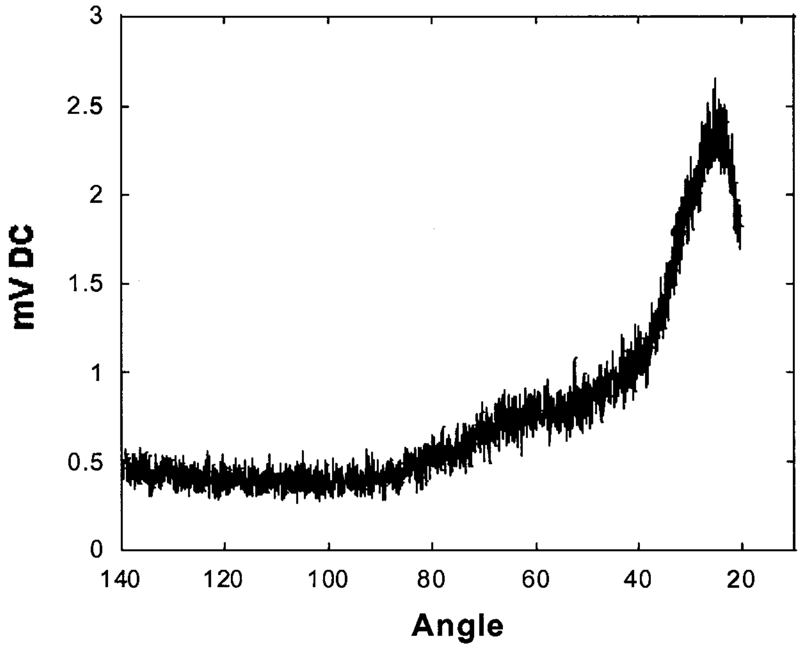

Fig. 5.17 XRD spectrum of palladium acetate film.

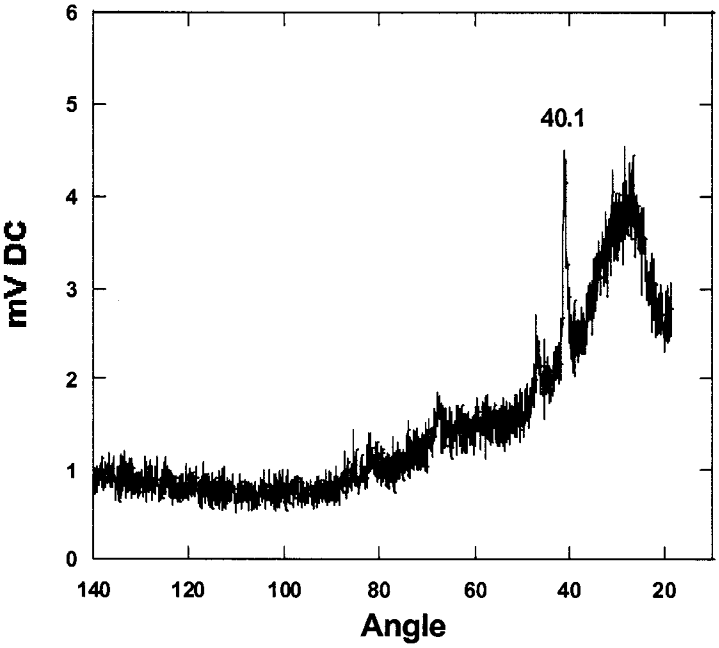

Fig. 5.18 XRD spectrum of palladium film after dissociation.

A significant diffraction peak shows at an angle of 40.1°, which is identical to the diffraction angle (2θ) of characteristic Pd [111] crystal. Here we use Bragg's law to verify the lattice structure.

Consider parallel lattice planes spaced d apart. The X-ray radiation is incident in the plane of the film surface. The path difference for X-rays reflected from adjacent planes is $2d\sin\theta$, where θ is measured from the plane. Constructive interference of the radiation forms successive planes that occur when the path difference is an integral number, n, of the wavelength, λ. According to Bragg law

$$2d\sin\theta = n\lambda \tag{5.2.2}$$

From the XRD data, we have $2\theta = 40.1°$, $n = 1$ and $\lambda = 1.538$ Å. From equation (5.2.2), we can obtain

$$d = \frac{n\lambda}{2\sin\theta} = \frac{1.538}{2\sin(20.05^\circ)} = 2.243 \text{ Å}. \tag{5.2.3}$$

According to the atomic properties of Pd, the crystal structure of Pd is fcc (111). So we have the equation for the distance of two adjacent parallel lattice planes

$$d(hkl) = a(h^2 + k^2 + l^2)^{-1/2} = a/3^{1/2} \tag{5.2.4}$$

For Pd, the lattice constant $a = 3.887$ Å. Thus

$$d = a/3^{1/2} = 2.244 \text{ Å} \tag{5.2.5}$$

The results that were calculated using equation (5.2.3) and (5.2.5) are the same. This means the film that formed on the substrate is exactly the palladium film and it is crystal line.

Thickness and Resistivity Measurement

The initial thickness of palladium acetate was approximately 300 nm. After irradiated with Lyman-α, the thickness of palladium was about 50 nm. This significant change of thickness was due to the loss of volatile products and organic species during the decomposition process. The other reason was the density of palladium is much higher than palladium acetate. The homogenous thin Pd film was observed with an optical microscope and an SEM. A Four-point technique was applied to measure the electrical resistivity of the palladium film. We found that the resistivity is approximately 200 μΩ·cm for a 50 nm thick palladium film.

5.2.3. Direct Pattern Writing

Mask Making

Contact printing photolithography was employed to directly write a Pd pattern with a MgF_2 mask. The optical materials that transmit in 121.6 nm wavelength are MgF_2 and LiF, but LiF is hygroscopic and mechanically soft, so in our experiment an MgF_2 window with a 1" diameter and 1 mm thickness was used for mask making. The MgF_2 mask was formed by pattern gratings in photoresist using i-line contact lithography. Fig. 5.19 shows the procedures for making the mask. First, a master mask with 1 μm lines and 1 μm spaces was contacted to the MgF_2 window, which had been precoated with i-line photoresist. Then, the MgF_2 window was exposed with UV light and developed. The resist lines on the MgF_2 window were opaque to 121.6 nm light and the spaces without resist were transparent. The 121.6 nm transmission of resist and MgF_2 window was measured directly with our DBD lamp and the PMT on the monochromator. From the measurement, the transmission of 300 nm thick resist is less than 1% and transmission through the pure MgF_2 window is 67%. The MgF_2 window patterned with photoresist could be used as a mask for 121.6 nm lithography. With our lithography facility, we made 5 μm line pattern masks. Cornell University National Nanofabrication Facility assisted us in making the 1 μm line pattern on MgF_2 masks using their optical lithography facility. Fig. 5.20 shows the optical microscope photograph of MgF_2 mask with 1 μm lines and 1 μm spaces.

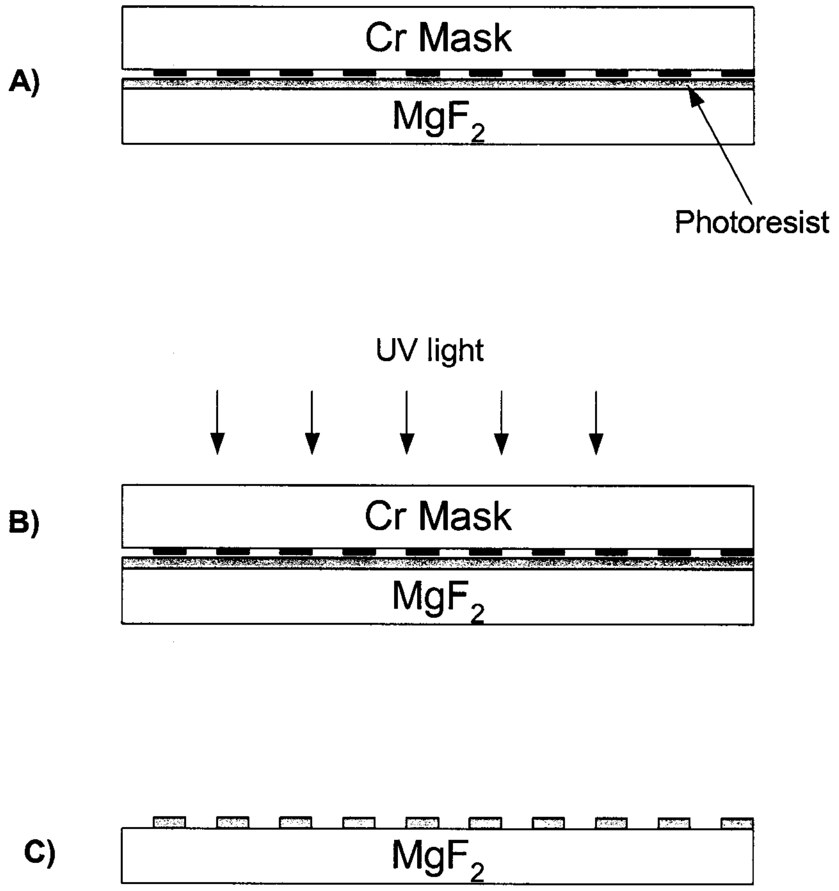

Fig. 5.19 The procedure for MgF_2 mask making, a) photo resist coating, b) exposure, c) after developing.

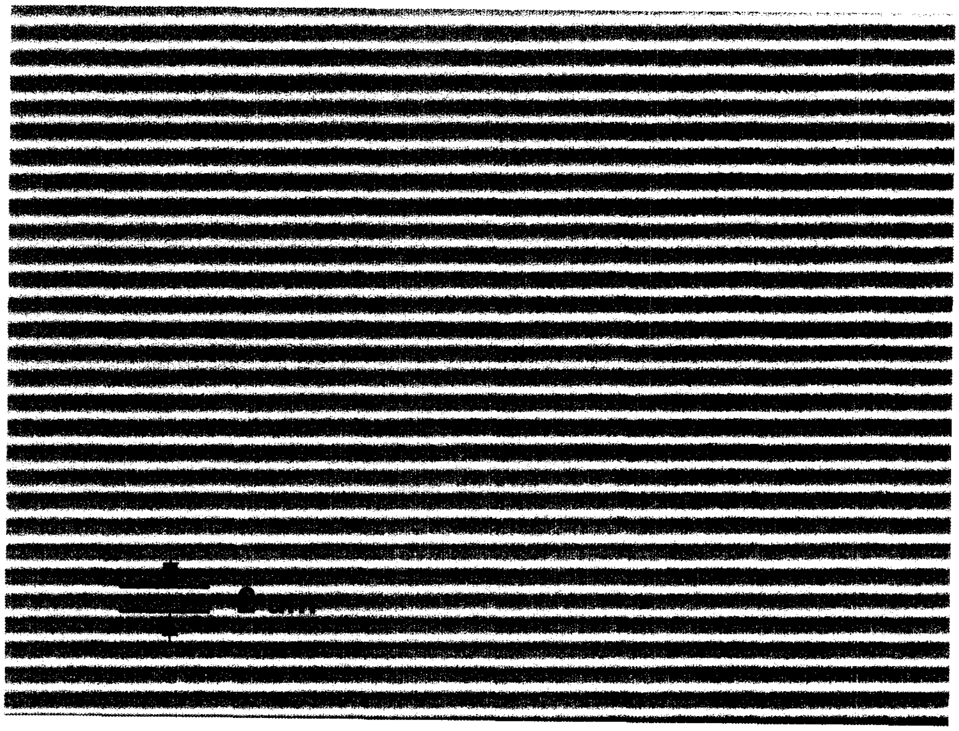

Fig. 5.20 Optical microscope photograph of the MgF_2 mask with 1 μm lines and 1 μm spaces (the light lines are the resist lines).

Pattern Writing

The MgF_2 mask was intimately contacted with the palladium acetate coated 1" diameter and 1 mm thick glass wafer. A C-mount holder was used to hold the MgF_2 mask and the glass substrate. After exposure to 121.6 nm light, the transparent area was irradiated with VUV photons and palladium lines were formed, while palladium acetate on the opaque area remained unchanged. We used chloroform liquid to wash out the residual palladium acetate and pure palladium lines were left on the glass substrate. Fig. 5.21 shows the procedure of palladium pattern making with contact printing.

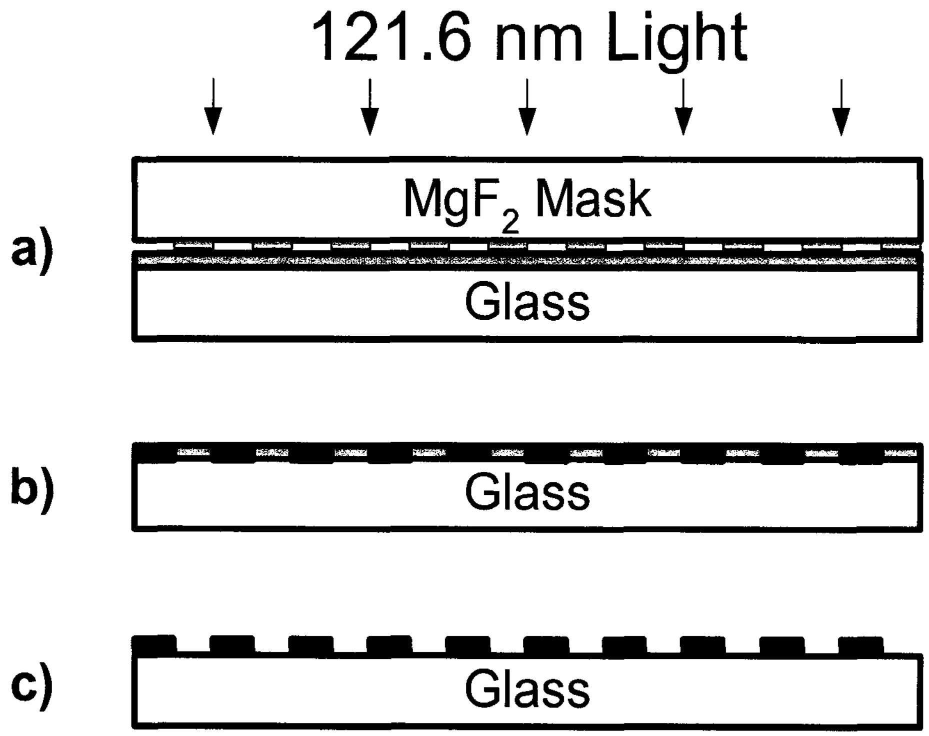

Fig. 5.21 The procedure of palladium pattern writing, a) contact printing, b) after exposure, and c) after palladium acetate removal.

Fig. 5.22 is an optical microscope photograph of the palladium pattern, which was exposed with Lyman-α radiation for 2 minutes under the low-pressure (3 Torr) discharge. Fig. 5.23 displays an SEM micrograph of the pattern on the glass substrate with a line width of 5 μm and 5 μm spacing. Figures 5.24 and 5.25 show the SEM micrograph and microscope graph of the palladium pattern with 1 μm lines and 1 μm spacing. From these figures, we observed that clear 5 μm and 1 μm palladium lines were obtained.

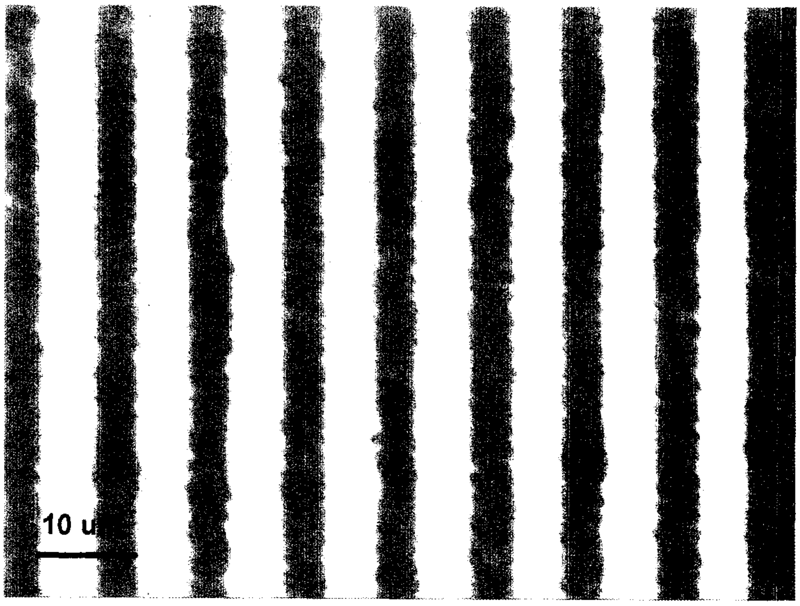

Fig. 5.22 Optical photograph of the palladium pattern (5 μm lines by 5 μm spaces).

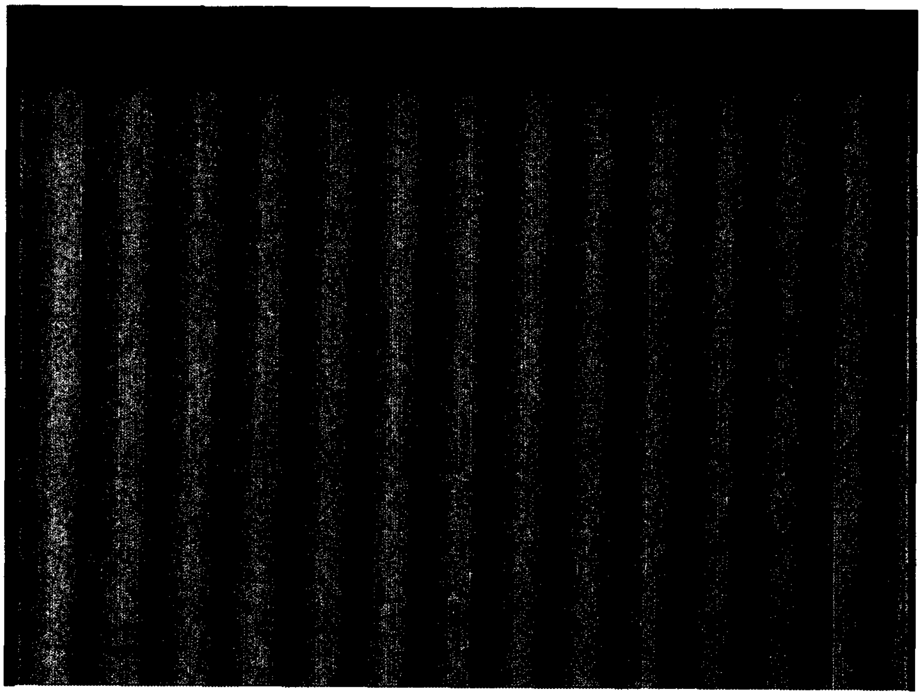

Fig. 5.23 SEM image of palladium pattern (5 μm lines by 5 μm spaces).

Fig. 5.24 SEM image of palladium pattern (1 μm lines by 1 μm spaces).

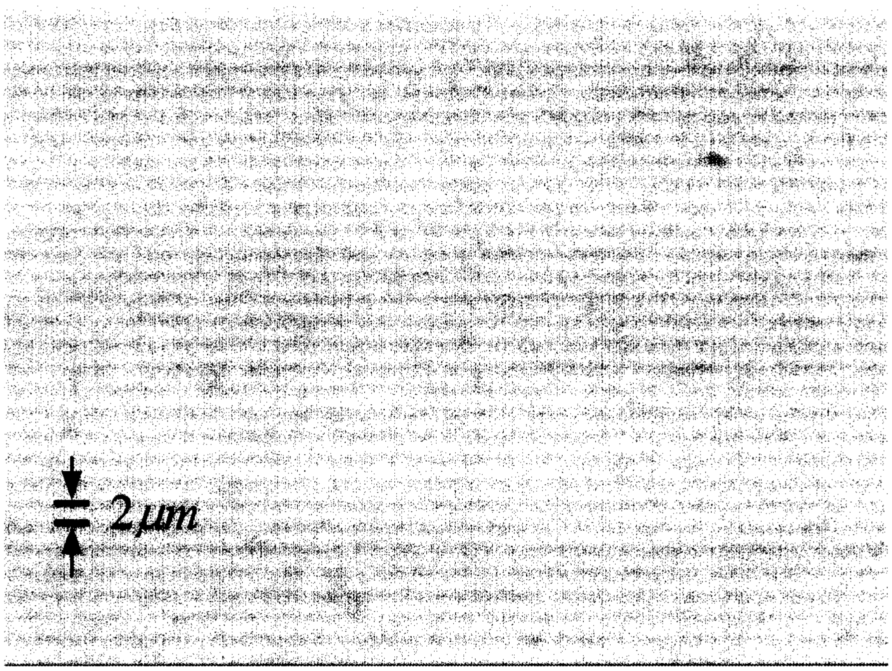

Fig. 5.25 Optical photograph of palladium pattern (1 μm lines by 1 μm spaces).

Palladium film had been formed on a glass substrate using the 121.6 nm discharge source. The growth rate of palladium was affected by radiation density and discharge pressure. High-energy photons, strong radiation flux, and low pressures enhanced the photodecomposition of palladium acetate. The results obtained with the spectrophotometer, XRD, and SEM showed that the palladium films obtained were of good quality. Direct patterning of palladium lines was demonstrated with lithography, yielding lines of 1 μm width. Lines of width less than 1 μm should be possible, and would depend on a suitable MgF_2 mask.

Cornell University National Nanofabrication Facility also made an MgF_2 mask with 200 nm line patterns using their e-beam lithography. However, the resist on that mask was PMMA and, from measurement, we found that the thin PMMA film is transparent to 121.6 nm radiation, so this mask could not work for pattern writing. The other problem is the resolution limitation of contact printing. Equation (1.3.2) defined the minimum linewidth that can be obtained by contact printing. According to this equation, if the resist thickness is 300 nm, the linewidth will be 200 nm, assuming a perfect contacting at 121.6 nm radiation. For our system setup, a 500 nm line pattern will be feasible. In conclusion, the direct palladium pattern writing with feature size less than 1 μm is possible with the photodissociation by Lyman-α and this method offers attractive applications in microcircuits, multichip interconnects, direct lithography, and prototype fabrication.

CHAPTER VI

SUMMARY AND SUGGESTIONS FOR FUTURE WORK

6.1 Dissertation Summary

The novel high-power 121.6 nm radiation source based on dielectric barrier discharge has been successfully developed for advanced lithography applications. The structure, which featured two electrodes wrapped outside the cylindrical dielectric tube, provides this source with some outstanding advantages such as compact size, easy operation, high power, and low cost.

A very intense and spectrally clean Lyman-α line was detected with a monochromator by operating the discharge in high-pressure neon mixed with trace amounts of hydrogen, which was driven by an RF power supply system. A strong radiation line only at 121.6 nm with narrow linewidth (less than 0.1 nm) was observed in the VUV region under the proper mixture of neon and hydrogen with a dynamic gas flow. From the experiment, the optimum ratio of gas mixture was about 0.06% hydrogen in neon gas by volume. If the hydrogen ratio was low, there was not sufficient hydrogen atoms excited and thus the Lyman-α radiation was low. However, at higher ratios, the recombination of atomic H into H_2 was more dominant and reduced the radiation of Lyman-α line.

Since the discharge was DBD, pressure played a significant role. The electron energy of the discharge was dependent on the value of *pd*, the production of pressure and electrode gap. The *pd* range for this discharge was from 50 Torr cm to 1000 Torr cm, and we found the pressure for highest intensity Lyman-α radiation was around 180 Torr. At lower pressures, the breakdown field was higher and neon excimer generation was not sufficient, so the radiation intensity of Lyman-α was lower. When the pressure increased, the quenching process dominated due to increasing electron density and excimer density, so that the radiation intensity dropped.

High intensity Lyman-α radiation was obtained with high RF input power. We could input 800 W RF power into the discharge and achieve a total (4π) Lyman-α radiation power of 8 W with an intensity of 12.3 mW/cm^2 at a distance of 5 cm from the detector to the source. That intensity was high enough for the lithography requirement, which only needs around 1 mW/cm^2. The maximum conversion efficiency (1.65%) from RF power to Lyman-α power occurred at an input RF power of 200 W, a gas pressure of 200 Torr, and a 0.06% H_2 gas mixture. With water-cooling electrodes and proper temperature control, the discharge could continually run over hundreds of hours with an output power fluctuation of less than 2%. This cooling system also allowed the lamp to run at a high power level without degradation from heating.

The transient emission of Lyman-α was measured with the monochromator-photomultiplier system. The Lyman-α peaks occurred continually and randomly with a pulse width (FWHM) of about 4 ns. The pulse density and the average intensity increased with the input RF power.

At high pressure, the discharge was a high intensity filament in the center of the tube. From the 2-D and 3-D beam profiles, we found the beam size was about 2 mm diameter and that size was suitable as a lithography source.

A model that involves the processes of discharge physics and plasma chemistry was used in this study. By modeling the discharge, the parameters of the discharge could be optimized and the results were in agreement with experimental measurements. From the model we concluded that the efficiency of generating Lyman-α was a function of pressure, total input energy, and density of hydrogen. The time-dependent electron current, neon excimer density, and excited hydrogen were illustrated. From the energy transfer sequences, we concluded that the radiation of Lyman-α occurred continually and randomly and would not be identical with the rf phase. This conclusion was in agreement with the results of our experiment measurements.

The electrical circuit of the discharge was modeled to achieve high efficient power transfer and obtain a high power Lyman-α source. Since the rf source and the load were not matched directly, a "Π-network" was placed between them. The advantages of this network were that it could match any discharge and provided added flexibility. In our experiment, we controlled the ratio of the reflected power to source power at less than 2%. We measured the discharge currents and voltages at different input powers and, based on these parameters, we calculated R_D, $sin(\psi)$, X_D, and C_{ab}. The capacitance (C_d) of dielectric layers was a very important factor that determined the voltage loaded on the plasma. It should be as large as possible in comparison to voltage on the plasma capacitance (C_p). There were methods to increase C_d, including increasing dielectric constant k, increasing the electrode area, and reducing the dielectric thickness.

The discharge was optimized by simulation using XOOPIC software. Results of the simulation were the electric field, electron energy and the electron and ion density profiles. At the application of an electric field, electrons gradually moved to the center of cylinder, so the density on the center area was much higher than the area near the tube wall. According to the simulation, the discharge filament was about 2 mm in diameter, which was consistent with our experimental results. In the steady state, the center of the tube had a high electron density of 2 x 10^{17} cm^{-3}. The electric field in the electrode region was higher than other regions, and had peaks at the edge of the electrodes, which had an intensity of 6 x 10^5 V/m. The average temperature of the electrons, 8 eV, in the steady state, was also obtained.

We also demonstrated strong Lyman-α radiation from low-pressure argon with trace amounts of hydrogen discharge. Argon discharges under both low and high pressures were studied to analyze the atomic resonance transition at VUV region. At low-pressure discharge, we found argon atomic lines at 104.8 and 106.6 nm, which corresponded with metastables $^3P_2$ and $^3P_0$ levels. These metastables increased the ground-state hydrogen atom by collisional dissociation of H_2 and excited the hydrogen atoms by resonant energy transfer. At low pressure, this energy transfer was enhanced, so strong Lyman-α radiation was obtained. When the pressure increased, the metastable population decreased and as a result the Lyman-α was weak. As the pressure continually increased to atmospheric pressures, the discharge mechanism was silent discharge with dominating argon excimer radiation peaking at 126 nm. In the meantime, the Ar_2^* excimers resonantly transferred energy to molecular oxygen and excited the oxygen atoms, which emitted a strong atomic line at 130 nm. If we mixed H_2 and O_2 in argon in controlled amounts, we observed that the Lyman-α radiation dominated at low pressure and oxygen atomic triplet around 130 nm dominated at high pressure. Radiation lines ranging from 100 nm to 130 nm were studied and we found that only Lyman-α line at 12.6 nm, considering spectra and intensity, would be an ideal source for lithography applications.

The lamp source was sent to MIT-Lincoln Lab for 121.6 nm lithography applications. Before using it in near-field lithography, the source was calibrated. The stability and radiation intensity met the requirement for lithography. By using a near-field phase shift MgF_2 mask, a large area of patterns with 63 nm feature size line was obtained. The feasibility of lithography at 121.6 nm wavelength was proven that would enable extension of many of the optical technologies developed at 193 and 157 nm. It was also shown that our 121.6 nm lamp was a stable source for lithography and other advanced imaging work.

Another application was direct palladium pattern writing using VUV photodissociation with 121.6 nm light irradiating a palladium acetate thin film on a glass substrate. A good quality palladium thin film was formed on the substrate from palladium acetate film after Lyman-α radiation. The palladium film was characterized with a spectrophotometer, X-ray diffraction, SEM, profilometer, and conductivity measurements. By using our lithography utility, we made the MgF_2 mask with 5 μm lines. Cornell University National Nanofabrication Facility assisted us in making 1 μm line pattern MgF_2 masks using their optical lithography facility. With these masks, we obtained 5 μm and 1 μm line patterns by contact printing lithography. Using optical microscopy and SEM, the patterns of palladium lines were seen to be clear and with good quality.

Based on the results of source characterization, the initial lithography experiment, and the direct pattern writing with VUV photodissociation, we concluded that the stable, high power 121.6 nm radiation source was suitable for lithography, nanofabrication, and other applications.

6.2 Suggestions for Future Work

Light Usage Improvement

The geometry of the discharge unit is a cylindrical dielectric tube. Only the light that radiates from the axial direction can be used and most of the 121.6 nm radiation was absorbed by the dielectric wall. Although we can apply high rf power to obtain enough intensity for lithography application, the efficiency of utilizing radiation is still low. There are some methods such as reflective mirroring, a reflective coating can be applied inside the discharge tube, to optimize the beam propagation and thus improve the efficiency. If this efficiency is improved, the electrode water-cooling can be avoided for some applications that do not need high intensity.

Large Area Structures

Based on the current design of the discharge lamp, the radiation source can be developed as a small discharge source using a small hollow tube. This source can be used to treat the irregular surface of a small area. On the other hand, we also can make a high power source with a large discharge tube with more rf power. This source can be used for large area treatment at high intensities.

High-resolution Lithography

A stable 121.6 nm lamp source can make optical lithography possible and can extend many optical technologies developed at 193 and 157 nm and their application to the 35-50 nm generations. We have used two kinds of printing technologies, contact printing and near-field phase shift printing. But the feature sizes are still limited. A projection system is still the best method to obtain 35-50 nm feature sizes. However, a projection system at that wavelength requires very high-numerical apertures and all-reflective optical designs are probably impractical. So, searching for the suitable optical materials is the biggest issue for 121.6 nm lithography.

Applications for Material Processing

High intensity Lyman-α radiation sources have potential applications for material surface processing because they have high photon energy, which has at least twice the covalent bond strength of most molecules, and plays a vital role in the initiation of photochemical processes. The related applications include polymer surface modification and material etching and coating.

High-temperature Processing at Atmospheric Pressure

The discharge can be operated at atmospheric pressures without high vacuums. We have demonstrated the argon discharge at atmosphere and a high density, high-temperature plasma was obtained. If high power lasers or microwaves are applied to the plasma, the plasma will absorb the energy efficiently and rise the temperature rapidly. This fast high temperature can be used for metal heating and improvement of the performance of metal. Metal processing applications include brazing, sintering, carbonizing, annealing, tempering, nitriding, and coating.

REFERENCES

1. T. M. Bloomstein, M.W. Horn, M. Rothschild, R.R Kunz, S. T. Palmacci, and R. B. Goodman, *J. Vac. Sci. Technol.* B **15**(6), 2112 (1997).

2. T.M. Bloomstein, M. Rothschild, R.R. Kunz, D.E. Hardy, R.B. Goodman, *J. Vac. Sci. Technol.* B **16**(6), 3154 (1998).

3. M. Rothschild, T.M. Bloomstein, J. E. Curtin, D. K. Downs, T. H. Fedynyshyn, D. E. Hardy, R. R. Kunz, V. Liberman, J. H. C. Sedlacek, R. S. Uttaro, A. K. Bates, and C. Van Peski, *J. Vac. Sci. Technol.* B **17**(6), 3262 (1999).

4. J. E. Bjorkholm, *EUV Lithography-The Successor to Optical Lithography*, Intel Technology Journal, **Q3** 1998.

5. Jos P. H. Benschop, A. J. J. Van Dijisseldonk, W. M. Kaiser, and D. C. Ockwell, *J. Vac. Sci, Technol.* B **17**(6), 2978, Nov/Dec 1999.

6. S.D. Golladay, H. C. Pfeiffer, J.D. Rockrohr, and W. Stickel, *J. Vac. Sci, Technol.* B **18**(6), 3072 Nov/Dec 2000.

7. M. Oda, M. Shimada, T. Tsuchizawa, and S. Uchiyama, *J. Vac. Sci, Technol.* B **17**(6), 3402 Nov/Dec 1999.

8. H. Loeschner, G. Stengl, R Kaesmaier, and A. Wolter, *J. Vac. Sci, Technol.* B *19*(6), 2520 Nov/Dec 2001.

9. V. Liberman, M. Rothschild, P.G. Murphy, and S. T. Palmacci, *J. Vac. Sci, Technol.* B **20**(6), 2567 Nov/Dec 2002.

10. J. Yan, A. El-Dakrouri, M. Laroussi, and M. Gupta, *J. Vac. Sci, Technol.* B **20**(6), 2574 Nov/Dec 2002.

11. J. Yan and M. Gupta, *J. Vac. Sci, Technol.* B **20**(6), 2839 Nov/Dec 2003.

12. W. R. Ott, K. Behringer, and G. Gieres, *Applied Optics* **14**(9), 2121 (1975).

13. A. Hollander and M. R. Wertheimer, *J. Vac. Sci. Technol.* A **12**(3), 879 (1994).

14. A. C. Fozza, A. Kruse, A. Hollander, A. Ricard, M. R. Wertheimer, *J. Vac. Sci. Technol.* A **16**(1), 72 (1998).

15. P. Kurunczi, H. Shah, and K. Becker, *J. Phys. B*, **32**(22), L651 (1999).

16. M. Spaan, A. Goehlich, V. Schulz-von der Gathen, and H. F. Dobele, *Applied Optics* **33**(18), 3865 (20).

17. M. Laroussi, in *Proc. IEEE Int. Conf. Plasma Science*, 203 (1999).

18. B. Eliasson and U. Kogelschatz, *IEEE Trans. On Plasma Sci.* **19**(2), 309 (1991).

19. B. Gellert and U. Kogelschatz, *Appl. Phys.* B **52**, 14 (1991).

20. P. Castrucci, W. Henley, W. Liebmann, "*SolidState Technology*", 1997.

21. M. Rothschild and D. J. Ehrlich, *J. Vac. Sci. Technol.* B **6**(1), 1 (1998).

22. M. Rothscild, M. W. Horn. C. L. Keast, R. R. Kunz, V, Liberman, S. C. Palmateer, S. P. Doran, A. R. Forte, R. B. Goodman, J .H.C. Sedlacek, R. S. Uttaro, D. Corliss, and A. Grenville, *The Lincoln Laboratory Journal*, **10**(1) 1997.

23. John Canning, *J. Vac. Sci. Technol.* B **16**(6), 2109 (1997).

24. Ch. K. Rhodes, "*Eximer Lasers*", Springer-Verlag Berlin Heidelberg New York 1979.

25. K. H. Schoenbach, A. El-Habachi, W. Shi, and M. Ciocca, *Plasma Sources Sci. Technol.* **6**, 468-477 (1997).

26. A. El-Habachi and K. H. Schoenbach, *Appl. Phys. Lett.* **72**(1) 22, (1998).

27. W. Shi, R. H. Stark, and K. H. Schoenbach, *IEEE Trans. on Plasma Sci.* **27**(1) 16, 1999.

28. O. Motret, J. M. Pouvesle, and J. Stevefelt, *J. Chem. Phys.* **83**(3), 1095 (1985).

29. J. Wieser, M. Salvermoser, L. H. Shaw, A. Ulrich, D E Murnick and H. Dahi, *J. Phys. B.* **31**, 4589 (1998).

30. P. Kurunczi, H. Shah, and K. Becker, *J. Phys. B*, **32**(22), L651 (1999).

31. S. M. Hooker and C. E. Webb, *VUV laser, Prog. Quant. Electr.* **18**, 227-274 (1994).

32. J. A. Samson, D. L. Ederer, "*Vacuum Ultravaiolet Spectroscopy I, II*," Academic Press, San Diego, CA 1998.

33. B. Stevens, E. Hutton: *Nature* **186**, 1045 (1960).

34. J. R. Murray, C.K. Rhodes, *J. Appl. Phys.* **47**, 5041 (1976).

35. R.S. Mulliken, *Phys. Rev.* **136**, A962 (1965).

36. M.L. Ginter, C. M. Brown, *J. Chem. Phys.* **56**, 672 (1972).

37. B. Liu, H.F. Schaefer, III, *J. Chem. Phys.* **55**, 2369 (1971).

38. 38 D.H. Liskow, H.F. Schaefer, III, P.S. Bagus, B. Liu, *J. Am. Chem. Soc.* **95**, 4056 (1973).

39. D.C. Lorents, *Physica* **82C**, 19 (1976).

40. G.R. Fournier, *Opt. Commun.* **13**, 385 (1975).

41. C.W. Werner, E.V. George, P.W. Hoff, C.K. Rhodes, *Appl. Phys. Lett.* **25**, 235 (1974).

42. E.V. George, CK. Rhodes, *Appl. Phys. Lett.* **23**, 139 (1973).

43. M.H.R. Hutchinson, *Inst. Phys. Conf. Ser.* **29**, 109 (1976).

44. B. Eliasson and U. Kogelschatz, *Appl. Phys.* B **46**, 299-303 (1988).

45. P.K. Leichner, *Phys. Rev.* A**8**, 815 (1973).

46. B. Schneider, J.S. Cohen, *J. Chem, Phys.* **61**, 3240 (1974).

47. T. Oka, K. Rama Rao, J. Redgath, R .Firestone, *J. Chem. Phys.* **61**, 4740 (1974).

48. N. Thonnard, G.S. Hurst, *Phys. Rev.* A**5**, 1110 (1972).

49. R. Bocique, P. Mortier, *J. Phys.* D**3**, 1905 (1970).

50. J. W. Keto, R.E. Gleason, G.K. Walters, *Phys. Rev. Lett.* **33**, 1375 (1974).

51. P.K. Leichner, R.J. Ericson, *Phys. Rev.* A**9**, 251 (1974).

52. M.A. Dubinskii, A.C. Cefalas and C.A. Nicolaides, *Opt. Commun.* **88**, 122 (1992).

53. J. B. West and H. A. Padmore, "*Handbook on Synchrotron Radiation*," Vol , Elsevier, Amsterdam, 1987.

54. A. Hofmann, *Phys. Reports* **64**. 253 (1980).

55. K. Kim, *J. AIP Proc.* **184**, 565 (1989).

56. G.R. Neil and L. Merginga, *Reviews of Modern Physics* **74**, 685 2002.

57. S. Benson, G. Biallas, C. Bohn, D. Douglas, H.F. Dylla, R. Evans, J. Fugitt, R. Hill, K. Jordan, G. Krafft, R. Legg, R. Li, L. Merminga, G.R. Neil, D. Oepts, P. Piot, J. Preble, M. Shinn, T. Siggins, R. Walker, B. Yunn, *Nuclear Instruments and Methods A* **429** 29 (1999).

58. G. Dattotli and A. Renieri, *Nuclear Instruments and Methods in Physics Research* A**507**, 464 (2003).

59. J. Pfluger, U. Hahn, B. Faatz, M.T. Tischer, *Nuclear Instruments and Methods in Physics Research* A**507**, 228 (2003).

60. B. E. A. Saleh, M. C. Teich, "*Fundamentals of Photonics,*" Wiley-Interscience, 1991.

61. "*NIST Atomic Spectra Database*", from http://physics.nist.gov/cgi-bin/AtData/main_asd.

62. W. Ott, J. Bridges, and J. Klose, *Opt. Lett.* **5**, 225 (1980).

63. H. Greim, *"Plasma Spectroscopy"*, McGraw-Hill, New York, 99. 293-394 (1964).

64. F. Burger and J. Maier, *J. Phys. E: Sci. Instrum.* **8**, 420 (1975).

65. A. McIlraith, *Nature*, London 212, 1422 (1966).

66. W. Wiese, "*Methods of Experimental Physics*", Academic Press, New York, pp. 307 (1968).

67. J. Morris and R. Garrison. *J. Quant. Spectrosc. Radiat. Transfer* **6**, 899 (1966).

68. A.T. M Wilbers and D. C. Schram, *J. Quant. Spectrosc. Radiat. Transfer* **46**(4), 299-308 (1991).

69. W. Wiese, D. Paquette, and J. Solarski, *Phys. Rev.*, **129**, 1225-1232 (1963).

70. J. Roth, in "*Industrial Plasma Engineering, Vol 1: Principles,*" Institute of Physics Publishing, Bristol and Philadelphia (1995).

71. W. Poffel and K.H. Schartner, *Rev. Sci. Instrum.* **61**, 613-615 (1990).

72. M. Jogwich, B. Huber, and K. Wiessenamm, *Z. Phys. D* **17**, 171-179 (1990).

73. F. Fehsenfeld, K. Evenson, and H. Broida, *Rev. Sci. Instrum.* **36**, 294-298 (1965).

74. D. Heine, J. Babis, and M. Denton, *Appl. Spectrosc.* **34**, 595-598 (1980).

75. M. Denton, M. Pilon, and J. Babis, *Appl. Spectrosc.* **44**, 975-978 (1990).

76. J.W. Carr and M. W. Blades, *Spectrochimica Acta*, vol. **39**B (4), 567-574, (1984).

77. G. Schonhense and U. Heinzmann, *J. Phys. E: Sci. Instrum.* **16**, 74-82 (1983).

78. D. Mason, D. Mintz, and A. Kuppermann, *Rev. Sci Instrum.* **48**, 926-933 (1977).

79. B.E. Varner, K.B. Persson, and G.J. Gollins, *J. Appl. Phys.* **50**, 5694-5703 (1979).

80. H. Koch and H. J. Eichler, *J. Appl. Phys.* **54** (9), 4939-4946 (1983).

81. K. Danzmann, J. Fischer, and M. Kuhne, *J. Phys. D: Appl. Phys.* **18**, 1299-1305 (1985).

82. K. Danzmann, M. Gunther, J. Fischer, M. Koch, and M. Kuhne, *Appl. Opt.* **27**, 4947-4951 (1988).

83. J. Hollandt, M. Kuhne, and B. Wende, *Appl. Opt.* **33**, 68-74 (1994).

84. J. Hollandt, M. Kuhne, M.C.E. Huber, and B. Wende, *Astron. Astrophys. Suppl. Ser.* **115**, 561-572 (1996).

85. C. Heise, J .Hollandt, R. Kling, M. Kock, and M. Kuhne, *Appl. Opt.* **33**, 5111-5117 (1994).

86. W. Walter, U. Schaller, and H. Langfoff, *J. Chem. Phys.* **83**(4), 1667-1670 (1985).

87. M. Savlermoser, D.E. Murnick, J. Wieser, and A. Ulrich, *J. Appl. Phys.* **88**(1), 453-459 (2000).

88. W. Jans, B. Mobus, M. Kuhne, G. Ulm, A. Werner, and K. H. Schartner, *Phys. Rev. A.* **55**, 1890-1898 (1997).

89. U. Kogelschatz, *Appl. Surf. Sci.* **54**, 410-423 (1992).

90. J.Y. Zhang and I.W. Boyd, *J. Appl. Phys.* **84** (3), 1174-1178 (1998).

91. R.P. Mildren, R.J. Carman, and I. S. Falconer, *J. Phys. D: Appl. Phys.* **34**, 3378-3382 (2001).

92. F. Kessler and G.H. Bauer, *Appl. Surf. Sci.* **54**, 430-434 (1992).

93. P. Bergonzo, P. Patel, I.W. Boyd, *Appl. Surf. Sci.* **54**, 424-429 (1992).

94. P. Bergonzo, U. Kogelschatz and I.W. Boyd, *Appl. Surf. Sci.* **69**, 393-397 (1993).

95. A.El-Dakrouri, J. Yan, M.C. Gupta, M. Laroussi, and Y. Badr, *J. Phys. D: Appl. Phys.* **35**, L109-L114 (2002).

96. E. M. Gullikson, R. Korde, L. R. Canfield, and R. E. Vest, *J. Electron Spectr. Related Phenomena* **80**, 313 (1996).

97. Yu. D. Korolev and G. A. Mesyays, *Physics of pulsed breakdown in gases*, URO-press, 1998.

98. M. A. Lieberman, A. J. Lichtenberg, "*Principles of Plasma Discharges and Materials Processing*", John Wiley & Sons, Inc. 1994.

99. J. P. Verbonconeur, A. B. Langdon and N. T. Gladd, *Phys. Comm.* **87**, 199 (1995).

100. C. H. Shon, J. K. Lee, H. J. Lee, Y. Yang, and T. H. Chung, *IEE Trans. Plasma Sci.,* Vol. **26** (6), 1635 (1998).

101. D. Bruhwiler, J. Cary, J. Verboncoeur, P. Mardahl, and R. Giacone, *Proceeding of EPAC 2000*, Vienna, Austria, **877** (2000).

102. I. Velchev, W. Hogervorst and W. Ubachs, *J. Phys. B: At. Mol. Opt. Phys.*, L511-L516 (1999).

103. M. Moselhy, R.H. Stark, K.H. Schoenbach, and U. Kogelschatz, *Appl. Phys. Lett.* **78** (7), 880-882 (2001).

104. K. H. Becker and P. Kurunczi, *Physics of Plasmas* **9** (5), 2399-2404 (2002).

105. K. Watanbe, E.C. Y. Inn and M. Zelikoff, *J. Chem. Phys.* **21**, 1026 (1953).

106. S. Ogawa and M. Ogawa, *Can. J. Phys.* **53**, 1846 (1975).

107. J. Yan and M. Gupta, *J. Vac. Sci. Technol.* B**22**(6), 3202-3205 (2004).

108. D.F. Heath and P. A. Sacher, *Appl. Opt.* **5**, 937 (1966).

109. J. A. Rogers, K. E. Paul, R.J. Jackman, and G.M. Whitesides, *J. Vac. Sci. Technol.* B**16**(1), 59-68 (1998).

110. A.R. Calloway, T.A. Galantowicz, and W.R. Fenner, *J. Vac. Sci. Technol.* A **1**(2) 1983.

111. M. Hanabusa, A. Oikawa, and P.Y. Cai, *J. Appl. Phys.* **66**(7), 1989.

112. C. Lavoie, M. Meunier, R. Izquierdo, S. Boivin, and P. Desjardins, *Appl. Phys. A* **53**, 339-342 (1991).

113. D. K. Flynn, J. I. Steinfeld, and D. S. Sethi, J. *Appl. Phys.* **59** (11), (1986).

114. R. Haight, P. Longo, and A. Wagner, J. *Vac. Sci. Technol.* A **21**(3), (2003).

115. J.Y. Zhang, I. W. Boyd, S. Draper, *Surface and Coating Technol.* 100-101 (1998).

116. Y. Zhang and M. Stuke, *Appl. Surf. Sci.* **46**, 153-157 (1990).

117. H. Esrom and U. Kogelschatz, *Appl. Surf. Sci.* **54**, 440-444 (1992).

118. J.Y. Zhang, H. Esron, and I.W. Boyd, *Appl. Surf. Sci.* **96-98**, 399-404 (1996).

119. J.Y. Zhang, I.W. Boyd, *Appl. Phys.* A **65**, 379-382 (1997).

VITA

JIANXUN YAN

Education:

Doctor of Philosophy (Electrical Engineering), Old Dominion University, Norfolk, Virginia May 2005

Mater of Science (Technology & Applications of Accelerator), Institute of High Energy Physics, Chinese Academy of Science, Beijing, China July 1997

Bachelor of Science (Electrical Engineering), Hunan University, Hunan, China, July 1991

Experience:

Research Assistant August 1999 – Present
Applied Research Center, Old Dominion University, Norfolk, Virginia

Electrical Engineer July 1998 – August 1999
Jefferson Lab, Newport News, Virginia

Electrical Engineer August 1994 – July 1998
Institute of High Energy Physics, Chinese Academy of Science, Beijing China

Electrical Engineer August 1991 – July 1994
The Plant of Jiangsu Mechanics, Nanjing, China

PUBLICATIONS AND PRESENTATIONS

Publication:

"Direct Metal Pattern Writing by VUV Photodissociation," J. Yan and M.C. Gupta, J. Vac. Sci. Technol. B **22** (6), Nov/Dec. 2004.

"High Power 121.6 nm Radiation Source," J. Yan, M.C. Gupta, J. Vac. Sci. Technol. B **21**(6), 2003.

"121.6 nm radiation source for advanced lithography," J. Yan, A. El-Dakrouri, M. Laroussi, M. C. Gupta, J. Vac. Sci. Technol. B **20**(6), Nov/Dec 2002, 2574-2577.

"VUV emission from a novel DBD-based radiation source," A. El-Dakrouri, J. Yan, M.C Gupta, M. Laroussi, and Y Badr, J. Phys. D: Appl. Phys. **35** (2002) L109-L114.

Presentation:

Oral presentation on the **46th** International Conference on Electron, Ion and Photon Beam Technology & Nanofabrication (EIPBN), Anaheim, CA, May 28-31, 2002.

Oral presentation on the **47th** International Conference on EIPBN, Tampa, FL, May 27-30, 2003.

Poster presentation on the **48th** International Conference on EIPBN, San Diego, CA, June 1-4, 2004.

121.6 nm radiation source for advanced lithography

Jianxun Yan, Ashraf El-Dakrouri, Mounir Laroussi, and Mool C. Gupta[a)]
Applied Research Center, College of Engineering and Technology, Old Dominion University, Newport News, Virginia 23606

(Received 28 May 2002; accepted 26 August 2002)

A vacuum ultraviolet (VUV) light source based on a high-pressure cylindrical dielectric barrier discharge (DBD) has been developed. Intense and spectrally clean Lyman-α line at 121.6 nm was obtained by operating a DBD discharge in neon with a small admixture of hydrogen. The spectrum, optical power, stability, and efficiency of the source were measured. The influence of the gas mixture and total gas pressure on the VUV intensity has been investigated. Maximum optical power of 3.2 W and spectral width <0.03 nm was achieved. Power stability of ±2% for 100 h of operation has also been obtained. The newly developed Lyman-α line source at 121.6 nm appears very promising for advanced lithography and other applications. © *2002 American Vacuum Society.* [DOI: 10.1116/1.1515302]

I. INTRODUCTION

Lithography at 157 nm with fluorine lasers is widely considered to be the last generation of conventional photolithography methods for sub-100 nm device fabrication. 100 nm lithography and beyond will be performed with next-generation lithography technologies such as x-ray, extreme ultraviolet (UV) (~13 nm), electron beams, and ion beams. But these alternatives represent a more radical deviation from the present optical-based technology, and thus they encounter more engineering challenges.[1] It has become apparent that a more mainstream extension of optical lithography should be considered as well. One of the alternatives is 121.6 nm technology. Therefore, the development of an intensive 121.6 nm light source appears to be necessary.

121.6 nm, Lyman-α line ($2p\,^2P_0 \rightarrow 1s\,^2S$), is emitted from an atomic transition in hydrogen, and is sufficiently narrow for lithography. There are many plasma-based methods which can achieve 121.6 nm line emission. Examples are arc discharge,[2] microwave excited discharge,[3] glow discharge,[4] microhollow cathode discharge,[5] and laser induced plasma.[6] Here we explore a discharge lamp based on a variant of the dielectric barrier discharge (DBD).[7] The DBD configuration is characterized by the presence of at least one dielectric layer in the current path between the electrodes and discharge space.[8,9] The dielectric barrier serves two functions. It distributes the microdischarges evenly over the entire electrode area and it limits the amount of charge and energy that can be fed into an individual filament. The plasma conditions of these microdischarges are ideal for excimer formation, in which a major fraction of the energy gained by the electrons in the electric field can be deposited in excited atomic and molecular states. One important feature of the DBD is that the plasma parameters can be influenced and thus optimized by external means. The reduced electric field E/n (n is gas density), which mainly controls the mean electron energy, can be influenced by the pressure in the discharge, the electrode spacing, and voltage slope at breakdown. On the other hand, the electron density in a microdischarge can be controlled again by pressure and by the properties of the dielectric barrier. The simplicity, versatility, and low cost of the DBD make them attractive for generating the Lyman-α line.

Due to the high excitation energy of rare-gas ions or excited rare-gas atoms, the Lyman-α line can be obtained under various excitation conditions when trace amounts of hydrogen are added to rare gas. For example, intense Lyman-α was observed in He–H$_2$ mixture near atmospheric pressure.[10] Argon/hydrogen mixture in low pressure glow discharge has been investigated to generate vacuum ultraviolet (VUV) for the photochemical treatment of polymer surfaces.[4] Energy transfer from neon ions to hydrogen molecules has been studied by an e-beam induced light source to obtain a strong intense Lyman-α line.[11] Neon–hydrogen mixture in a high-pressure discharge was shown to be a very efficient and selective method for generating Lyman-α.[5] The process of neon excimer formation, the resonant energy transfer from neon excimer molecules to molecular hydrogen, and subsequent light emission are shown as follows:

$$\mathrm{Ne} + e^- \rightarrow \mathrm{Ne}^+ + 2e^-, \tag{1a}$$

$$\mathrm{Ne}^+ + 2\mathrm{Ne} \rightarrow \mathrm{Ne}_2^+ + \mathrm{Ne}, \tag{1b}$$

$$\mathrm{Ne}_2^+ + e^- \rightarrow \mathrm{Ne}^* + \mathrm{Ne}, \tag{1c}$$

where Ne* denotes a metastable neon atom. Alternatively, Ne* can be the product of direct electron impact:

$$\mathrm{Ne} + e^- \rightarrow \mathrm{Ne}^* + e^-. \tag{1d}$$

Neon excited molecular complexes without stable ground states, also called excimers, are formed by a three-body reaction of a metastable neon atom and two atoms in the ground state

$$\mathrm{Ne}^* + \mathrm{Ne} + \mathrm{Ne} \rightarrow \mathrm{Ne}_2^* + \mathrm{Ne}. \tag{2}$$

Resonant energy transfer from Ne_2^* (14.8±0.8 eV) to molecular hydrogen leads to H$_2$ dissociation (4.48 eV) and excitation H* (10.2 eV),

---

[a)] Electronic mail: mgupta@odu.edu

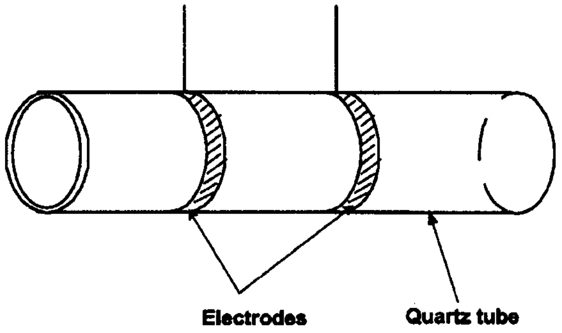

FIG. 1. Cylindrical DBD configuration with ring electrodes.

$$\mathrm{Ne}_2^* + \mathrm{H}_2 \rightarrow 2\mathrm{Ne} + \mathrm{H} + \mathrm{H}^*(n=2). \tag{3}$$

Excited hydrogen atoms spontaneously emit the Lyman-α line

$$\mathrm{H}^* \rightarrow \mathrm{H} + h\nu(121.6\ \mathrm{nm}). \tag{4}$$

II. EXPERIMENTS

The discharge geometry used in our experiments is cylindrical, featuring a hollow quartz (or alumina) tube and two copper-ring electrodes wrapped around the outer surface of the tube[7,12] (see Fig. 1). Since the electrodes are out of the discharge volume, electrode erosion and contamination of the plasma with metal vapor is avoided. The length, diameter, and thickness of the tube, and the distance between the ring electrodes are variable, thus the plasma can be optimized by adjusting external parameters.

The experimental setup consists of the discharge unit, monochromator, detector, gas inlet and outlet assembly, pump system, and rf power supply with impedance matching network. The system is schematically shown in Fig. 2. The discharge unit is a 115 mm×8 mm o.d.×4 mm i.d. quartz tube, which connects with two flanges by two O-rings to vacuum seal the tube. The whole discharge unit is fixed on an 8.5 cm six-way cross cube, on which a monochromator and photodetector can be easily mounted. The monochromator is connected with the cube chamber by a flange adapter, on which a window could be installed. The system can either have a window or be windowless. For the Lyman-α line, the LiF window was used to transmit the radiation, because its short-wavelength cutoff is at 105 nm. On the other side of the cube, the gas inlet flange and detector chamber, which contains a filter and a silicon photodiode, are mounted. The discharge is ignited with a rf power supply system, which consists of a 13.56 MHz rf generator and an impedance matching network.

Before generating the plasma, the discharge unit, monochromator, and detector were evacuated to 10^{-6} Torr. High vacuum was necessary before filling the neon and hydrogen gas, to avoid emission from impurities such as O, N,.... Two flow meters, one connecting with high purity neon and the other with 1% hydrogen/neon mixture (research grade), controlled the flow rate and ratio of hydrogen and neon. A needle valve and flow meters were adjusted together to control the flow rate and to maintain a constant pressure in the lamp. The lamp was operated in a dynamic mode, which had a gas flow rate of 600 sccm. The plasma was initially ignited at a relatively low pressure (less than 100 Torr). The discharge formation rf power depended on pressure p, electrode gap width d, and type of dielectric.

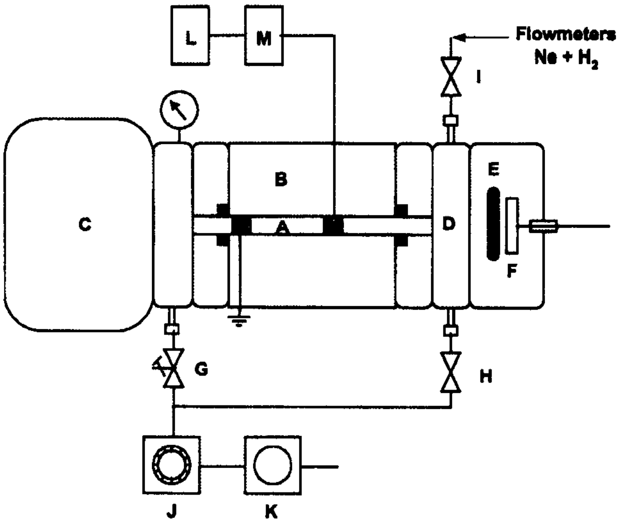

FIG. 2. Schematic drawing of the experiment setup. (A) Quartz tube, (B) chamber, (C) monochromator, (D) gas inlet and outlet flange, (E) filter, (F) semiconductor detector, (G) needle valve, (H and I) valves, (J) turbo pump, (K) roughing pump, (L) rf generator, and (K) matching network.

III. RESULTS AND DISCUSSION

Emission spectra were measured with a 0.2 m McPherson scanning monochromator (model 320). Intense Lyman-α radiation was observed as the only strong radiation in the entire VUV spectrum. Figure 3 shows the emission spectrum at a pressure of 500 Torr, with a neon gas containing 0.058% hydrogen and a flow rate of 600 sccm. The emission line has a bandwidth of less than 0.1 nm full width half maximum (FWHM) and was limited by the resolution of the monochromator, which has grating of 1200 G/mm. The range of hydrogen from 0.03% to 0.12% was found to be the ideal range to achieve a Lyman-α line dominated spectrum. Beyond this range, the intensity of the line would dramatically decrease, and other lines, 130 nm from oxygen, 156 and 165 nm from carbon, would relatively increase. According to our experimental results, the optimum ratio for intense Lyman-α line is about 0.06% hydrogen in neon. The pressure and electrode gap also influenced the intensity of Lyman-α. From our experiment, the optimum range of pd value was from 50–100 Torr cm. This represents a great advantage over many other discharge types, because of the relative simplicity in changing the pressure–electrode gap product. Thus in a fairly simple way one can adjust this important plasma parameter to optimize the yield of the excimer and Lyman-α emission.

The absolute intensity of the Lyman-α radiation was measured by a silicon photodiode[13] (IRD company, model SXUV-100), which has 1 cm×1 cm active area and 0.01 A/W responsivity at 121.6 nm. A narrowband filter located

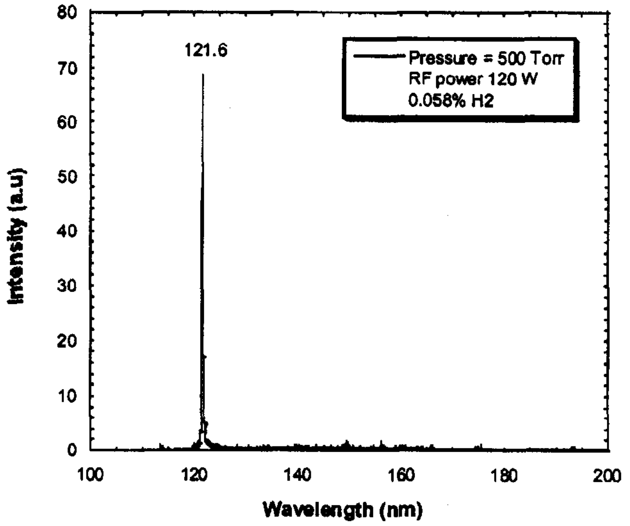

FIG. 3. Emission spectrum of neon/hydrogen mixture at a pressure of 500 Torr.

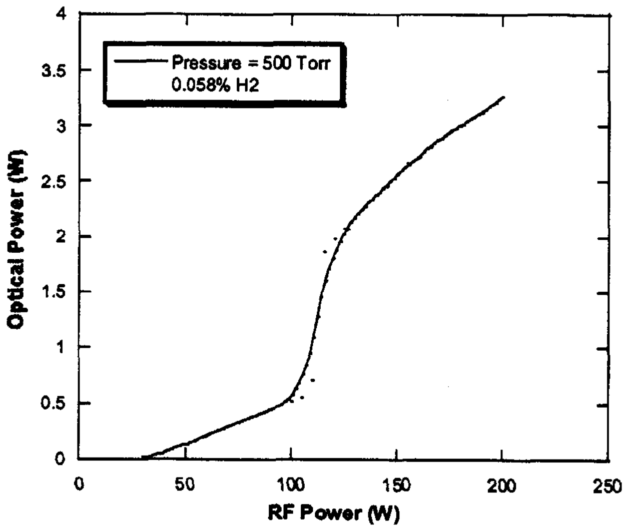

FIG. 4. Total optical power dependence on the input rf power at pressure of 500 Torr.

between the discharge unit and the detector was used. It has peak transmittance at 119.6 nm, FWHM of 13.5 nm, and a transmission efficiency of 15% at 121.6 nm. Although visible light in the red region was radiated with a low intensity compared to the Lyman-α nm radiation (1:30), it is necessary to block out this radiation with the filter. The intensity that the detector measured was that of 121.6 nm. The discharge is a filament source with 2 mm diameter and 3 cm length. The calculation of total power was based on a line source. Figure 4 shows the total optical power increased with rf input power. At a pressure of 500 Torr and rf input power of 200 W, we obtained emission intensity of 5.3 mW/cm^2 on detectors, which had a distance of 5 cm from the front edge of the source. The maximum total optical power of 3.2 W and with an efficiency of 1.6% was obtained. In order to generate more power, a stronger rf field should be applied to the discharge. For increased efficiency, the impedance of the discharge and that of the rf generator should match. Since the capacitance of the discharge was variable, a wide load-matching range network was specially designed to meet the impedance matching criterion.

Beam profile was measured to identify the emission intensity across the beam cross section. At low pressures the tube was filled with the discharge, and the whole section had a nearly uniform intensity. As the pressure increased, the discharge restricted toward the center and a filament between two electrodes was formed. The front view of the discharge appeared like a 2 mm diam disk, and the side view was a line source. Figure 5 shows the two-dimensional (2D) and three-dimensional (3D) beam profiles at 500 Torr. Since we could not image beam profile at 121.6 nm directly, these images were based on the visible light generated in the discharge.

Power stability is an important criterion for a lamp used in lithography applications. Preliminary tests showed that our source was capable of continuous operation over a 24 h period with rf input power of 120 W and total optical power of about 2.0 W (Fig. 6). The average emission intensity on the detector was 3.34 mW/cm^2 with a distance of 5 cm from the source. During the 24 h of operation the power fluctuation was less than ±2% and without power degradation.

IV. CONCLUSIONS

We have demonstrated a DBD-based VUV source that emits strong radiation at 121.6 nm. Using high-pressure neon

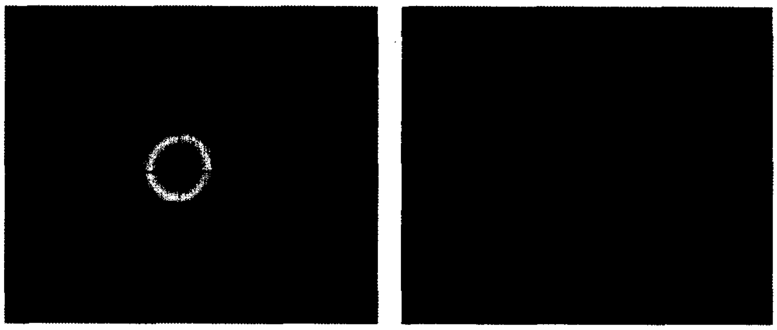

2 – D

3 - D

FIG. 5. 2D and 3D beam profile.

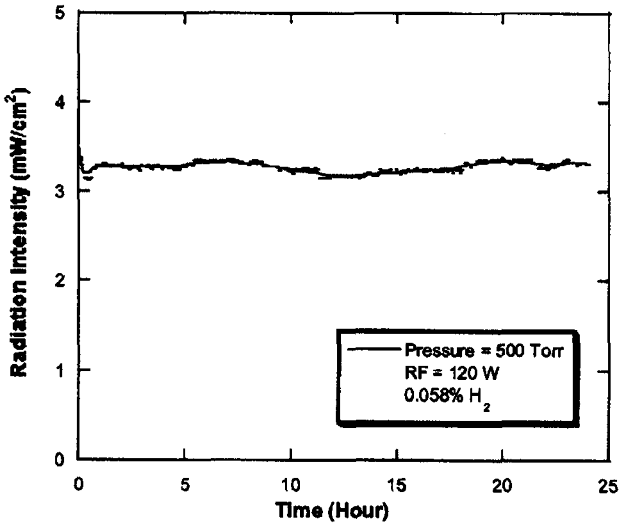

FIG. 6. Radiation intensity vs operating time: $P = 500$ Torr; rf = 120 W; 0.058% H_2.

with a small admixture of hydrogen, an intense and nearly monochromatic source at the Lyman-α line was built with FWHM less than 0.03 nm. The emission spectrum, optical power, efficiency, beam profile, and stability were investigated. High power emission up to 3.2 W at 121.6 nm was achieved. This study demonstrated that it is possible to achieve high power, spectrally narrow and stable 121.6 nm sources from a compact lamp for advanced lithography and other applications.

ACKNOWLEDGMENTS

This work was supported by the U.S. Defense Advanced Research Projects Agency (DARPA) under Contract No. DAAD 19-99-1-0277 and administered by Army Research Office. The author thanks Professor K. Becker and Dr. Akhmerov for helpful discussions.

[1] M. Rothschild *et al.*, J. Vac. Sci. Technol. B **17**, 3262 (1999).
[2] W. R. Ott, K. Behringer, and G. Gieres, Appl. Opt. **14**, 2121 (1975).
[3] A. Hollander and M. R. Wertheimer, J. Vac. Sci. Technol. A **12**, 879 (1994).
[4] A. C. Fozza, A. Kruse, A. Hollander, A. Ricard, and M. R. Wertheimer, J. Vac. Sci. Technol. A **16**, 72 (1998).
[5] P. Kurunczi, H. Shah, and K. Becker, J. Phys. B **32**, L651 (1999).
[6] M. Spaan, A. Goehlich, V. Schulz-von der Gathen, and H. F. Doele, Appl. Opt. **33**, 3865 (1994).
[7] M. Laroussi, Proceedings of the IEEE International Conference on Plasma Science, Monterey, CA, 1999, p. 203.
[8] B. Eliasson and U. Kogelschatz, IEEE Trans. Plasma Sci. **19**, 309 (1991).
[9] B. Gellert and U. Kogelschatz, Appl. Phys. B: Photophys. Laser Chem. **52**, 14 (1991).
[10] O. Motret, J. M. Pouvesle, and J. Stevefelt, J. Chem. Phys. **83**, 1095 (1985).
[11] J. Wieser, M. Salvermoser, L. H. Shaw, A. Ulrich, D. E. Murnick, and H. Dahi, J. Phys. B **31**, 4589 (1998).
[12] *Techniques and Applications of Plasma Chemistry*, edited by J. R. Hollahan and A. T. Bell (Wiley, New York, 1974).
[13] E. M. Gullikson, R. Korde, L. R. Canfield, and R. E. Vest, J. Electron Spectrosc. Relat. Phenom. **80**, 313 (1996).

High power 121.6 nm radiation source

Jianxun Yan and Mool C. Gupta[a]
Applied Research Center, College of Engineering and Technology, Old Dominion University, Newport News, Virginia 23606

(Received 8 July 2003; accepted 29 September 2003; published 9 December 2003)

A high power 121.6 nm radiation source based on dielectric barrier discharge (DBD) has been developed. Lamp parameters such as gas pressure, discharge tube diameter, electrode area and gap were optimized to maximize the 121.6 nm radiation power. Higher rf power was coupled to discharge by applying a flexible rf network, which matched the impedance between the source and discharge. The discharge was optimized by simulation using XOOPIC software to model the lamp. The simulation results were in agreement with our experimental measurements. The stable, high power (8 W) radiation source was achieved and it could be used as a reliable source for lithography and other applications. © *2003 American Vacuum Society.* [DOI: 10.1116/1.1627801]

I. INTRODUCTION

Photolithography using VUV light source of wavelength 121.6 nm has been evaluated to be a promising candidate for extending optical lithography beyond 157 nm.[1] In previous articles,[2,3] we have reported a vacuum ultraviolet (VUV) light source based on a high-pressure cylindrical dielectric barrier discharge (DBD), which was capable of producing intense and spectrally clean hydrogen Lyman-α line at 121.6 nm. The lamp generated Lyman-α line radiation via resonant energy transfer from neon excimer molecules to molecular hydrogen, which leads to dissociation and excitation. The output spectrum in the VUV region showed the strong Lyman-α line at 121.6 nm with linewidth less than 0.03 nm. Strong and stable radiation power was obtained, which had total power of 3.2 W in the 4π solid angle. This source was used for metrology and initial lithography experiments and some initial results were obtained. However, due to transmission and reflection losses of optical elements, this source still needs to be further improved to achieve high power radiation for practical exposure intensity level.

The lamp parameters such as discharge pressure, tube diameter, electrode area and gap have been optimized for maximum radiation power. In order to reduce the rf reflected power and efficiently couple rf power in discharge, a rf network was designed. By measuring rf power, voltage and current, the resistance and reactance of discharge were calculated. Water-cooling was used to minimize the electrode heating for enhanced discharge performance. The discharge was optimized by simulation using XOOPIC software to model plasma as discrete macroparticles interacting with EM field.

II. EXPERIMENTAL AND SIMULATION

The experimental system consisted of discharge chamber, measurement system, rf power source, and vacuum pumping system. The schematic setup and details were described in Ref. 2. Figure 1 shows a photograph of discharge chamber, which is connected to a monochromator and VUV radiation detector chamber. The discharge chamber was carefully designed for easy operation and measurement. A water-cooled copper ring clamp around a quartz tube was used as an anode electrode. The distance between the anode and cathode could be easily adjusted. For increased efficiency, the impedance of the discharge and that of the rf generator need to be matched. For this purpose, the rf cable from matching network was directly connected to the anode and a rf wattmeter (Model 43 from BIRD Electronic Corp.) was used to measure rf input power. An ac current probe (Mode P6021 from Tektronix Inc.) was looped around the cable to measure the discharge current.

XOOPIC is an object-oriented two-dimensional relativistic electromagnetic particle-in-cell code developed at the University of California at Berkeley.[4] The XOOPIC code can handle electrostatic and electromagnetic simulations and relativistic and nonrelativistic particles. It has been used to simulate a wide range of challenging problems, including plasma,[5] ion implantation, high-power microwave devices, and particle accelerators.[6] The XOOPIC code has implemented Cartesian and cylindrical geometries. Our discharge structure has cylindrical ($r-z$) geometry as shown in Fig. 2. The simulation geometry is a 2D cylindrical region with radium of 8 mm and length of tube as 45 mm. The anode and cath-

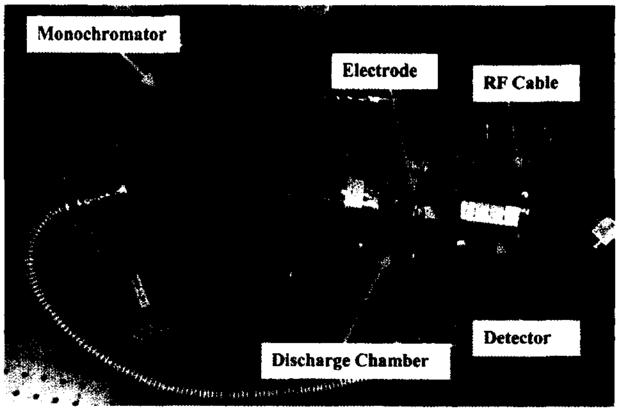

FIG. 1. Experimental setup.

---

[a] Electronic mail: mgupta@odu.edu

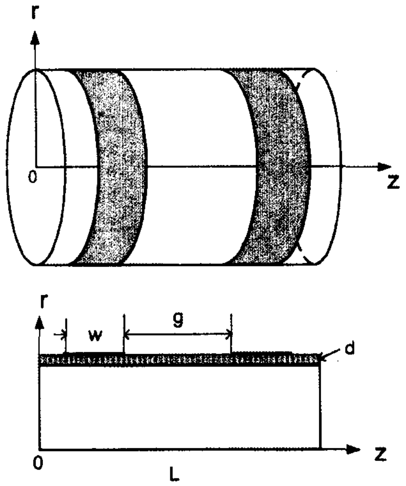

FIG. 2. 2D cylindrical geometry and simulation model parameters.

ode were located outside the dielectric tube, and each one had a width (*w*) of 10 mm. The distance between two electrodes called *g* is 15 mm. The thickness of the tube wall (*d*) is 1 mm. The boundary is closed with dielectric material.

III. RESULTS AND DISCUSSION

Emission spectra were measured at high pressure (100 Torr to atmosphere pressure) with a neon gas containing 0.06% hydrogen. The radiation intensity at 121.6 nm varied as a function of gas mixture pressure with a fixed input rf power of 200 W (Fig. 3). A maximum intensity was obtained at 180 Torr. At low pressure the intensity at 121.6 nm radiation was lower due to the high breakdown fields and insufficient neon excimer generation. In the high pressure region the intensity decreased with pressure. This was due to atomic hydrogen recombination into H_2. The recombination was more predominant at higher H_2 density, which resulted in a faster decrease of the Lyman-α radiation. Two plasma generation tubes of sizes, 15 mm o.d.×13 mm i.d. and 8 mm o.d.×6 mm i.d. were used. The radiation intensity from larger tube was about 10% higher than the smaller, because of more discharge volume. The thickness of tube was a factor that affected the discharge breakdown and radiation intensity. We used 1 mm thick tube because we could get higher ionization, resulting in higher intensity of VUV radiation than when a thicker tube was used. The radiation intensity at different electrode gap was also measured. From the experiment the optimum electrode gap was from 10 to 25 mm at a gas pressure of 200 Torr. The important feature of this DBD was that the plasma parameters could be easily changed and thus optimized.[7] The mean electron energy was controlled by the pressure in the discharge, the electrode spacing and the properties of the dielectric barrier.

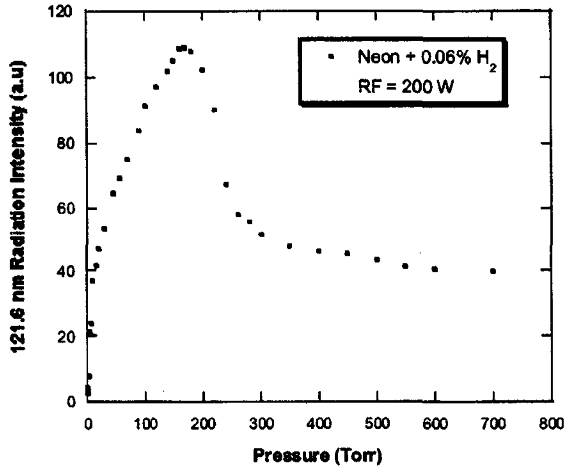

FIG. 3. 121.6 nm radiation intensity dependence on gas pressure.

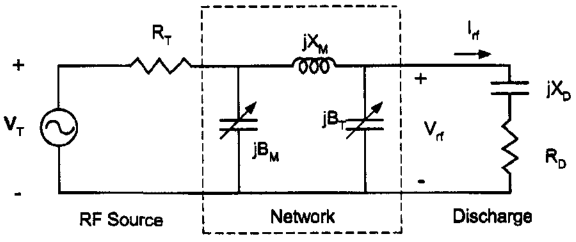

FIG. 4. Equivalent circuit for matching the rf power source to the discharge using a π-network.

If the discharge was driven directly by a rf power source, then generally power could not be transferred efficiently from the source to the discharge. A matching network can be placed between the source and load so that the supplied power from the source can be equal to the absorbed power by the discharge. Figure 4 shows that equivalent circuit for matching the rf power source to the discharge using a π-network. The power source was modeled by its Thevenin-equivalent circuit, consisting of a voltage source with complex amplitude $\tilde{V}_T$ in series with a source resistance R_T and discharge was modeled as a load having impedance $Z_D = R_D + jX_D$, where R_D is the discharge resistance and X_D is the discharge reactance, typically $X_D \gg R_D$. R_D and X_D are functions of the discharge-absorbed power P_{abs}, and are determined from

$$P_{\mathrm{abs}} = \tfrac{1}{2} I_1^2 R_D \tag{1}$$

and

$$X_D = -\frac{1}{\omega C_{ab}}, \tag{2}$$

where C_{ab} is the discharge capacitance, ω is the rf radian frequency, and I_1 is the current through the discharge. The network circuit consists of two variable capacitors and a fixed value inductive coil. By adjusting these two capacitors, the matched condition of maximum power transfer between the source and the load can be reached. The time-average power absorbed by the discharge can be expressed as

$$P_{\mathrm{abs}} = \frac{1}{\tau} \int_0^{\tau} V_{\mathrm{rf}}(t) I_{\mathrm{rf}}(t)\,dt = \frac{1}{2} I_1 V_{\mathrm{rf}} \sin \psi, \tag{3}$$

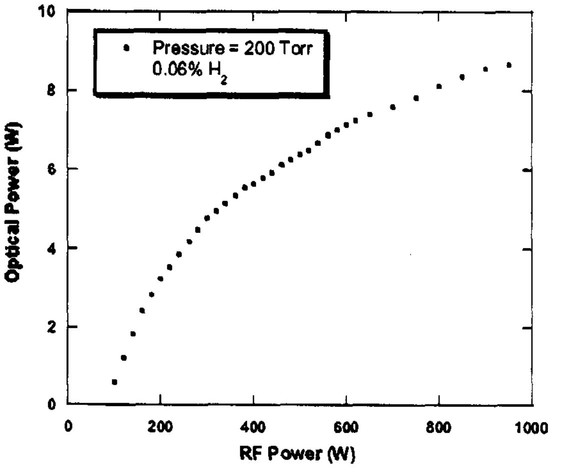

FIG. 5. Total optical power dependence on the input rf power at gas pressure of 200 Torr.

where $I_{rf}(t) = I_1 \cos \omega t$, $\psi = \tan^{-1}(R_D/X_D) \approx (R_D/X_D)$, $\tau = 2\pi/\omega$, and V_{rf} is the voltage across the discharge. Under matched conditions, the power supplied by the source, P_T, equals the power absorbed by the discharge,

$$P_{abs} = P_T. \tag{4}$$

The supplied power P_T was measured by the rf wattmeter, and the current I_{rf}, and voltage V_{rf} were measured with probes and displayed on an oscilloscope. From Eqs. (1), (2), and (3), we determined R_D, X_D, and C_{ab}. In our system, if rf input power is 100 W, we have current $I_1 = 0.6$ A, $V_{rf} = 1500$ V. Under the conditions of electrode area 2.5 cm^2 and electrode gap 15 mm, we have $R_D = 550$ ohm, $X_D = 2775$ ohm, and $C_{ab} = 4.2$ pF. The calculated values were in close agreement with the actual values used in the experiment.

The absolute Lyman-α radiation power was measured with a special silicon photodiode (IRD company, model SXUV-100). Figure 5 shows the total optical power variation with rf input power from 50 W to 900 W at conditions of 200 Torr gas pressure, 0.06% H_2 mixture, and a gas flow rate of 660 sccm. The total radiation power of 8 W at 800 W of rf input power was obtained. The previous results discussed in Ref. 2 had an optical power of 3.2 W at rf power of 200 W. With improved water-cooling and rf matching, we were able to inject higher rf power in the discharge to obtain higher optical intensity. The emission intensity at this power was 12.3 mW/cm^2 for a distance of 5 cm between the detector and the front edge of the source. The maximum electrical to optical conversion efficiency was 1.65% at gas pressure of 200 Torr. The VUV output increased with increasing input energy due to the corresponding increased in the electron density. But if the density gets too large, the VUV efficiency dropped due to quenching collisions of exited species with electrons.

Due to collisional momentum transfer between the oscillating electrons and the neutrals, some part of the power deposited in the bulk plasma caused heating.[8] Heat generated in high pressure nonequilibrium plasma wasted energy and often caused unfavorable temperature rise in the discharge fields. In DBD discharge, most of the input power was selectively transferred to the dielectric electrode. This was because microdischarges spread into a surface discharge on the dielectric wall, covering much larger area than the original filament diameter. In our system, the temperature could reach over 1000 °C. High temperature could significantly damage the copper electrode and the quartz tube, so the water-cooling system was necessary. Both electrodes were equipped with water-cooling circuits, and the temperature was controlled appropriately for better operating conditions.

The discharge was simulated using the XOOPIC code with a rf voltage, which had a frequency of 13.56 MHz. Typical results of simulation were the electric field, the electron and ion density-profiles. These values were taken at 10^{-6} s, which is approximately 13 times the rf period, and did not change significantly with time, so we considered approaching the steady state. Figure 6 shows the distribution of electron and ion in the $r-z$ cylindrical geometry. At the initial condition the electron and ion were distributed evenly over the whole volume with a density of 10^{15} cm^{-3}. Under the formation of the electric field, the electron moved to the center of the cylinder. At the steady state, the center of the tube had high electron density of 2×10^{17} cm^{-3}. The high-energy electron collided with the neutral gas and ionized the neon, thus more ions were formed and more Lyman-α radia-

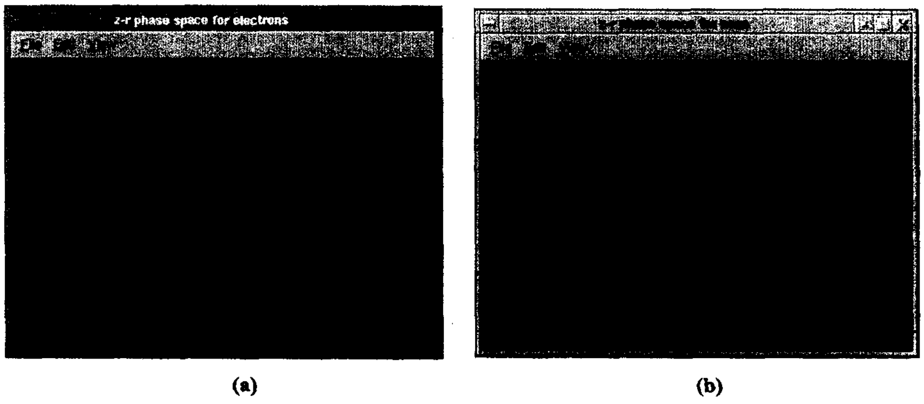

(a) (b)

FIG. 6. Radial and axial distribution for (a) electrons (b) neon ions.

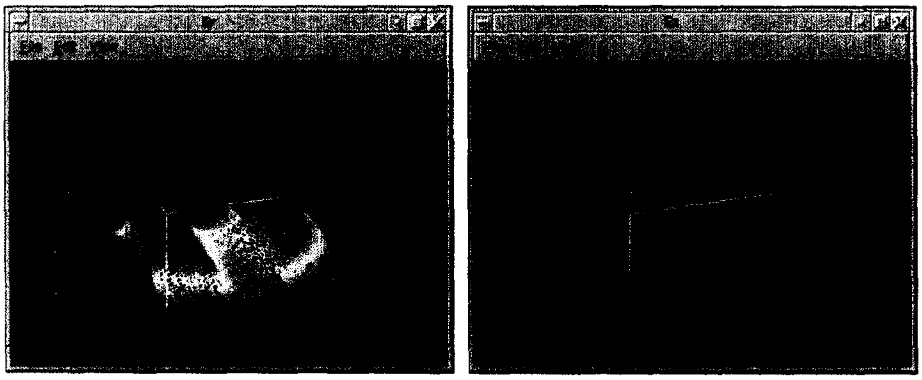

(a)

(b)

FIG. 7. Electric field along (a) radial direction; (b) axial direction.

tion emitted from the center of the tube. According to the simulation, the discharge filament was about 3 mm diam, which was consistent with our experimental results.[2] Figure 7 shows the variation of electric field along radial (r) and axial (z) directions. The E field at the electrode region was higher than the other region, and had peaks at the edge of the electrodes, which had an intensity of 6×10^5 V/m. The high E field at the electrode region pushed the electron and ion to the tube center. The average temperature of the electron was also obtained, which was 8 eV at the steady state. This energy was suitable for the excitation of a rare gas atom and the formation of the excimer. Simulation results allowed us to choose optimum discharge tube size, tube wall thickness, and electrode gap.

IV. CONCLUSIONS

The rf parameters, discharge tube diameter, thickness, electrode area and gap, gas pressure were optimized to maximize the radiation power at 121.6 nm wavelength. With the rf network and water-cooling circuit higher rf power was coupled in discharge, and a total radiation power of 8 W at 121.6 nm was achieved. By using XOOPIC software to model and simulate the lamp, the discharge parameters, electron and ion distribution, electric field, electron density and energy were obtained. From the results of measurement and initial experiment, the stable, high power (8 W) radiation source should be suitable for photolithography and other applications.

ACKNOWLEDGMENTS

This work was supported by the U.S. Defense Advanced Research Projects Agency (DARPA) under Contract No. DAAD 19-99-1-0277 and administered by the Army Research Office.

[1] V. Liberman, M. Rothschild, P. G. Murphy, and S. T. Palmacci, J. Vac. Sci. Technol. B **20**, 2567 (2002).

[2] J. Yan, A. El-Dakrouri, M. Laroussi, and Mool C. Gupta, J. Vac. Sci. Technol. B **20**, 2574 (2002).

[3] A. El-Dakrouri, J. Yan, M. C. Gupta, M. Laroussi, and Y. Badr, J. Phys. D **35**, L109 (2002).

[4] J. P. Verbonconeur, A. B. Langdon, and N. T. Gladd, Commun. Phys. (London) **87**, 199 (1995).

[5] C. H. Shon, J. K. Lee, H. J. Lee, Y. Yang, and T. H. Chung, IEEE Trans. Plasma Sci. **26**, 1635 (1998).

[6] D. Bruhwiler, J. Cary, J. Verboncoeur, P. Mardahl, and R. Giacone, Proceeding of EPAC 2000, Vienna, Austria, 2000, Vol. 877 (unpublished).

[7] B. Gellert and U. Kogelschatz, Appl. Phys. B: Photophys. Laser Chem. **52**, 14 (1991).

[8] T. Nozaki, Y. Miyazaki, Y. Unno, and K. Okzazki, J. Phys. D **34**, 3383 (2001).

Direct metal pattern writing by VUV photodissociation

Jianxun Yan and Mool C. Gupta[a)]
Applied Research Center, College of Engineering and Technology, Old Dominion University, Newport News, Virginia 23606

(Received 2 June 2004; accepted 9 August 2004; published 10 December 2004)

An efficient process for direct pattern writing of thin metallic films has been developed using a 121.6 nm vacuum ultraviolet source by photodissociation of metalorganic materials. The optical reflection, crystal structure, and surface morphology of photodissociated palladium thin films were studied using a spectrophotometer, x-ray diffraction, and scanning electron microscopy. A pattern of 5 μm palladium lines separated by 5 μm spaces was produced on glass substrate by contact printing lithography. © *2004 American Vacuum Society.* [DOI: 10.1116/1.1802871]

I. INTRODUCTION

In the past, metalorganic materials for growing thin films of metals, dielectrics, and semiconductors have generally been gases, as used in laser-induced chemical vapor deposition. Metalorganic gases, such as $Al_2(CH_3)_6$, $Ge(CH_3)_4$, and $Cr(CO)_6$, have been decomposed to metal films using lasers and vacuum ultraviolet (VUV).[1-5] Unfortunately, depositing metals from gaseous precursors requires a complex and expensive vacuum system. Recently, metal deposition by large-area VUV-induced decomposition of metalorganic compounds has been reported.[6-8] Metalorganic decomposition is a liquid-based method of depositing thin films, and does not require a vacuum. A metalorganic precursor, dissolved in appropriate solvent, is dispensed onto a substrate. After the solvent is evaporated, a VUV source is used to decompose the metalorganic film, converting the metalorganic precursors to their constituent metal elements. A variety of thin films (Au, Cu, Pd, etc.) have been deposited onto various substrates using different types of VUV radiation sources. The production of thin films by VUV-induced metalorganic decomposition offers several advantages over other methods of thin-film deposition. The process occurs at ambient temperature and pressure without gas transport, and therefore needs no complicated vacuum equipment. Precursor materials can also be synthesized to incorporate a wide variety of metals. Since the metal ion and the organic radicals in the metalorganic materials are held together by weak bonds, the compounds decompose at relatively low temperatures. As a result, temperature-sensitive materials can also be coated.

Large-area VUV sources with high photon fluxes provide a relatively low-cost method for industrial large-area processing. In this article, we have demonstrated that palladium, copper, and gold thin-film deposition can be achieved by decomposition from their corresponding organic compounds using a VUV source based on a dielectric barrier discharge (DBD).[9,10] The high-energy (10.2 eV) of Lyman-alpha photons is sufficient to break the bond between the metal ion and the organic radical in most metalorganic materials. Very uniform thin films of palladium and direct pattern writing have been achieved in our experiment. Palladium thin films may act as catalysts for subsequent electroless metal deposition. This method can be used for deposition and patterning of various types of metallic, semiconducting, and nonconducting films for various applications.

II. EXPERIMENTAL PROCEDURE

Palladium acetate [$Pd(OCOCH_3)_2$; (Pdac)], obtained from Alfa Aesar, was dissolved in chloroform solution. Thin films of Pdac of 100– ~ 1000 nm thickness were prepared by spin-coating on glass, quartz, and silicon substrates. The resulting Pdac thin films were then directly irradiated by the high-intensity Lyman-α line (121.6 nm) from a cylindrical DBD-based VUV lamp source[9,10] operating in an Ne and H_2 mixture at various pressures between 1 and 500 Torr. Figure 1 shows the experimental setup. The glass substrate and discharge tube were in the same chamber, allowing the film to be directly exposed to the Lyman-α radiation with power density of 10 mW/cm^2. A photon detector and an He-Ne laser of wavelength 632.8 nm were used to measure the film's transmission. The progress of palladium film deposition could be determined by measuring the change in transmission at different pressures and exposure times. The Pdac film thickness was measured using a Tencor Alpha step 200 profilometer. The thickness of palladium film after decomposition was measured with atomic force microscopy (Digital Instruments Dimension 3100). The transmission and reflection of palladium film were measured from UV to near infrared (NIR) using a Perkin-Elmer Lambda 9 spectrophotometer.

III. RESULTS AND DISCUSSION

A. Palladium thin film

The absorption of photons ($h\nu > 3.0$ eV) in Pdac initiates its decomposition into palladium and volatile organic species as

$$Pd(OCOCH_3)_2 \rightarrow Pd + COCH_3^+ + CCH_3^+ + CH_3^+ + CO_2 + H_2O.$$

The decomposition mechanism of Pdac with VUV radiation has been discussed in literature.[11] The formation of Pd over time was determined by measuring the sample's transmission

---

[a)]Electronic mail: mgupta@odu.edu

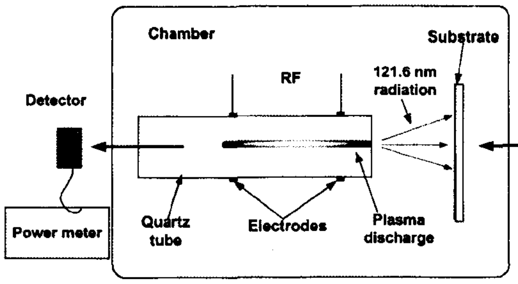

FIG. 1. Experimental setup for photodissociation studies.

for laser light at a wavelength of 632.8 nm. The transmission of the films decreased rapidly during the first 60 s, a flat transmission curve was then observed (Fig. 2). The flat curve indicated that the palladium film had completely decomposed and pure Pd film had formed. Compared with other VUV sources, our 121.6 nm radiation lamp achieved palladium film in the least time.

The decomposition rate of Pdac also depended on the pressure in the chamber. Figure 3 showed the time to obtain 95% metal palladium in films under different pressures. At a pressure of 3 Torr, the Pdac decomposed completely within 1 min. At high pressures, it took much longer time to decomposed the palladium acetate. This result was similar to that of other experiments mentioned in,[12] which also provided an explanation. In our system, the discharge gas was ventilated, removing volatile decomposition products that would attenuate the Lyman-α radiation.

With continued illumination at the Lyman-α line, the palladium crystallite appeared and started to grow until it formed a homogeneous palladium film on the glass substrate. The film was examined by optical microscopy and scanning electron microscopy (SEM). The crystal structure of palladium film was studied by x-ray diffraction (XRD). Figure 4 shows the XRD spectrum taken by a Rigaku x-ray diffractometer ($\lambda=0.1538$ nm). An intense diffraction peak occurs at 40.1°, which is the same diffraction angle (2θ) as for the characteristic Pd [111] crystal. The initial thickness of Pdac film was 300 nm; after irradiation with Lyman-α, it reduced to 50 nm. The thickness change is due to the loss of volatile products and organic species during decomposition. Another reason for the lower final thickness is that palladium is much denser than Pdac. With the spectrophotometer, we measured the optical transmission and reflection of 100-nm-thick films of Pdac and metal palladium from wavelengths 200 to 1000 nm. The transmission of the Pdac film was about 80% at wavelengths from 600 to 1000 nm, while the transmission of the metal palladium film was less than 5% [Fig. 5(a)]. The reflectivity of Pdac was 17% from

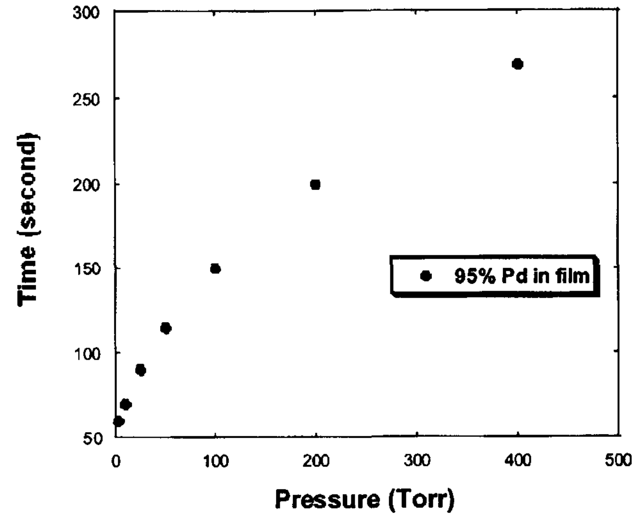

FIG. 3. Time to achieve 95% palladium metal content in films under different pressures.

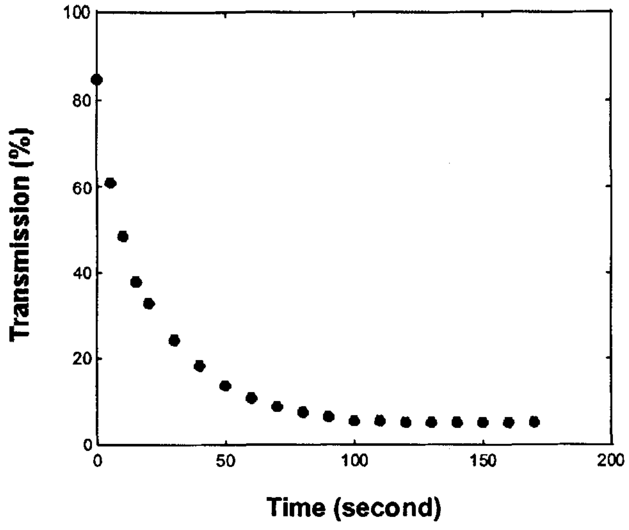

FIG. 2. Evolution of light transmission through palladium and Pdac film as a function of exposure time at pressure of 3 Torr.

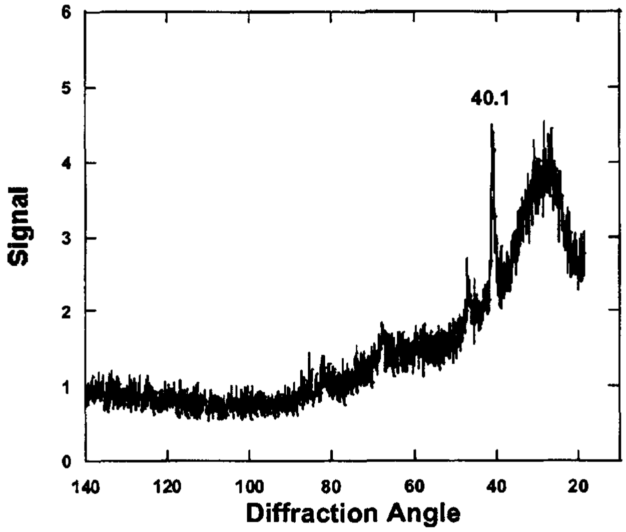

FIG. 4. XRD spectrum of palladium film after photodissociation.

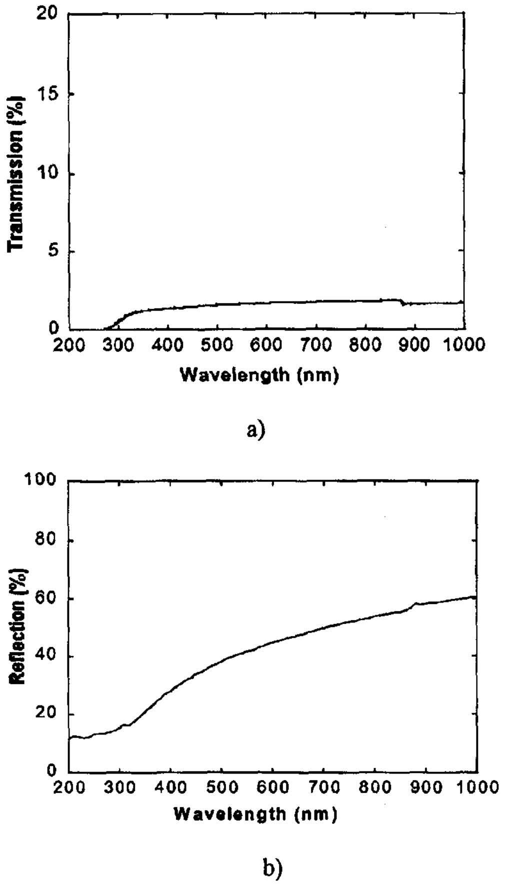

FIG. 5. Optical spectral measurement for palladium film: (a) transmission and (b) reflection.

200 to 1000 nm. The reflectivity for metal palladium increased with wavelength, with 60% at 1000 nm [Fig. 5(b)]. From literature, the reflectivity of pure bulk palladium is 72% at 1000 nm. The four-point probe technique was used to measure the electrical resistivity of the palladium film, giving a resistivity of about 200 $\mu\Omega$ cm for a 50-nm-thick film.

B. Direct pattern writing

Contact printing photolithography was used to direct-write palladium patterns with a MgF_2 mask. The optical materials that transmit 121.6 nm wavelength are MgF_2 and LiF. However, LiF is hygroscopic and mechanically soft,[13] so that in our experiment MgF_2 with 1 in. diameter and 1 mm thickness was used for mask fabrication. The MgF_2 mask was fabricated by patterning grating lines in photoresist using i-line contact lithography. First, a master mask with 5-μm lines and 5-μm spaces was contacted to the MgF_2 substrate, which had been precoated with i-line resist. The resist on the MgF_2 substrate was then exposed and developed. The resist lines on the MgF_2 substrate are opaque to 121.6 nm light, while the spaces with no resist are transparent. The transmission of the resist and substrate was measured directly with our DBD lamp and the photomultiplier tube coupled to the monochromator at 121.6 nm wavelength. The transmission of the 300 nm resist was less than 1%, while the transmission of the pure MgF_2 substrate was 67%. An MgF_2 substrate patterned with photoresist was used as a mask for 121.6 nm lithography.

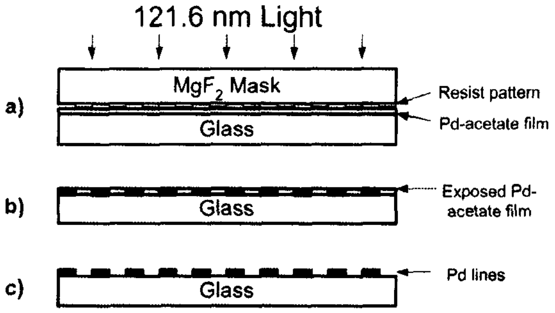

FIG. 6. The palladium pattern writing process: (a) contact printing, (b) after exposure, and (c) after Pdac removal.

A C-mount held the MgF_2 mask in contact with a Pdac-coated glass wafer of 1 in. diameter and 1 mm thickness. After exposed to 121.6 nm light, metal palladium lines were formed, while Pdac in the opaque area remained unchanged.

Chloroform was used to wash out the residual Pdac, leaving pure palladium lines on the glass substrate. Figure 6 illustrates how palladium patterns are made by contact printing. Figure 7 is an optical microscope photograph of the palladium pattern, which was obtained with Lyman-α radiation exposure for 2 min under low-pressure discharge conditions. Figure 8 displays a SEM micrograph of the pattern on the glass substrate indicating a line width of 5 μm.

IV. CONCLUSIONS

Palladium films have been formed on a glass substrate using a 121.6 nm radiation source. The growth rate of palladium is affected by radiation density and discharge pressure. High-energy photons, strong radiation flux, and low operation pressures enhanced the photodecomposition of palladium acetate. The results obtained with the spectrophotometer, XRD, and SEM show that the palladium films obtained were of good quality. Direct patterning of palladium films

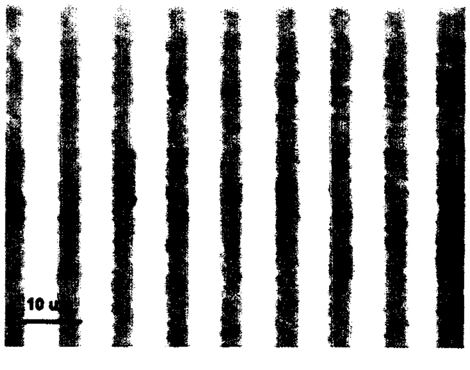

FIG. 7. Optical micrograph of palladium pattern (5 μm lines separated by 5 μm spaces).

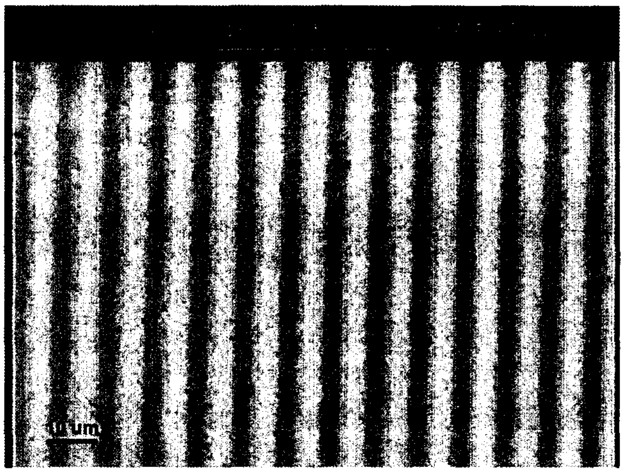

FIG. 8. SEM micrograph of palladium pattern.

was demonstrated using standard lithography process, yielding lines of 5 μm width. Lines of width less than 1 μm should be possible. The direct writing method offers attractive applications in microcircuits, multichip interconnects, direct lithography, and prototype fabrication.

ACKNOWLEDGMENTS

The authors thank Dr. Jousef Mohajer for his help in the determination of chemical compounds. This work was supported by the U.S. Defense Advanced Research Projects Agency (DARPA) under Contract No. DAAD 19-99-1-0277 and administered by the Army Research Office. Thanks to Cornell University National Nanofabrication Facility for fabrication of the MgF_2 masks.

[1] A.R. Calloway, T.A. Galantowicz, and W.R. Fenner, J. Vac. Sci. Technol. A **1**, 534 (1983).

[2] M. Hanabusa, A. Oikawa, and P.Y. Cai, J. Appl. Phys. **66**, 3268 (1989).

[3] C. Lavoie, M. Meunier, R. Izquierdo, S. Boivin, and P. Desjardins, Appl. Phys. A: Mater. Sci. Process. **53**, 339 (1991).

[4] D. K. Flynn, J. I. Steinfeld, and D. S. Sethi, J. Appl. Phys. **59**, 3914 (1986).

[5] R. Haight, P. Longo, and A. Wagner, J. Vac. Sci. Technol. A **21**, 649 (2003).

[6] J. Y. Zhang, I. W. Boyd, and S. Draper, Surf. Coat. Technol. **100–101**, 469 (1998).

[7] Y. Zhang and M. Stuke, Appl. Surf. Sci. **46**, 153 (1990).

[8] H. Esrom and U. Kogelschatz, Appl. Surf. Sci. **54**, 440 (1992).

[9] J. Yan, A. El-Dakrouri, M. Laroussi, and M. C. Gupta, J. Vac. Sci. Technol. B **20**, 2574 (2002).

[10] J. Yan and M. C. Gupta, J. Vac. Sci. Technol. B **21**, 2839 (2003).

[11] J. Y. Zhang, H. Esron, and I. W. Boyd, Appl. Surf. Sci. **96–98**, 399 (1996).

[12] J. Y. Zhang and I. W. Boyd, Appl. Phys. A: Mater. Sci. Process. **65**, 379 (1997).

[13] V. Liberman, M. Rothschild, P. G. Murphy, and S. T. Palmacci, J. Vac. Sci. Technol. B **20**, 2567 (2002).